

Molecular Studies of Confined Liquids and Nanofluids for Passive Thermal Management

Michael Frank

Submitted for the Degree of Ph.D.



Institute of Aerospace Science
Cranfield University
Cranfield, UK

2015

Cranfield University

School of Aerospace, Transport and Manufacturing (SATM)

PhD

Michael Frank

Molecular Studies of Confined Liquids and
Nanofluids for Passive Thermal Management

Supervisors

1st: Prof. Dimitris Drikakis, 2nd: Dr. Nikolaos Asproulis, 3rd: Mr. Angus
Murray

March, 2015

Abstract

The constant technological advances in integrated circuits and electronic systems experienced over the last few years have resulted in large temperature gradients. These can damage electronic devices. Current cooling methods are unable to cope with highly demanding applications such as military systems. Furthermore, for applications in which failure is not an option, a lack of sufficient thermal management can be a limiting factor in the design and addition of functionality.

The aim of this research project is to provide possible solutions to the overheating of electronics. Following an in depth review of the state-of-the-art in cooling technologies, we have identified nanofluidics and nanofluids as promising candidates for thermal management. However, systems characterised by such small dimensions are governed by surface phenomena. Sometimes, continuum computational methods such as Computational Fluid Dynamics (CFD) are inadequate in providing a detailed description of such effects. Instead, molecular methods, such as Molecular Dynamics (MD), study systems at a higher resolution and can potentially provide a more accurate understanding of such systems.

This thesis uses MD to understand how the thermodynamic properties of liquids and nanofluids are modified by spatial restrictions. An important finding is that heat is transferred differently in confined and unconfined liquids. Following this realisation, an analysis of the system parameters is carried out to understand how to optimise the heat conductance of such systems. We also consider confined nanofluids. Different materials are modelled and compared with respect to their possible practical use as thermal management agents.

The thermodynamic behaviour discovered has not been described elsewhere and has potentially high practical importance. Although in its infancy, we believe that it can eventually provide a framework for the design of efficient cooling devices.

Acknowledgements

During the period of this PhD, a number of people have played an important role in the completion of this project.

First of all, I would like to thank BAE systems for all their support. Particularly I would like to thank Mr. Angus Murray for his excellent job in coordinating this project. Through reviews held every three months during this PhD, he has managed to create an interdisciplinary network of academic and industrial professionals making the entire experience much more rewarding.

I would also like to express my sincere gratitude to my supervisors Professor Dimitris Drikakis and Dr. Nikolaos Asproulis. In addition to giving me the opportunity to do this research degree, their expertise and intellect have provided inspiration throughout this project. Their support was always in the form of friendly advice, which has made this period particularly enjoyable. I genuinely feel very lucky to have had the chance to work with them.

I am very grateful to my house-mates Tassos Mesogitis, Dinos Tzanidakis and Manolis Daxtilelis for making my stay here at Cranfield particularly pleasant. I also want to thank Michalis Papanikolaou, with whom I have been sharing an office for the last few years. Apart from being a pleasant individual and a good friend, our everyday technical discussions have become an important part of my thinking process and in the analysis of my results.

I would also like to thank my older brother Kyriacos Frank who is still looking after me, even as I am reaching the age of 28. Telephone conversations with him and his wife (and my friend) Christina Mitidou have frequently cheered me up at times where much needed. This section would be incomplete without acknowledging the help of our newest member, Miss Mara Frank (9 days old as of today). Her arrival in this world has provided the strength required during the last two weeks while editing this thesis.

I would also like to attribute special thanks to my parents Photini and Gordon Frank. Their never-ending support (in any conceivable form) has been the driving force behind every step of my life, including this PhD. The optimistic personality I have inherited from them has made the difference between three exhausting years and an enjoyable research experience. My gratitude towards them cannot possibly be expressed in writing (especially in a single paragraph) or otherwise.

Last but not least, I would like to thank my grandmother the late Loukia Photiou; an impressive and hard-working personality. Our stimulating discussions through my entire life have made me eager to constantly improve, gain new experiences, meet new people, and always aim high.

Contents

1	Introduction	1
1.1	Passive Thermal Management	1
1.2	Micro and Nano Flows	2
1.3	Nanofluids	2
1.4	Modelling fluids and nanofluids	2
1.5	Aims and Objectives	4
1.6	Publications	5
1.7	Thesis Overview	6
2	Thermal Management	8
2.1	Heat Transfer	8
2.1.1	Heat Conduction	8
2.1.2	Convection	9
2.1.3	Radiation	10
2.2	Conventional Heat Exchangers	10
2.2.1	Heat Sinks	10
2.2.2	Heat Pipes	13
2.3	Carbon allotropes	17
2.3.1	Introduction	17
2.3.2	Overview of common carbon allotropes	17
2.3.3	Theoretical overview of heat transfer in carbon allotropes	19
2.4	Nanofluids	24
2.4.1	Mechanisms for Enhancement of Thermal Conductivity	25
2.4.2	Nanofluids for Thermal Management	29
2.5	Conclusions	30
3	Molecular Modelling	31
3.1	Geometrical Structure	32
3.1.1	Crystallography	32
3.1.2	Boundary Conditions	37
3.2	Dynamics	39
3.2.1	Intramolecular Forces	39
3.2.2	Intermolecular/interatomic Forces	43
3.2.3	Interatomic Potentials	45
3.3	Statistical Mechanics	52
3.3.1	General Overview	52
3.3.2	Monte Carlo	61

3.3.3	Molecular Dynamics	65
3.4	Conclusions	69
4	Thermal Behaviour of Confined Liquids	71
4.1	Introduction	71
4.2	Computational Model	72
4.3	Validation and Uncertainty	73
4.4	Crystal-like heat transfer of liquids in nanochannels	75
4.5	Parametric analysis	81
4.5.1	Solid-Liquid Interactions	82
4.5.2	Density	84
4.5.3	Temperature	90
4.6	Conclusions	93
5	Thermal Behaviour of Confined Nanofluids	95
5.1	Thermal Conductivity of copper-argon Nanofluids in Nano-channels . . .	96
5.1.1	Computational Model	96
5.1.2	Results and Discussion	97
5.1.3	Summary	104
5.2	Water-Copper	104
5.2.1	Computational Model	104
5.2.2	Results and Discussion	106
5.2.3	Summary	109
5.3	Conclusions	110
6	Conclusions and Future Work	111
	Appendices	114
A	Reduced Units	115

List of Figures

1.1	Representation of various computational methods for modelling fluids based on the length and timescales of the system	4
2.1	Thermal conductivity of heat sink materials. Reproduced from [1]	11
2.2	Cross-section of some heat sink designs. The micro-channel heat sink (2.2a) has continuum grooves through which the liquid can flow. Instead, micro-pin fin heat sinks can have discrete protuberances exposing a greater surface area to the fluid. These can be either aligned (2.2b) or staggered (2.2c)	12
2.3	A simple heat pipe	13
2.4	A loop heat pipe	15
2.5	The temperature of the LHP evaporator as a function of the heat load. Reproduced from [2, 3]	16
2.6	Derivation of graphene and CNTs from graphite. Graphene is a single atomic layer extracted from graphite and a single CNT is a rolled up graphene sheet	18
2.7	Thermal conductivity of aligned and Unaligned SWNTs as a function of the temperature. Reproduced from [4]	20
2.8	Thermal conductance and thermal conductivity (inset) of a single MWNT as a function of the temperature. The image at the top left is the structure used for the calculation of the thermal conductivity. Reproduced from [5]	21
2.9	MD calculations of the thermal conductivity of a (10,10) SWNT. Reproduced from [6]	22
2.10	Comparison between the thermal conductivities of 3D graphite (the lower, dotted line), 2D graphene (the top, dash-dot line), and 1D SWNTs (the middle, solid line). The inset compares experimental measurements [7–9] for graphite with the results of the simulations	23
2.11	Periodic nature of the thermal conductance of a sheet of graphene. It is shown that as the angle of the heat flux on the plane changes, the conductance is oscillatory with a period of $\frac{\pi}{3}$. Reproduced from [10]	23
2.12	Thermal conductivity enhancement as a function of the temperature. The model based on the Brownian motion of the nanoparticles (straight lines) is compared with experimental data. Reproduced from [11]	26
2.13	SEM picture of Ludox (silica) nanofluid, indicating clustering of nanoparticles. Reproduced from [12]	28
2.14	Serial and parallel modes of conduction. The former represents the absolute lowest thermal conductivity limit while the latter represents the absolute highest possibility. Reproduced from [12]	28

3.1	The atomic structure of a crystal solid (3.1a) with the atoms arranged hexagonally and a corresponding lattice (3.1b). The lattice is obtained by collecting all the points from the crystal structure which are identical to O in terms of the relative positions of their neighbours	33
3.2	Two lattice planes (shaded) within a unit cell of a cubic lattice	36
3.3	Conventional and primitive cell of fcc lattice. Reproduced from [13] . . .	36
3.4	A close-packing of spheres arranged in an fcc structure	37
3.5	An illustration of periodic boundary conditions in two dimensions. The simulation cell is infinitely stacked in the two dimensions such that all atoms interact in a similar manner	38
3.6	Periodic table depicting all the known elements found in nature. Reproduced from Wikipedia under "Periodic Table" thread)	40
3.7	A schematic representation of a covalent bond within a water molecule between an oxygen (light green) and two hydrogen atoms (light blue). The smaller circles represent electrons with the dark blue electrons being the ones initially possessed by the hydrogen atoms and the dark green electrons being the ones initially possessed by the oxygen atom	42
3.8	A schematic representation of a metallic bond between iron atoms (FE). The negatively charged electrons (yellow with minus sign) move freely across the lattice. The positively charged iron atoms are attracted to this electron fluid through electrostatic forces	43
3.9	Schematic representation of the polarity of water molecules (3.9a) and the dipole-dipole interactions between them (3.9b)	44
3.10	Lennard-Jones potential as a function of the interatomic distance. The function crosses the axis at a distance σ and reaches a minimum at $-\epsilon$. At short distances (shaded as red) the interatomic forces are repulsive due to the Pauli exclusion principle while at larger distances (shaded in blue), van der Waals forces are attracting the atoms	47
3.11	Illustration of 3-site model 3.11a and 4-site model 3.11b site models for water. The dark blue circles indicate positive charges, the red circle indicates the negative charge and the yellow circle is where the LJ potential is acting. The 3-site model has its charges on the same positions as the atoms. The 4-site model shifts the negative charge toward the hydrogens along the bisector of the angle	51
3.12	Schematic representation of the NEMD method for calculating the thermal conductivity. First a temperature difference is introduced between two regions. Once the system has reached steady state, the heat transferred from the hot to the cold region is measured. The heat and the temperature gradient extracted from the linear temperature profile are then used in Fourier's law of conduction to realise the thermal conductivity	59
4.1	MD model of liquid argon confined in a nanochannel, visualized using VMD	72
4.2	Convergence of the thermal conductivity for the various channel widths .	74
4.3	Convergence of the thermal conductivity for the various channel widths .	75

4.4	HFACF in the x-direction for unrestricted liquid argon (blue) and for liquid argon in a nanochannel (red)	76
4.5	Density contours in the xy plane averaged over time	77
4.6	HFACF of a liquid in a 6.58σ channel and the sum of two exponential functions fitted onto it	78
4.7	The thermal conductivity of the system as a function of the wall separation. The four curves represent the property as obtained by a direct integral of the HFACF(green), by using Eq. 4.4.2 (red), and the individual short (black) and long (blue) range effects	79
4.8	Density profiles in the direction of confinement for 3 different wall separations	81
4.9	The thermal conductivity as a function of the interaction strength between the solid walls and the liquid, ϵ_{wl}	83
4.10	Decomposition of the thermal conductivity of a liquid in a channel of 8.3σ as a function of the liquid density.	84
4.11	Thermal conductivities against the density of the liquid (4.11a) and the wall separation of the channel (4.11b).	86
4.12	HFACF of liquid in a 6.58σ -width channel in the y direction for various densities.	87
4.13	The HFACF in the y direction for various wall separations for $\rho = 0.75\rho^*$ (4.13a) and $\rho = 0.84\rho^*$ (4.13b)	89
4.14	Thermal conductivity against the system temperature for 4 different wall separations	91
4.15	Density profiles in the direction of confinement for 2 different system temperatures	92
5.1	Schematic representation of the MD model of a copper-argon nanofluid confined within two idealized walls. On the right hand image the argon particles are made transparent	96
5.2	Thermal conductivity of the nanofluid (blue) and pure argon (red) as a function of the channel width. The black line is obtained through regression of all but the first point of the thermal conductivity of the nanofluid	98
5.3	Thermal conductivity of the nanofluid as a function of the volume fraction	99
5.4	Radial distribution function of the liquid around the nanoparticle	100
5.5	Density profiles of the liquid close to the channel wall	101
5.6	Thermal conductivity of nanofluid in the y direction as a function of the channel width	102
5.7	Total MSD (5.7a) and its component in the normal direction (5.7b directions)	103
5.8	Schematic representation of atomistic model. The oxygen (light blue) and hydrogen (light pink) make up the water molecule. The copper nanoparticle (green) can be seen slightly protruding in the centre	105
5.9	Thermal conductivity of the nanofluid as a function of the volume fraction for 3 different wall separations.	106
5.10	Thermal conductivity of nanofluid as a function of the wall separation for 4 different volume fractions.	107

5.11 Normalized thermal conductivity of the nanofluid as a function of the volume fraction for 3 different wall separations. 108

5.12 Density profiles for pure water ($\phi = 0\%$) and a nanofluid with particle loading $\phi = 2.75\%$ for two different wall separation distances 108

List of Tables

3.1	The 14 Bravais lattices divided into 7 lattice systems. Reproduced from the thread “Bravais Lattice” from Wikipedia	34
3.2	Table with LJ parameters for pairwise interactions between atoms of the same element. These values are merely empirical and might vary significantly depending on the type of bonding between them	48
3.3	Parameters of some 3-site models [14]	52
5.1	Lennard Jones parameters between atoms of the system. C represent the carbon atoms of the graphene walls, H and O represent the hydrogen and oxygen atoms of the water molecules and Cu refers to the copper atoms that constitute the nanoparticle	106
A.1	Reduced units	115

Abbreviations

- CNT** Carbon Nanotube. 18
- DOF** Density of States. 19
- EAM** Embedded Atom Method. 49
- EMD** Equilibrium Molecular Dynamics. 58
- FEM** Finite Element Method. 24
- FLG** Few-Layer Graphene. 22
- HFACF** Heat Flux Autocorrelation Function. 60
- HMCM** Hybrid Molecular/Continuum Methods. 3
- HOPG** Highly-Oriented Pyrolytic Graphite. 17
- LAMMPS** Large Scale Atomic/Molecular Massively Parallel Simulator. 70
- LHP** Loop Heat Pipe. 14
- LJ** Lennard-Jones. 46
- MC** Monte Carlo. 3
- MD** Molecular Dynamics. 3
- MFP** Mean Free Path. 9
- MSD** Mean Square Displacement. 57
- MWNT** Multi-walled Carbon Nanotube. 18
- NEMD** Non-Equilibrium Molecular Dynamics. 58
- RDF** Radial Distribution Function. 56
- SPC** Single Point Charge. 51
- SWNT** Single-Walled Carbon Nanotube. 18
- TIP3P** Transferable Intermolecular Potential 3 Point. 51
- TIPS** Transferable Intermolecular Potential Functions. 51

Nomenclature

- $A(x \rightarrow x')$ Acceptance operator. 64
- C_v Specific heat capacity at constant volume. 9
- D Diffusion coefficient. 57
- E Energy. 53
- K Characteristic stiffness of a spring. 49
- MSD(t)** Mean square displacement. 57
- N Number of atoms. 53
- NPT Isothermal-Isobaric Ensemble. 53, 61
- NVE Microcanonical ensemble. 53
- NVT Canonical ensemble. 53
- N_A Avogadro's number equal to $\approx 6.0221413 \times 10^{23}$. 9
- P Probability. 62
- $P(x \rightarrow x')$ Transition operator. 63
- T Temperature. 9
- V Volume. 56
- Δt Computational timestep. 67
- F Force. 46
- J Microscopic heat flux. 60
- J_D Diffusion flux. 57
- a Lattice vector. 32
- b Lattice vector. 32
- p Momentum. 52
- q heat flux. 9

- r Position Vector. 35
- v Velocity. 9
- δ Kronecker delta. 53
- ℓ Mean free path. 9
- η Dynamic viscosity. 26
- \hbar Reduced Plank's constant. 92
- κ_B Boltzmann constant which is approximately $\approx 1.3806488J/K$. 26, 53
- λ Thermal Conductivity. 9
- \mathcal{D} Degree of freedom. 55
- \mathcal{F} Arbitrary Integral. 62
- \mathcal{H} Hamiltonian. 53
- \mathcal{K} Kinetic energy. 55
- \mathcal{V} Potential. 45
- \mathcal{W} Virial stress. 56
- ω Frequency. 92
- ϕ Volume fraction. 25
- ρ Number Density. 9, 56
- σ Distance at which the Lennard-Jones potential crosses the axis. 46
- ε Depth of the potential well in a Lennard-Jones potential. 46
- ε_0 Permittivity of free space. 48
- c Concentration of a substance. 57
- f Arbitrary function. 62
- $g(r)$ Radial distribution function. 56
- $g(x \rightarrow x')$ Proposal operator. 64
- h Microscopic partial enthalpy. 61
- m Mass. 55
- p Pressure. 15, 56

q Charge. 48

x Real number. 35

y Real number. 35

Introduction

1.1 Passive Thermal Management

The constant demand for ever more sophisticated functionality in electronic systems has led to technological advances at an unprecedented rate. These developments often result in the generation of large heat fluxes, which increase the temperature of systems. In turn, this can potentially have devastating effects on their correct function—and even cause permanent damage. Removing excess heat is therefore a crucial aspect of the design and correct operation of devices.

Thermal Management refers to the regulation of a system's temperature to acceptable levels. A naive solution is to use pumps to increase fluid flow over the heated surface. Up to a point this can be effective. However, the additional consumption of power is often undesirable. Most research focuses on **passive** thermal management: cooling methods with no additional energy requirements. Such techniques attempt to increase heat transfer by exploiting the intrinsic properties of materials and optimising the geometrical structure of the devices.

Historically, simple heat sinks using conventional materials (e.g. copper) have been adequate in cooling down most devices. For more demanding applications, liquid cooling (instead of air cooling) could deal with the associated heat fluxes. However, as systems—particularly military systems where generation of heat can reach up to $1000W/mK$ —become increasingly demanding, traditional materials and methods have proven ineffective. Furthermore, in applications such as avionics, failure is unacceptable, rendering thermal management of paramount importance in the design of the avionics bay.

This urgent need for thermal management has kindled interest into research investigating possible solutions. The current investigation starts with a review of the literature to identify promising directions for improving heat transfer. Following this review, we focus on liquid cooling using nanofluids and flows through nanochannels.

1.2 Micro and Nano Flows

Micro and nanofluidics refer to fluids enclosed in geometries of micro and nano-meter-sized dimensions. Many disciplines, ranging from biomedicine [15–18] to electronics [19], use such structures. Furthermore, the invention of microchannel heat sinks [20] has promoted micro- and nano-flows for thermal management.

For engineering purposes, a large percentage of studies attempt to optimise the geometry of heat exchangers, assuming knowledge of the thermodynamic properties of the materials used. However, studies have shown that under severe confinement phenomena at the solid-liquid interface become increasingly important [21–23] and distort such macroscopic assumptions. Traditional models based on the Navier-Stokes equations tend to ignore such effects, or at best treat them based on empirical experimental observations [24, 25]. As a result they are inadequate for micro and nanofluidic systems [26–28]. The elusive nature of micro- and nano-flows, as well as the wide spectrum of possible applications has been a topic of academic interest over the last few decades.

1.3 Nanofluids

Nanofluids are suspensions of solid particles of nanometer-sized diameters in some fluid. They have been of keen interest recently as potential candidates for thermal management. Experimental studies on the heat transfer properties of nanofluids [29–31] observed thermal conductivities far exceeding those predicted by classical, effective-medium-based approximations [32, 33] which treat properties of composites as an average of those of their constituents, taking into account their volume fractions.

In an attempt to bridge theory and experiment, a number of disparate, speculated theories have arisen [12, 34–39], all of which have their advocates and critics. To date, there is a lack of consensus as to the heat transfer mechanisms that enhance the thermal conductivity of nanofluids beyond the realms captured by Fourier's laws and effective medium theory. It is therefore an open topic of significant academic and industrial interest.

1.4 Modelling fluids and nanofluids

Fluid dynamics have long been modelled using the Navier-Stokes equations. Their success in the design and optimization of macroscopic structures and devices (e.g. aircraft, automobiles, buildings) have established them as an effective method for studying fluid flow. This approach is based on the assumption of a continuum fluid which is in equilibrium within a

very small volume, a premise reasonable at larger scales. However, the restriction of fluids to nanometer-sized characteristic dimensions is accompanied by phenomena at interfaces such as large gradients which compromise the continuum assumptions.

Atomic scale simulation techniques such as Molecular Dynamics (MD) and the Monte Carlo (MC) method have proven effective in delineating, from first principles, the physical mechanisms that govern such systems. They have assisted in the resolution of discrepancies between experimental results and macroscopic computational models. Furthermore, the computational nature of these methods permits access to information unavailable in experiments. Such data can provide important details of the behaviour of the system rather than just calculating macroscopic properties.

The main disadvantage of atomic-scale simulation methods is their computational expense, which, despite various optimisation techniques, still increases dramatically with the number of atoms in the system. Complications arise in micro-flows where the non-homogeneities and interfacial effects of nano-flows are still evident, rendering continuum mechanics insufficient tools, while the system size is still outside the practical scope of MD.

This blend of difficulties in such systems renders the independent use of either continuum or atomistic methods insufficient or practically impossible. To account for this, mesoscale and Hybrid Molecular/Continuum Methods (HMCM) have been of academic interest for over two decades now. These attempt to bridge the two types of model into a synergy which allows for an accurate calculation of the properties of the system at an acceptable computational cost. Mesoscale models (e.g. lattice Boltzmann method, dissipative particle dynamics) comprise a single solver of intermediate resolution. This is usually achieved by introducing pseudo-particles that represent a large number of real atoms or molecules. Instead HMCM utilize both, a molecular and a continuum solver exchanging information. The main idea is that the simulation uses the expensive molecular component for small regions (decoupling length-scales) or limited amount of time (decoupling time-scales). Figure 1.1 pictorially demonstrates the time and length scales in which atomistic, continuum and hybrid methods are used.

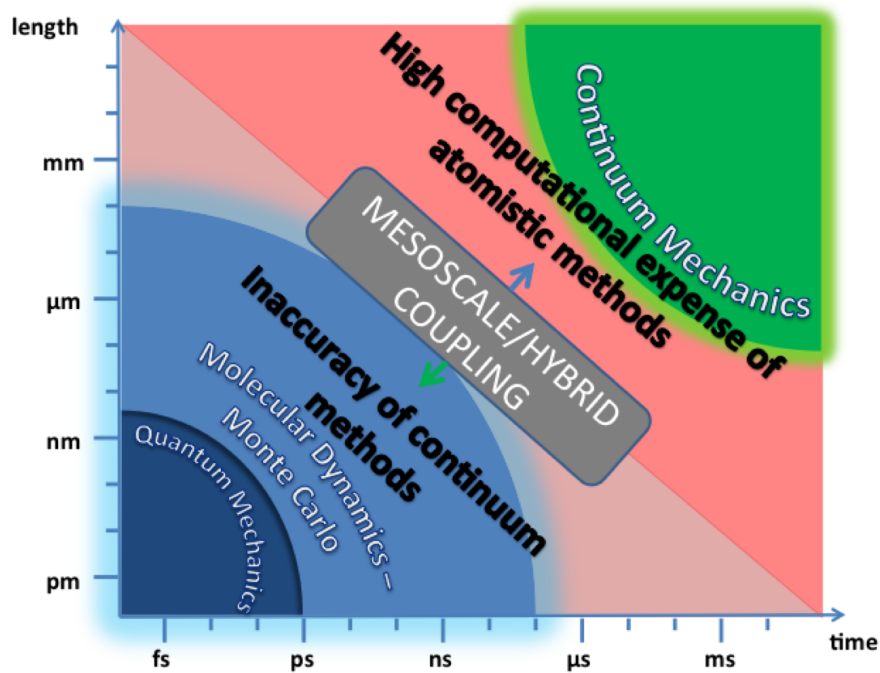


Figure 1.1: Representation of various computational methods for modelling fluids based on the length and timescales of the system

Although HMCM approaches are of greater practical use, at this stage our main objective is a deeper understanding of the physical behaviours and trends that the systems of interest exhibit. Therefore, the investigations carried out in this PhD concentrate solely on molecular computations, leaving hybrid based approaches as a necessary future endeavour.

1.5 Aims and Objectives

This PhD project started as a general study in passive cooling of electronic systems. As part of a larger project funded by BAE Systems, the top-level objective was to propose possible solutions to the overheating of electronics. Therefore, the mixed academic-industrial nature of this PhD required research which is both challenging, novel, and scientifically interesting, as well as having a direct vision as to its potential use.

The aims of the project are broken down as follows:

- Clearly identify the various cooling methods currently available as well as appreciate promising future candidates.

- Prepare computational models and design experiments to accurately study the cooling capacity of various technologies.
- Study the identified cooling technologies and clearly propose methods to improve current thermal management tools. These suggestions must be justified by computational and experimental results.

The objectives of the project are:

- Carry out a critical review of the literature in the broad field of thermal management. This should enable an educated convergence of the initially generic topic towards a focal point of study. The documentation of the findings of this review should also serve as a broad guide to promising cooling technologies.
- Develop relevant computational models in accordance with state-of-the-art methodologies as presented in the literature. In retrospect, this involved the development of MD models for nanoflows and nanofluids as well as accurate statistical techniques for obtaining meaningful data from the simulations.
- Design and conduct experiments to showcase the applicability of nanofluids in the context of thermal management. The experimental results have been presented to BAE Systems and have proven to be crucial for the industrial purposes of the project. However, their academic substance is limited and therefore this thesis will not include information on the experimental work carried out.
- Use the high performance computing facilities at Cranfield University to perform computer simulations on nanofluids and confined liquids
- Study the results of the computer simulations and provide a qualitative understanding of the physical behaviour of nanofluids and quantify how various circumstances and parameters can enhance their cooling capabilities

1.6 Publications

During the period of this PhD project, three conference papers have been written and presented. In addition, four papers have been prepared which will be submitted to peer-reviewed journals

- Conferences
 - M. Frank and D. Drikakis, “Investigation of the thermal conductivity of a Water-Copper nanofluid confined in a graphene nano-channel”, Microfluidics conference, Limerick, Ireland, 2014

- M. Frank, N. Asproulis and D. Drikakis “Thermal Conductivity of Nanofluids in Nanochannels” Micro and Nano Flows (MNF), London, UCL, 2014
- M. Frank, and D. Drikakis “Advances and challenges in computational research of micro and nano flows” Micro and Nano Flows (MNF), London, UCL, 2014
- M. Frank, D. Drikakis, N. Asproulis “Thermal behaviour of nanofluids confined in nanochannels” Micro and Nano Flows (MNF), London, UCL, 2014
- Journals (Under review)
 - M. Frank, D. Drikakis “Thermal Conductivity of Nanofluids in Nanochannels” Microfluidics and Nanofluidics
 - M. Frank, and D. Drikakis ”Advances and challenges in computational research of micro and nano flows” Microfluidics and Nanofluidics
- Journals (In preparation for submission)
 - M. Frank, D. Drikakis and N. Asproulis, “Crystal-like heat transfer of liquids in nanochannels”
 - M. Frank and D. Drikakis “Density effects on the ballistic heat transfer of confined liquids”
 - M. Frank, N. Asproulis and D. Drikakis “Thermal properties of a Water-Copper nanofluid in a graphene channel”
 - M. Kio, M. Frank, D. Drikakis, N. Asproulis and László Könözy, “Mass and stiffness effects on thermal resistance at the solid-liquid interface of nanofluidic channels”

1.7 Thesis Overview

Chapter 2 provides an overview of some of the most commonly researched areas for passive thermal management. Due to the general nature of the PhD, this review was an integral part of the project. Covering a relatively broad area of topics, it has guided the selection of specific areas to be investigated in depth. Additionally, it can be used independently as an introduction to effective thermal management techniques.

Chapter 3 provides the reader with information necessary for understanding and appreciating the models and results of this investigation. We have tried to keep this section as short as possible and it is by no means a detailed description of the disciplines included (i.e. crystallography, chemistry, statistical mechanics). Various subsections suggest relevant textbooks for a more detailed study. Although the topics discussed might initially seem disparate, they are all directly relevant to this thesis. The only exception to this is the section on the Monte Carlo simulations. Although the method has not been employed

here, we believe that a brief description is required to justify our decision to use Molecular Dynamics instead.

Chapter 4 describes the Molecular Dynamics studies on the thermal behaviour of confined liquids. The mechanism of heat transfer is identified to be different from that of unrestricted liquids. The remainder of the chapter describes how the system parameters can be altered to enhance the thermal conductivity of liquids in nanochannels.

Chapter 5 describes the Molecular Dynamics studies on the thermal behaviour of confined nanofluids. Two different nanofluids are studied. The first is a copper-argon nanofluid confined in idealised solid walls. The second is a copper-water nanofluid confined in graphene-based walls. These are initially investigated independently. The chapter however, concludes by drawing a line between the two indicating how the relationship of the materials used in the system can affect its thermal behaviour. We would like to mention that the research described in this section preceded that of chapter 4. In fact, some of the findings in this section directed our interest into the thermal behaviour of pure liquids (rather than nanofluids) under confinement. However, it is our opinion that this is a much more natural sequence to present our findings.

Chapter 6 wraps up this thesis by briefly stating its findings collectively. We appreciate that our research covers novel concepts that are still unresolved. Here we also list the next steps required to elevate these theoretical concepts to useful practices.

Thermal Management

2.1 Heat Transfer

The atoms and molecules of a system in equilibrium at a temperature above absolute zero are moving and colliding with each other stochastically. As the temperature rises, the motion becomes more vibrant and the collisions more violent. We refer to the kinetic and potential energy of a system due to its temperature as **thermal energy**.

Heat transfer is the transfer of thermal energy. This is not to be confused with the work done onto a system, where energy is transferred along with the collective, ordered motion of the atoms (rather than stochastic motion from collisions). The fundamental mechanisms of heat transfer are:

- Heat Conduction
- Convection
- Radiation

The following sections briefly describe these means of heat transfer.

2.1.1 Heat Conduction

Heat conduction is the transfer of energy across a system (or between systems in contact) in the presence of a temperature gradient. Atoms exchange energy by interacting with each other. The interactions might be direct atomic or molecular collisions, by transmission and absorption of electrons and through lattice vibrations.

Macroscopically, heat conduction is calculated using Fourier's law which is given by

$$\mathbf{q} = -\lambda \nabla T \quad (2.1.1)$$

where \mathbf{q} is the heat flux vector; λ is the thermal conductivity of the material; T is the temperature; and ∇T is the temperature gradient. The thermal conductivity is an intrinsic property of a material quantifying how efficiently heat is transferred through it.

In a fluid, heat is mostly transferred through direct collisions of atoms and molecules. Under a temperature gradient, the particles in regions of higher temperature are moving violently, colliding with the more relaxed particles in cooler regions. Each collision transfers some energy in the form of heat. This continues until the system has reached thermal equilibrium. For ideal gases the thermal conductivity is often described using kinetic theory by

$$\lambda = \frac{\rho \langle v \rangle \ell C_v}{3N_A} \quad (2.1.2)$$

where ρ is the number density of the liquid, defined as the number of liquid particles in a unit of volume; v is the velocity; and $\langle v \rangle$ is the average velocity, directly related to the temperature; ℓ is the Mean Free Path (MFP) of the particle, characterising the average distance travelled by the particles in between collisions; C_v is the specific heat at fixed volume; and N_A is Avogadro's number which is approximately equal to $6.0221 \times 10^{23} \text{ mol}^{-1}$

In metals, the main energy carriers are the electrons. The atomic structure of metals is characterised by delocalised electrons which are free to move between atoms. Under a temperature gradient the electrons in hotter regions have greater energy. These move to cooler regions transferring heat with them. Models, such as the free electron gas model, often describe the electrons in metals as a fluid moving over the positively charged cores. Under a temperature gradient, the electrons travelling from hotter regions have higher thermal energy than those in cooler regions.

Finally, in many non-metallic solids where electrons are not a significant energy carrier, uniform lattice oscillations transfer both kinetic and potential energy. Quantum mechanically, such atomic vibrations are often described by quasi-particles referred to as phonons.

2.1.2 Convection

Convective heat transfer is the transfer of energy through the bulk motion of a fluid. Owing to the usually low thermal conductivity of liquids and gases, convection is usually the dominant form of heat transfer in these states of matter.

2.1.3 Radiation

Radiation is the transfer of heat via electromagnetic waves. As matter heats up, the motion of its charged particles emits photons transferring energy over long distances. This means of heat transfer can even occur through a vacuum.

2.2 Conventional Heat Exchangers

2.2.1 Heat Sinks

A commonly used component for cooling electronic devices is the **heat sink**; a generic name for a device that conducts heat from its source and dissipates it into some fluid medium where it is removed through natural or forced convection. The efficiency of a heat sink is measured by its ability to transfer heat away from the device. It depends on various factors such as the materials used, the velocity and temperature of the fluid around it and geometrical design factors aiming to decrease the thermal resistance. In addition to efficiency, the cost, weight and volume of heat sinks are of critical importance for many applications [1].

The first consideration in the design of a heat sink is the choice of its material. Different materials possess a wide range of thermal conductivities (figure 2.1). As far as efficiency is concerned the higher the thermal conductivity the better. However, ease of manufacturing and application-specific constraints such as weight, space availability, power consumption, flow conditions and cost, often rule out many promising options. An example is diamond. Its thermal conductivity of 22000 W/mK is roughly five times that of copper. However its cost renders it a very impractical material for use in most thermal management applications. Furthermore copper, a material frequently used for cooling devices, is a relatively heavy metal. It is therefore not the optimal choice for applications such as aeronautics and the automotive industry, where additional weight is undesirable [1]. Therefore, aluminium alloys are often the choice of preference for thermal management devices in these fields.

Regardless of the extremely low thermal conductivity of plastic, which is roughly 0.2 W/mK, its low cost, weight and ease of manipulation and manufacture tantalizes engineers in thermal management. Studies on plastic composites have shown that traces of highly conductive materials, such as graphene fibres, can increase the conductivity of plastics up to 100 W/mK, a value comparable with that of aluminium [1].

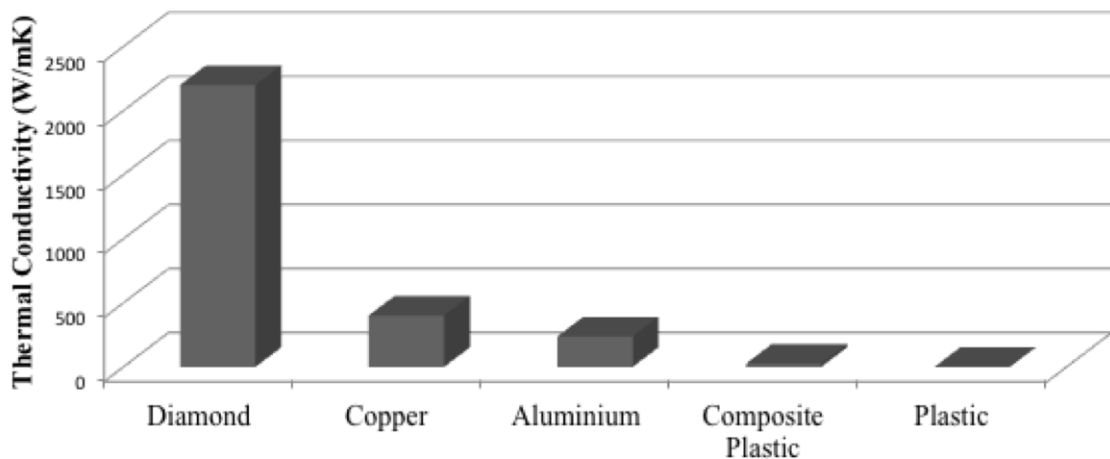


Figure 2.1: Thermal conductivity of heat sink materials. Reproduced from [1]

Phase-Change Materials (PCM) have also been used in the design of heat sinks [40, 41]. The idea is that during the melting of the material, much of the provided heat is used to change the state of matter rather than increasing its temperature. However, the thermal advantage provided lasts only during the melting period. It is therefore effective in applications where heat is generated within a small time-frame. Hybrid solutions have been considered in which only part of the heat sink is immersed in the PCM [40]. During periods of low convection, the PCM stores heat keeping the system temperature low. During higher flow rates, the conventional part of the heat sink is operational and can even cool down and re-solidify the PCM.

The geometrical design of the heat sink also contributes towards its thermal performance. The addition of fins, protuberances on the surface of the heat sink, can greatly reduce the thermal resistance of the system by exposing a greater surface area to the fluid medium. This, however, increases the pressure drop within the system, causing a reduction in flow velocity [1]. Therefore, an optimal design is achieved by carefully balancing heat transfer and fluid flow properties of the system. Analytical models [42, 43] have been introduced to evaluate the most efficient configuration of fins. These take into account the dimensions of fins as well as the materials they are made of.

The obvious bottleneck of traditional finned heat sinks is the low thermal conductivity of air. Liquids such as water, which possess higher thermal conductivities than air, are often employed as the fluid medium. Micro-channel heat sinks (figure 2.2a), in which a liquid is pumped through channels of micrometer-sized characteristic dimensions, have been increasingly used since their invention [20]. As with fin heat sinks, the design of the micro channels is a compromise between thermal resistance and pressure drop. Various analytical [44–46] and numerical [47, 48] methods have been introduced to optimise the dimensions of the channels to achieve maximum thermal performance.

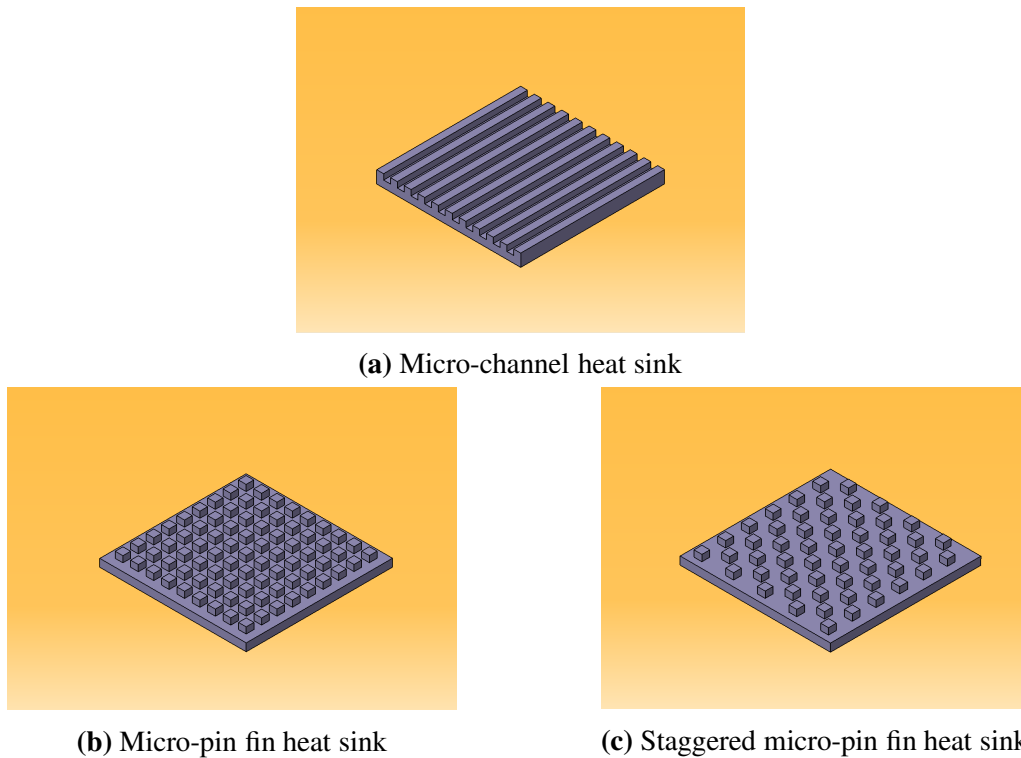


Figure 2.2: Cross-section of some heat sink designs. The micro-channel heat sink (2.2a) has continuum grooves through which the liquid can flow. Instead, micro-pin fin heat sinks can have discrete protuberances exposing a greater surface area to the fluid. These can be either aligned (2.2b) or staggered (2.2c)

Micropumps, pumps that operate in the micro-meter range, can potentially overcome the pressure drops resulting from frictional forces in microchannels [49]. They are cheap to run since they do not operate based on mechanical phenomena. However, their performance is often inadequate [50]. Integrated micropumps are often proposed instead, which use various techniques such as electrohydrodynamics to drive the flow of the liquid [50, 51].

Advances in micro-fabrication technologies have also enabled the design and manufacture of micro-pin fin heat sinks. These have rows of discrete extrusions rather than continuous walls that form channels. The pins can either be aligned (figure 2.2b) or staggered (figure 2.2c). Micro-pin fin configurations have lower thermal resistances than micro-channels [52], especially at high flow rates. Beyond 60 g/min the flow becomes turbulent enabling a greater surface area to be exposed to the liquid [53]. However, a significantly greater pressure drop accumulates due to the collision of the liquid with every single pin [53, 54]. Adjusting the shape of the pins (i.e. airfoil shape) can decrease the pressure drop in the system [54].

The high surface to volume ratio in micro-channel/micro-pin-fin exchangers introduces a problem. The small volume of the fluid can heat up rapidly. In turn this introduces temperature fluctuations within the channel. Due to the different thermal expansion coefficient

of the various parts of the heat sink and device this can have devastating effects [55]. The obvious solution of increased liquid velocity is often unacceptable due to the additional power requirements. Two phase flow is an alternative option in which, as with PCMs, the heat of vaporisation absorbed by the liquid during the phase change does not increase the temperature of the system. Fluids with a low boiling point, such as Vertrel FX, have been used to successfully minimise any temperature gradients compared to single-phase water [55]. Two-phase heat transfer has also been studied in micro-pin-fin heats sinks [56] and was found to improve the heat transfer coefficient compared to single-phase flows.

2.2.2 Heat Pipes

Heat pipes are two-phase thermal management devices which use phase change to carry heat across locations of different temperatures. In its most basic form, as shown in figure 2.3, a heat pipe consists of a tube, only partially filled with liquid. Heat is applied to one end of the pipe, known as the evaporator section, causing the liquid to vaporise, absorbing latent heat. In turn, a build up of pressure caused by the temperature difference between the two ends, pushes the gas towards the other end, called the condenser section. The lower temperature causes the gas to condense back into a liquid. The latent heat absorbed earlier is now released and dissipates outside the pipe, usually through a heat sink. The liquid then returns to the evaporator to repeat the cycle.

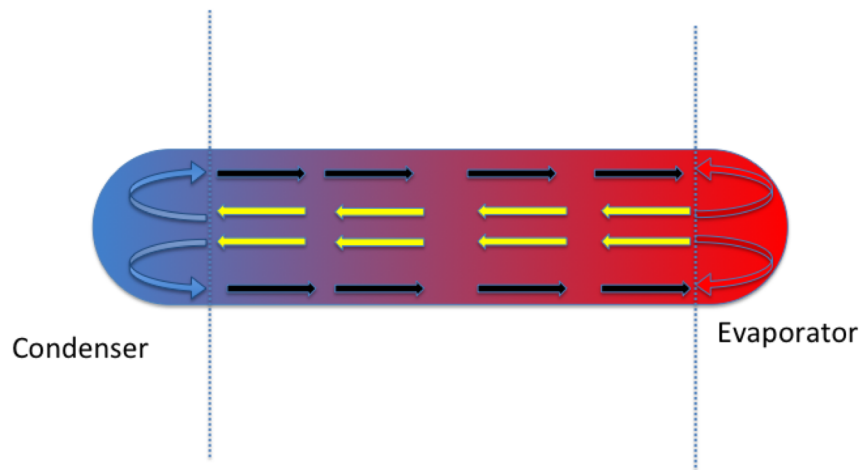


Figure 2.3: A simple heat pipe

The main challenge in the design of a heat pipe is the efficient return of the fluid from the condenser back to the evaporator. Usually porous structures, known as wicks, are installed along the entire length of the heat pipe. The liquid is pumped through the wick non-mechanically. This is achieved by capillary action, the motion of a liquid through confined spaces as a result of the adhesive, solid-liquid forces and the surface tension of the liquid.

Studies have considered various designs attempting to make such cooling devices work efficiently under various conditions and orientations [57]. The main issue with the basic design of figure 2.3 is that decreasing diameter of the wick pores, necessary to provide sufficient capillary forces, results in large pressure drops. This compromise restricts the use of such devices to distances usually < 0.5 m when the return of the liquid is fighting against gravity [58].

A variation of the conventional heat pipe is the Loop Heat Pipe (LHP) [2, 59, 60]. The basic principle of carrying and releasing excess heat through the vaporisation and condensation of a fluid remains the same. However, the design and operation of LHPs are significantly more complicated, allowing such devices to operate over much larger distances and over various orientations within a gravitational field. The main components of a LHP are the evaporator, condenser, and liquid and vapour lines. The evaporator, which is the most complex part of the entire system, consists of a primary and secondary wick, a vapour chamber and a compensation chamber. Figure 2.4 schematically shows a simple configuration of a LHP. The figure aims to highlight the main components of these devices and is not an accurate representation of the exact positioning of all the components.

There are two main differences between the LHP and conventional design. The first is that the vapour and liquid flow through different lines, which together form a closed loop. This eliminates any viscous influences between the two states of matter. The second difference is that the wick structure is located only in the evaporator with the remaining tubing being made of smooth walls. Both characteristics reduce the pressure drop considerably, allowing for the pumping of the liquid/fluid to be achieved over significantly larger distances.

In the absence of a heat flux, liquid is only filling the liquid line and evaporator. The wick is entirely saturated [58]. Once heat is applied to the evaporator, the liquid in the wick vaporises inside the vapour chamber and compensation chamber. The thermal resistance of the wick prevents heat from travelling back to the condenser. The vapour then starts applying pressure both towards the wick and the vapour line. The capillary pressure at the wick prevents the vapour from moving backwards into the compensation chamber, and forces it to move towards the condenser via the vapour line. Designing a wick with small pore diameter increases the capillary pressure for the circulation of the fluid. This is, however, the theoretical, maximum pressure that the wick can apply. It is the vapour pressure that will push against the menisci of the wick to initiate the desired mass flow. As the vapour moves around the line, it condenses (at the condenser) via an external heat exchanger and is pushed into the compensation chamber. At that point, the secondary wick transfers the liquid into the primary wick to repeat the cycle.

The compensation chamber is a crucial part of the LHP. Its first task is to store excess liquid, ensuring that the primary wick is continuously saturated (through the secondary wick) under any heat load intended for the device. This enables the LHP to be ready at any time to start the cycle. Usually, the volume of the compensation chamber and the total amount of liquid in the system are adjusted to satisfy the following conditions [2]

- Under no heat load, the compensation chamber should have some liquid even when the rest of the pipe is flooded
- At the highest possible operating temperature some vapour space is available in the compensation chamber.

Because the heat load is applied closer to the vapour chamber, the temperature and pressure of the compensation chamber is lower. Furthermore, due to the subcooled liquid returning to the compensation chamber from the condenser, its temperature further decreases. In turn, different saturation temperatures exist between the two components, giving rise to the thermodynamic relation [2, 58, 61]:

$$\Delta p_{cc} - \Delta p_w = \left. \frac{dp}{dT} \right|_{T_{cc}} (T_e - T_{cc}) \quad (2.2.1)$$

where p is the pressure; and the subscripts cc and w stand for compensation chamber and wick; T_e is the temperature at the evaporator and T_{cc} is the temperature in the compensation chamber at the liquid-vapour interface. The derivative $\frac{dp}{dT}$ corresponds to the gradient of the saturation line (on a pressure-temperature diagram) for the working fluid. The equation states that a pressure difference between the compensation chamber and vapour chamber should correspond to two saturation temperatures whose pressure difference is the same. This indicates that the temperature of the compensation chamber can control the operating temperature of the LHP.

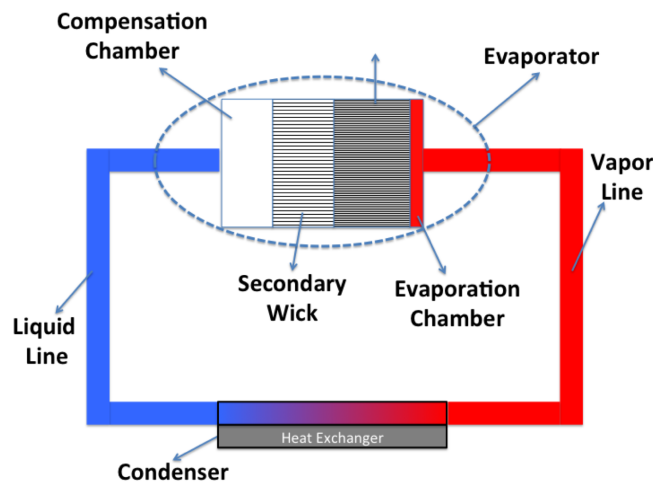


Figure 2.4: A loop heat pipe

The choice of working fluid is an important parameter in the design of a LHP. A liquid with high thermal conductivity will increase the heat transfer capacity of the system[62]. However, other liquid properties such as the absolute vapour pressure, and the freezing and

boiling point must be tailored to each application [63]. Common working fluids are ammonia and water. The low saturation temperature of ammonia keeps the operating temperature in the evaporator lower than water for heat loads $< 55\text{ W}$ [62].

However, for applications such as satellites, the freezing point of liquids such as ammonia is too high. Other liquids such as propylene can be used, although under normal conditions (higher heat loads) ammonia can outperform propylene four-fold [64]. LHPs have also successfully been utilized under cryogenic temperatures ($4\text{ K} < T < 70\text{ K}$) using working liquids such as nitrogen, neon, hydrogen and helium [65]. In addition to thermal properties of the working liquid to be used, the compatibility between the liquid and the materials making the LHP should be considered.

It is also interesting to study the performance of LHPs as a function of the heat load at the evaporator. Intuitively, one expects that as the heat load increases so does the temperature in the evaporator. Indeed, some experiments have found exactly that [66]. Other studies however, have shown that for lower heat loads, an increasing power is presented with an initial decrease in the evaporator temperature [2, 3, 67] (figure 2.5). The explanation is that the condenser is fully capable of removing the low heat load entering the system. The bottleneck is therefore the low mass flow. Increasing the heat entering at the evaporator increases the mass flow and in turn, reduces the operating temperature of the LHP. This decrease continues up to the point where the heat in flux is greater than the possible heat removal. Once the condenser has reached its full capacity, the temperature at the evaporator will steadily and linearly increase with increasing power load.

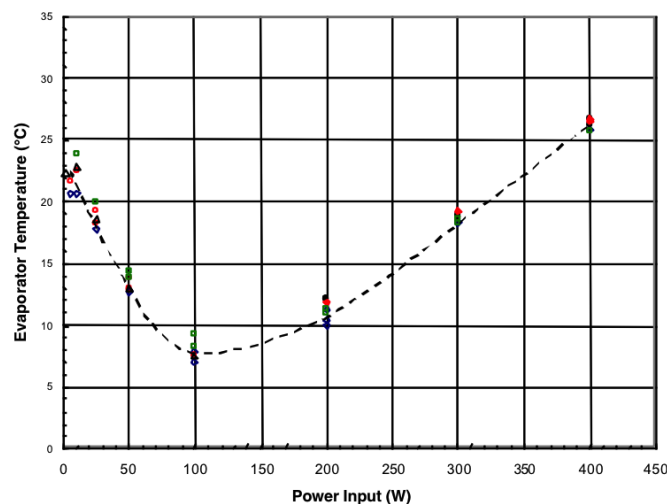


Figure 2.5: The temperature of the LHP evaporator as a function of the heat load. Reproduced from [2, 3]

The different behaviour in the operating temperatures discussed above is attributed to the heat sink and ambient temperature [67]. Generally, the lower the heat sink temperature,

the lower the LHP operating temperature. Of course this is only true as long as the heat sink is cooler than the surrounding environment [2]. If not, heat will flow from the ambience into the liquid, increasing the temperature of the system.

The length and diameter of the vapour and liquid lines can also affect the performance of the LHP. Shortening the vapour line and increasing its diameter can significantly decrease the pressure drop of the system, leading to higher convection rates [68].

2.3 Carbon allotropes

2.3.1 Introduction

Carbon is one of the most interesting and important elements in the periodic table. Its chemical properties and ability to form complicated networks are fundamental to organic chemistry and the existence of life. It can be found in many different structural configurations called **carbon allotropes**. Some of these, such as diamond and graphite, have been known since ancient times. Others however, such as Carbon Nanotubes have been artificially engineered in the last few decades.

Carbon allotropes are being increasingly used due to their electrical and mechanical properties. Additionally, they have shown extraordinary thermal properties with thermal conductivities ranging between $0.01 \geq \lambda \leq 3500$ W/mK. The following review on carbon allotropes will focus on their thermodynamic properties.

2.3.2 Overview of common carbon allotropes

Carbon allotropes differ in the geometrical arrangement of the carbon atoms and the atomic bonding between them. These two factors have a surprising effect on the dynamics of the material.

Amorphous forms of carbon, such as amorphous diamond and diamond-like carbon are materials that lack symmetry. They tend to have very low thermal conductivities as the lack of structure enables scattering of phonons across imperfections.

As symmetry is introduced, properties of carbon allotropes become more interesting. The atoms in diamond are arranged on a **face-centered cubic** structure (discussed in section 3.1). Graphite is an array of planes, the atoms of which form a hexagonal arrangement. Depending on the quality and structure of the planes, the properties of graphite vary significantly. Highly-Oriented Pyrolytic Graphite (HOPG) is an artificial, nearly-perfect

graphite sample. It is obtained through annealing of its natural form. Due to the lack of impurities HOPG has various properties of interest in many fields.

In addition to having interesting properties, graphite is also the base for graphene and carbon nanotubes (figure 2.6). Its basal plane, a single layer of carbon atoms in a hexagonal tessellation, constitutes the two-dimensional material **graphene**. The synthesis of graphene is quite complicated due to stability issues [69]. Its extraction was only achieved over the last decade by extracting a single layer of atoms from graphite, using a technique called micromechanical cleavage [70].

In a similar manner to Graphene, a Carbon Nanotube (CNT) is a hexagonal arrangement of carbon atoms within a plane. However, the plane is folded into a cylinder, reducing it into a one-dimensional material. CNTs are generally categorised into Single-Walled Carbon Nanotube (SWNT), which consist of only one cylinder, and Multi-walled Carbon Nanotube (MWNT) in which a number of cylinders of decreasing diameters are embedded inside each other.

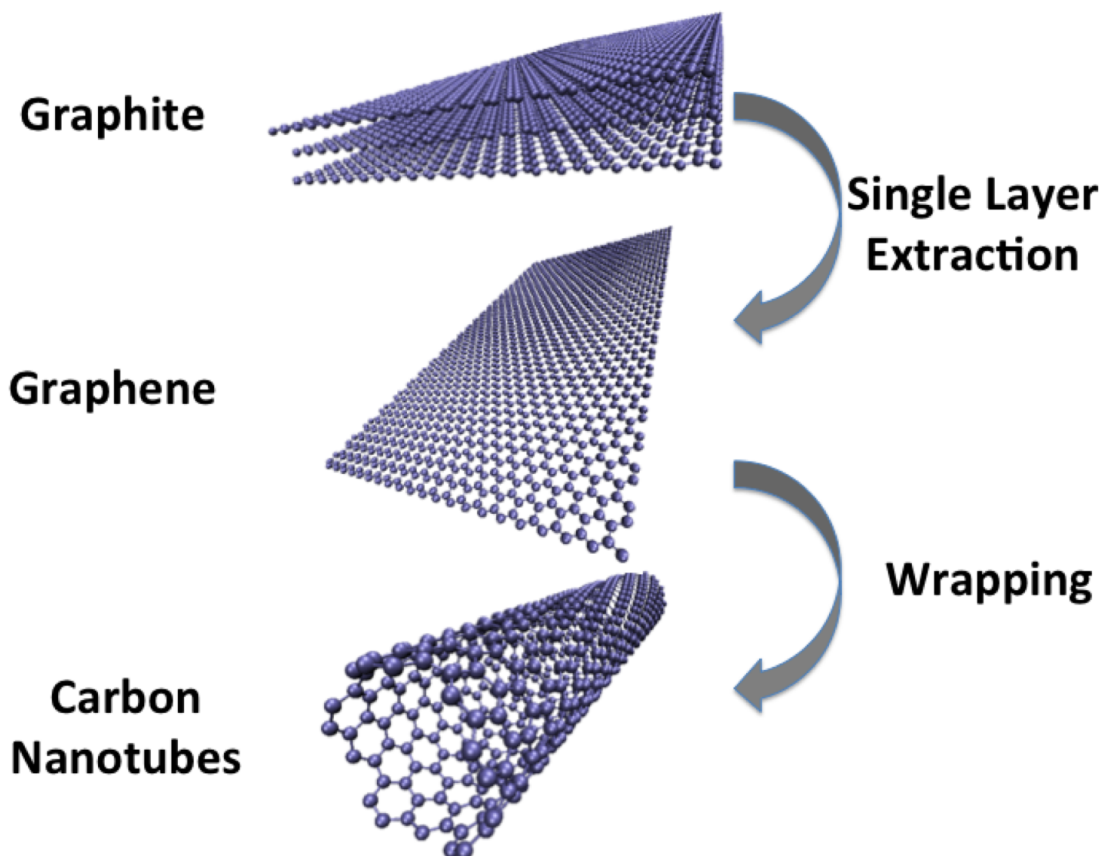


Figure 2.6: Derivation of graphene and CNTs from graphite. Graphene is a single atomic layer extracted from graphite and a single CNT is a rolled up graphene sheet

An individual CNT is characterised by the orientation in which the sheet of graphene

is rolled up. Consider for example a rectangular sheet. This can be rolled parallel to the width. Alternatively, it can be rolled at some angle. Conventionally, this is described by a pair of indices (n, m) . These correspond to a number of lattice units in each direction, i.e. a vector on the graphene plane. This vector indicates pairs of atoms that will coincide when the sheet is rolled up into a nanotube.

2.3.3 Theoretical overview of heat transfer in carbon allotropes

Phonons are the main heat carriers in carbon allotropes. Their energy and mean free path depends on the strength of the bonds between atoms, the symmetry of the configuration, and the number of impurities and dislocations.

Amorphous types of carbon tend to have very low thermal conductivities. This is related to the high frequency of scattering events resulting from the lack of symmetry. Materials such as amorphous diamond and diamond-like carbon have been found to possess thermal conductivities as low as $5 < \lambda < 10$ W/mK and $0.3 < \lambda < 1$ W/mK respectively [71], the latter being comparable to those of liquids. As symmetry is introduced, the heat transfer capacity is enhanced significantly. Pure isotropically enriched diamond demonstrated thermal conductivities of up to 41000 W/mK [72].

Phonons behave differently under different temperatures. This introduces a temperature dependence in the thermal conductivity of carbon allotropes. Graphite and diamond reach a maximum thermal conductivity at ≈ 150 K after which it decreases [4, 73, 74]. The initial increase is attributed to the increasing phonon Density of States (DOS) [75], the number of states available for occupation at each energy level. The thermal conductivity decreases past ≈ 150 K due to increased phonon-phonon scattering, called **Umklap scattering**. This is more pronounced for high energy phonons.

The thermal conductivity of CNTs keeps increasing for much higher temperatures. As figure 2.7 demonstrates, aligned CNTs show an increase in the range between $8 < \lambda < 400$ K with a thermal conductivity of ≈ 200 W/mK at room temperature. The linear progression of the curve at temperatures below 30 K is believed to be a product of quantum mechanical effects. The decreased slope after 300 K is an indication of increased Umklap scattering. The unaligned SWNTs have a greatly reduced thermal conductivity of ≈ 35 W/mK at room temperature due to increased scattering events at the junctions of the tangled nanotubes [4, 75].

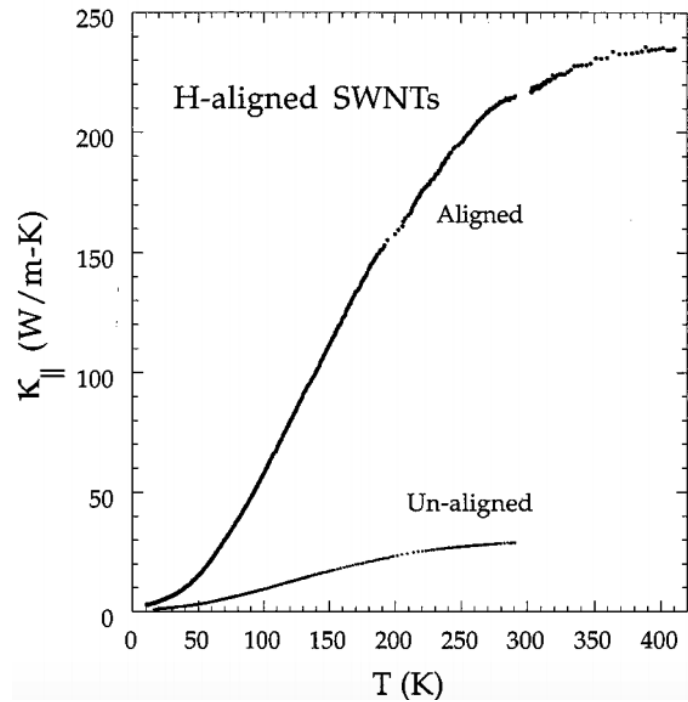


Figure 2.7: Thermal conductivity of aligned and Unaligned SWNTs as a function of the temperature. Reproduced from [4]

Early studies of the thermal conductivity of MWNTs found it to be ≈ 25 W/mK [76]. The low value is explained by scattering due to the contact between the tubes as well as the quality of the samples used [75]. Subsequent studies used more accurate methods for calculating the thermal conductivity of a single MWNT [5]. They have calculated a thermal conductivity of ≈ 3000 W/mK at room temperature [5]. Figure 2.8 shows the thermal conductance (extensive quantity) and thermal conductivity of the MWNTs presenting a behaviour similar to that of the SWNTs.

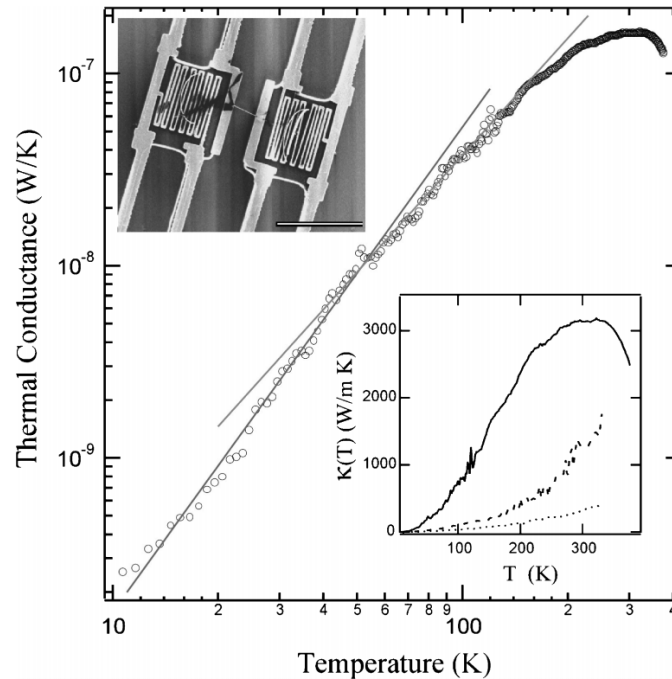


Figure 2.8: Thermal conductance and thermal conductivity (inset) of a single MWNT as a function of the temperature. The image at the top left is the structure used for the calculation of the thermal conductivity. Reproduced from [5]

Computational models have also been used to study the temperature dependence of the thermal conductivity of carbon allotropes [6, 77]. MD studies of an individual (10,10) SWNT has shown an initial increase in the thermal conductivity which peaks at 100 K and then decreases [6] (figure 2.9). The results show a maximum value of 37000 W/mK. This is close to the highest thermal conductivity ever recorded (41000 W/mK for a 99.9% pure isotopically enriched diamond [72]). The room temperature conductivity of the SWNT has been found to be 6600 W/mK. This value far exceeds the thermal conductivity of commonly used materials such as aluminium and copper.

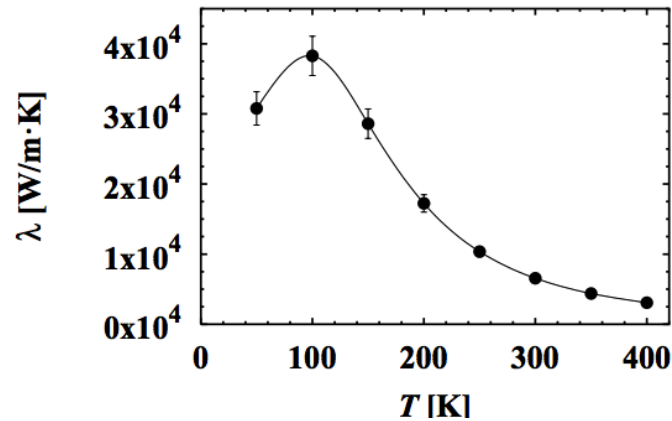


Figure 2.9: MD calculations of the thermal conductivity of a (10,10) SWNT. Reproduced from [6]

Comparing graphite, graphene, and SWNTs, which are made out of the same building blocks, can show the sensitivity of the thermal conductivity to the structure. The results from MD studies show that the three possess similar but different thermal properties [6] (figure 2.10). Graphite has the lowest thermal conductivity due to the phonon interactions between the basal (graphene) planes. Studies reached similar conclusions by studying Few-Layer Graphene (FLG) [78] – only few parallel graphene layers (not enough to be called graphite). Their results show that the thermal conductivity at room temperature decreases from 2800 W/mK to 1300 W/mK as the number of layers increases from 2 to 4.

On the other hand, CNTs have a low phonon DOS at low temperatures, due to their one-dimensional structure. This is reflected in the results shown in figure 2.10 where the thermal conductivity of SWNTs below 300 K is significantly lower than that of graphene. At higher temperatures, graphene and CNTs have similar DOS and the thermal conductivity is therefore of comparable magnitude [75].

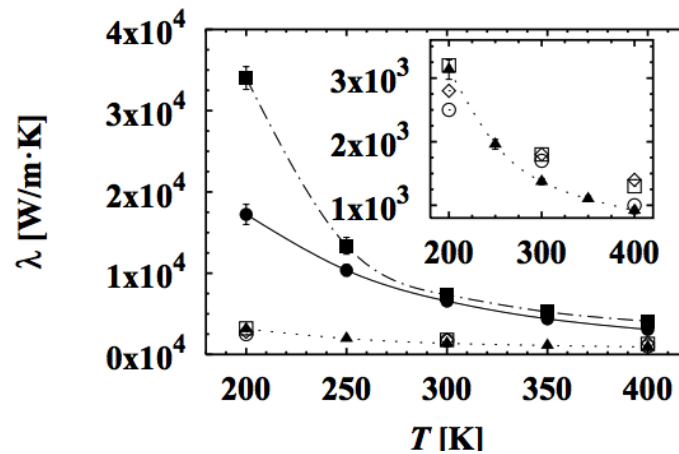


Figure 2.10: Comparison between the thermal conductivities of 3D graphite (the lower, dotted line), 2D graphene (the top, dash-dot line), and 1D SWNTs (the middle, solid line). The inset compares experimental measurements [7–9] for graphite with the results of the simulations . Reproduced from [6]

The honeycomb structure of graphene, also gives it anisotropic thermal properties, as a result of different phonon group velocities [10] in the various directions. In figure 2.11 the thermal conductance is shown as a function of the angle of the heat flux on a sheet of graphene under a temperature of 100 K showing a variation of 1%.

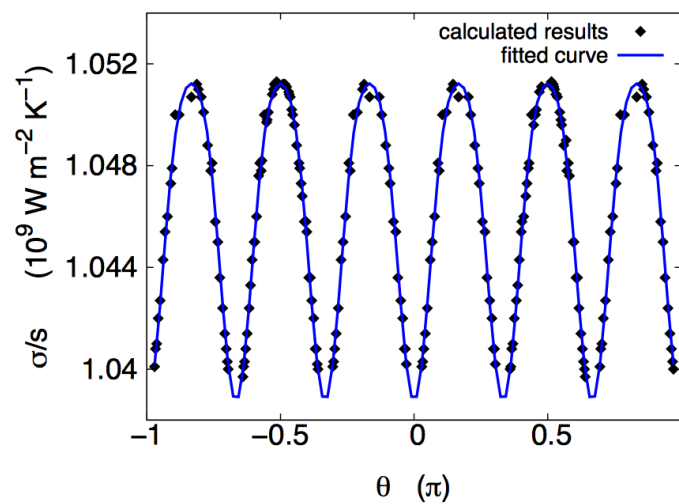


Figure 2.11: Periodic nature of the thermal conductance of a sheet of graphene. It is shown that as the angle of the heat flux on the plane changes, the conductance is oscillatory with a period of $\frac{\pi}{3}$. Reproduced from [10]

The majority of models assume perfect crystals. However, it is of practical importance to understand how defects and vacancies affect the thermal conductivity of carbon

allotropes. This reflects a more realistic representation of such materials. Dislocations are expected to be detrimental for the one dimensional CNTs since the lack of degrees of freedom restricts phonons from circumventing impurities. However, it has been shown that their effect is not much more severe than that in diamond [79]. This unexpected outcome is attributed to strong covalent bonds in CNTs which provide additional paths for phonons to bypass imperfections[80].

Accurate experimental measurements of carbon allotropes are usually obtained by having the materials suspended. When materials such as graphene come in contact with a substrate, their heat transfer capacity can be greatly reduced [81, 82]. The thermal conductivity of a single layer of graphene drops from its maximum suspended value ($3000 \text{ W/mK} \geq \lambda \leq 5000 \text{ W/mK}$) to 600 W/mK when it is in contact with a silicon substrate. This reduction is explained by a “leakage” of phonons at the interface [81].

Carbon allotropes are increasingly being used in polymer (i.e. epoxy resin) composites as thermal interface materials. Studies have shown that even a small percentage of MWNTs mixed into a polymer can greatly increase its thermal conductivity [83]. For example, even a mere 5% of FLG flakes in epoxy enhanced its thermal conductivity by $\sim 1000\%$ [84].

FLG has also been shown to perform well as a heat exchanger in circuits. Models using the Finite Element Method (FEM) have shown that the addition of FLG on silicon-based circuits managed to reduce the temperature of “hot spots” — spikes in the temperature profile of a surface — by 70 K [85].

2.4 Nanofluids

Scientists have long known that the addition of solid particles in a liquid can enhance the liquid’s thermal conductivity [32]. The idea is quite simple: since solids have higher thermal conductivity than liquids, the addition of solid particles must surely enhance the thermal properties of the base fluid. Prior to the advanced manufacturing techniques currently available, particles could only be scaled down to mili- and micro-meter sized dimensions. Such dimensions are not ideal as they can cause severe problems such as abrasion and clogging. The availability of nanoparticles (particles of nano-meter sized dimensions) enabled the engineering of **nanofluids**[86], suspensions of these solids into a base liquid. Nanofluids can enhance thermal conductivity of liquids while avoiding the problems that arise with larger particles.

2.4.1 Mechanisms for Enhancement of Thermal Conductivity

Initially, effective medium theory was used to calculate the thermal conductivity of nanofluids [87]. This method is established for the calculation of properties of solid-composites. Here, it evaluates the thermal conductivity of the nanofluid by considering those of the liquid and solid individually, and taking into account the percentage of each within the total system. Its initial form, as given by Maxwell, is

$$\lambda_{MAXWELL} = \frac{\lambda_p + 2\lambda_l + 2(\lambda_p - \lambda_l)\phi}{\lambda_p + 2\lambda_l - (\lambda_p - \lambda_l)\phi} \lambda_l \quad (2.4.1)$$

where λ_p is the thermal conductivity of the material of the particle, λ_l is the thermal conductivity of the liquid and ϕ is the volume fraction of the particles within the system. Subsequent models have attempted to improve this by accounting for the particle shape [33], distribution [88] and interactions between the particles [89].

Here, we refer to models adhering to the conventional wisdom of Maxwell's formulation as "classical". Such models suggest that the total thermal conductivity of the nanofluid can be broken into the independent properties of the constituents making it. There are no dynamic or static effects resulting from the combination of the two. Studies however, have shown discrepancies between experimental observations and the predictions of these models. The measured thermal conductivities far exceed those calculated by equations similar to 2.4.1 [29–31]. Experiments have also identified relationships which are absent from theoretical models. For example experiments have shown an inverse relationship between the particle size and the thermal conductivity (at a constant volume fraction) [90–92]. Furthermore, studies show that the thermal conductivity depends on the system temperature [93–96]. Both observations come in conflict with Maxwell's theory.

Investigations have proposed various mechanisms attempting to bridge experimental measurements with the theoretical framework. These are [34]:

- The Brownian motion of the particles [11, 34, 36]
- Nanoconvective effects within the liquid, as a result of the particle motion
- Structured liquid layering around the particles with higher thermal conductivities
- The formation of particle chains providing paths of low thermal resistance.

Brownian motion refers to the seemingly random motion of the suspended nanoparticle. This is a product of the various stochastic collisions with the liquid molecules. Initial investigations suggested that the Brownian motion causes collisions between the solid particles [97]. Each collision transfers energy which is not included in classical models. Instead such models [11] correlate the enhancement in thermal conductivity to the diffusion coefficient given by the Einstein-Stokes equation

$$D = \frac{\kappa_B T}{(6\pi\eta r_p)} \quad (2.4.2)$$

where κ_B is the Boltzmann constant; η is the dynamic viscosity of the base fluid; and r_p is the radius of the particle. The relation also correlates the thermal conductivity with the temperature of the system — a step towards reconciliation with the experiments. Calculations using such models agree with experimental data [11] (figure 2.12).

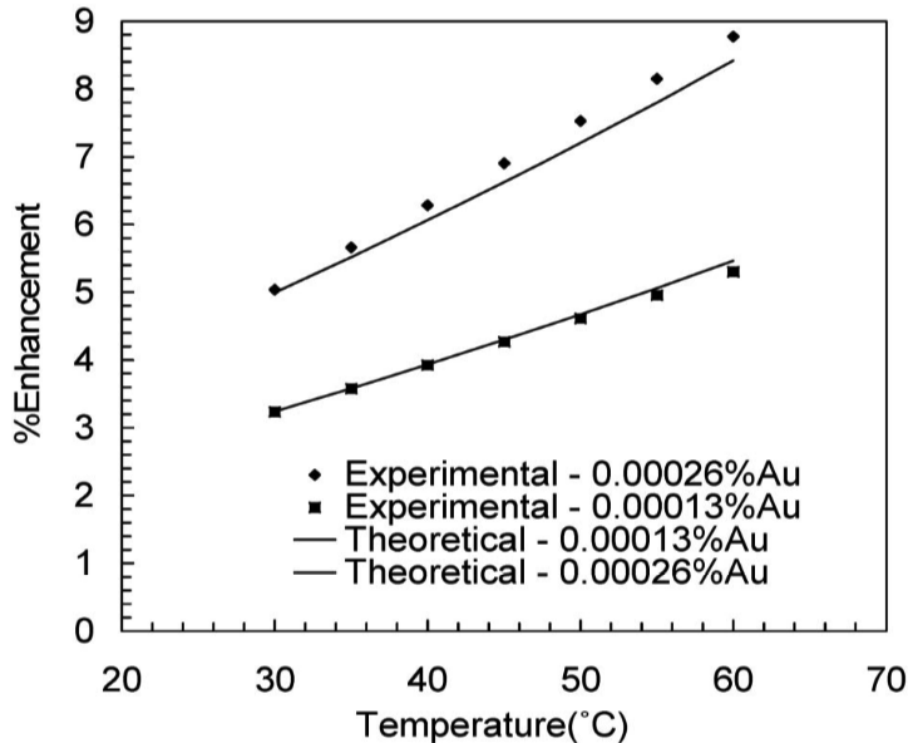


Figure 2.12: Thermal conductivity enhancement as a function of the temperature. The model based on the Brownian motion of the nanoparticles (straight lines) is compared with experimental data. Reproduced from [11]

Despite their initial success, later studies have criticised Brownian motion-based models [12, 34, 35, 98]. The main argument is that the diffusion of the nanoparticles is an order of magnitude slower than that of the fluid. Therefore, their collisions cannot possibly contribute enough to account for the enhancements observed. The agreement of these models with experiments has been attributed to the unrealistic mean free paths given to the nanoparticles ($\approx 1\text{cm}$). Therefore, the direct effect of the particle's motion has been deemed negligible.

Other studies suggested that indirectly, its trajectory might initiate convective effects within the liquid which is the missing source of thermal conductivity. Various models [99, 100] take such effects into account by involving the Nusselt and Prandtl numbers into the effective thermal conductivity of the nanofluids [35, 101]. The models match experimental

results very well [35]. Yet, other studies still consider such effects insignificant [12].

Experimental observations using X-ray reflectivity have shown that liquid molecules tend to form structured layers around the nanoparticles [102]. These have a structure resembling solids and are therefore expected to have higher thermal conductivities. The “classical” formulations do not take into account such phenomena. Theoretical models have attempted to incorporate this layering in equation 2.4.1, by considering a “pseudo” particle. This is composed of the nanoparticle and the spherical liquid layers around it [37, 103, 104]. However, such models often assume a layer of up to $5nm$ thick. Furthermore, they assign these layers a thermal conductivity of about 10 times that of the liquid [37]. Such assumptions contradict experimental observations, which show a thickness of only a few molecular dimensions [105–108]. Furthermore, experiments using well dispersed particles of $4nm$ in diameter have contradicted the predictions of such models [109].

Others have theorised that the electrostatic interactions between the nanoparticles and liquid might contribute to the thermal conductivity of the suspension. Experimental studies [110] on the surface charge of nanoparticles have shown that the pH of the nanoparticles strongly affects the thermal conductivity. More specifically, it has been shown that as the pH of the surface diverges from the isoelectric point (the pH level in which the net charge is zero) the thermal conductivity is enhanced.

The model described by equation 2.4.1 assumes a nanofluid with well and uniformly dispersed nanoparticles. Experimental observations show that nanoparticles tend to agglomerate (figure 2.13). Thus, the assumption of a uniform colloid cannot be generalized [12]. Some researchers believe that the grouping of nanoparticles can affect the thermal conductivity [12, 34]. Furthermore, this effect depends on the way in which the nanoparticles are connected.

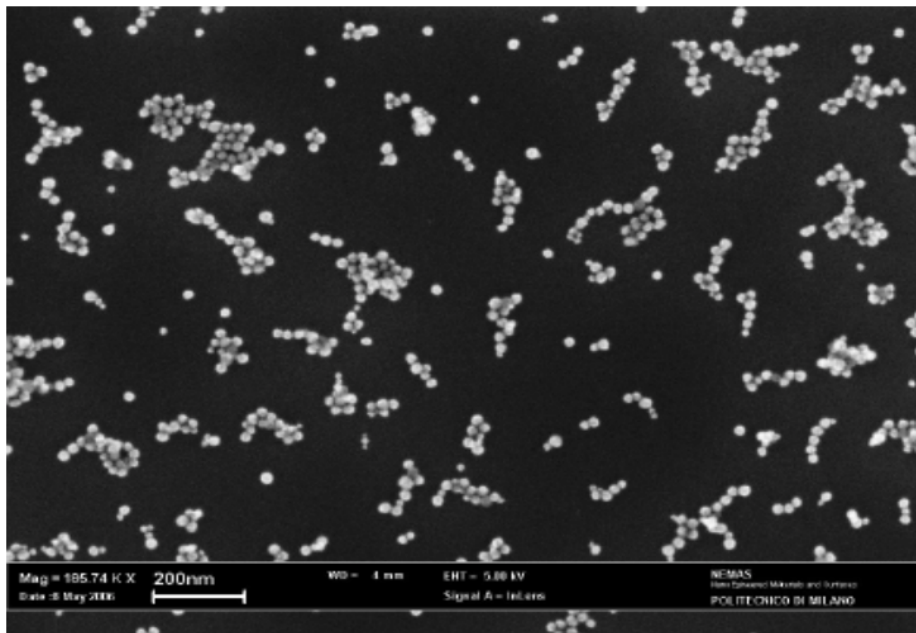


Figure 2.13: SEM picture of Ludox (silica) nanofluid, indicating clustering of nanoparticles. Reproduced from [12]

These studies believe for an arbitrary distribution of particles (i.e. not uniform) the classical model has in fact an upper and a lower limit (this is also correct for solid composites). The best configuration is one in which the nanoparticles are neatly arranged in parallel with the direction of the heat flow (figure 2.14b). The worst case is when the particles and liquid are arranged serially (figure 2.14a). These two modes constitute strict upper (parallel) and lower(serial) limits to the thermal conductivity of the nanofluid[111].

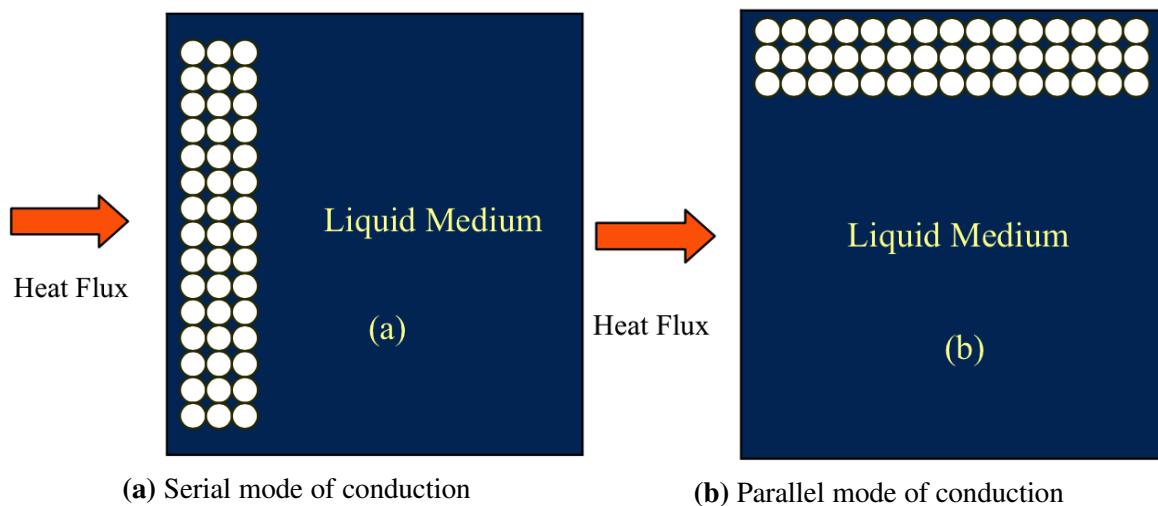


Figure 2.14: Serial and parallel modes of conduction. The former represents the absolute lowest thermal conductivity limit while the latter represents the absolute highest possibility. Reproduced from [12]

These modes are ideal, extreme cases which do not accurately reflect the the distribution of nanoparticles in nanofluids. Instead a more relaxed set of bounds has been derived given by [112]

$$\lambda_f \left(1 + \frac{3\phi[\lambda]}{3\lambda_f + (1 - \phi)[\lambda]} \right) \leq \lambda \leq \left(1 - \frac{3(1 - \phi)[\lambda]}{3\lambda_f - \phi[\lambda]} \right). \quad (2.4.3)$$

The boundaries provided by equation 2.4.3 contain almost all (if not all) the experimental observations of the thermal conductivity of nanofluids. In addition, all experimental measurements on well dispersed nanofluids have conductivities predicted by Maxwell's model. Therefore some researchers are convinced that the thermal properties of nanofluids are not anomalous and in fact behave in a manner similar to all composites [12].

2.4.2 Nanofluids for Thermal Management

Most of the research on nanofluids revolves around the physical interpretation of their thermal conductivities. However studies have also focused on their possible applicability for thermal management.

Nanofluids have proven to be excellent coolants through microchannels, providing cooling rates of $\sim 3000 \text{ W/cm}^2\text{K}$; sufficient for even the most demanding applications such as cooling X-ray emitting equipment [113]. Computational models of *CuO*-water nanofluids concur that nanofluids provide much higher thermal performances with no additional pressure drop [114]. Numerical models show that an addition of only 1% diamond nanoparticles in water pumped with 2.25 W can increase the cooling rate by $\approx 10\%$ [115].

The addition and increasing volume fraction of nanoparticles significantly increases the forced convective heat transfer of a fluid for both laminar [116, 117] and turbulent[118] flow. Studies found that the addition of 1.8% aluminium oxide (Al_2O_3) nanoparticles can enhance the convective heat transfer of water by 32%. In contrast, other experiments using a *CuO*-Water nanofluid have indicated that at high flow rates, the effect of the particle loading becomes negligible [119]. Investigations have also evaluated the effect between particle loading and natural convection [120]. The results show a decrease with increasing particle volume fraction.

Experiments have also incorporated nanofluids in heat pipes. A gold-water suspension has been shown to reduce the thermal resistance of the heat pipe by $\approx 40\%$ [121, 122]. Silver based nanoparticles decreased the thermal resistance by 10 – 80% at an input power of 30 – 60 W [123]. This significantly reduced the overall heat pipe temperature.

2.5 Conclusions

This chapter briefly describes possible considerations for thermal management. Heat sinks and heat pipes are established cooling devices already in industrial use as thermal management tools. The literature presents a large number of studies providing guidelines for improving their thermal efficiency. The review in this chapter has clarified that such devices need to be tailored to specific applications. Although a complicated task, which requires both numerical and experimental work, we believe that its academic potential is limited.

The review then changes direction into material sciences. Carbon allotropes and nanofluids are discussed. The thermodynamic properties of both have received considerable attention over the last years. However, they seem to lack the depth of understanding required by industrial standards. We believe that both offer the blend of academic and practical qualities required by this project.

It should be noted here that these topics are interconnected. First of all, heat sinks and heat pipes rely on materials with high thermal conductivities such as nanofluids and carbon allotropes. Indeed such studies have been mentioned in the preceding sections (e.g. nanofluids in microchannels and heatpipes, FLG on heat sinks) However, even the two materials can be related. The review has referred to studies in which carbon allotropes (e.g. CNT and diamond particles) have been used for nanofluids.

Following this review, the main focus of research was turned onto nanofluids. More specifically, we focused on how nanofluids behave under confinement; a realistic scenario which is considered by only a limited number of studies. However, we should mention that beyond a certain point, our investigations turned towards confined, pure liquids. This unplanned change was made following unexpected and fascinating results. Although the section on confined liquids precedes that on nanofluids (as it felt like a more natural order), it does not reflect the order in which the results were produced.

Molecular Modelling

Molecular modelling refers to a number of computational techniques, such as Molecular Dynamics (MD) and Monte Carlo (MC). These describe systems from an atomic/molecular perspective. Leaving quantum mechanics aside, molecular models can theoretically predict the behaviour of systems from first principles. This classical (rather than quantum) approach is in fact very accurate for many systems of interest.

However, as with any computational method, the model has to be set up correctly to accurately portray the physical system of interest. This chapter provides some general concepts for molecular modelling, as well as specific techniques used within this thesis. To enhance readability, we divided this chapter into three major sections:

1. *Geometrical structure*: This section explains crystallographic techniques for positioning atoms. This might seem irrelevant in a thesis on fluids as atoms do not have fixed positions. However, in modelling microchannel systems some crystallographic concepts are adopted during the design of the channel walls. We provide the basics for understanding the design of the models used in the results sections to follow. In addition, the main boundary conditions used in molecular methods are discussed.
2. *Molecular interactions*: This section deals with the interactions between atoms and molecules. We give a brief description of physical bonding mechanisms and intermolecular forces. We then explain the concept of potentials and how they can be used to model these interactions.
3. *Statistical Mechanics*: This section describes how statistical averages can translate the microscopic movements of atoms and molecules into meaningful, macroscopic and experimentally observable properties. This description gives rise to two main methods for molecular modelling: Molecular Dynamics (MD) and Monte Carlo (MC). Both these methods are briefly discussed.

3.1 Geometrical Structure

3.1.1 Crystallography

Crystals are solids whose atoms or molecules are arranged in a highly structured and organised manner. They are often categorized based on their invariance to changes in the coordinate system. This invariance is referred to as **symmetry**.

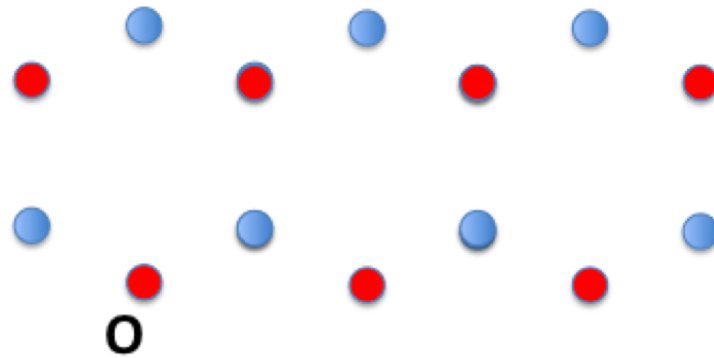
Crystallography is the science of unambiguously describing the structure of crystals. Given the positions of the crystal atoms, an arbitrary atom can be selected as the origin O . Due to the symmetric nature of the crystal, one can identify points which are identical to O . The set of such points makes up a **crystal lattice**, or simply **lattice**, and is a crucial part in the description of such materials. It is important to understand that the lattice points are positions of symmetry within the structure to which the atoms can be related; they do not necessarily correspond to atomic positions (i.e. they can be positions in between atoms).

Figure 3.1a shows the atomic structure of a crystal. The atoms are arranged in a honeycomb. This is in fact the structure of graphene (figure 2.6). We arbitrarily take the red atom labelled O as the origin and examine the relative positions of its immediate neighbours. In terms of these relative positions, all the red atoms are identical to O . Figure 3.1b isolates the **points** (not the actual atoms) in which these atoms lie. The isolated set of points forms a lattice. Atoms will later be related with each lattice point, fully describing the crystalline solid.

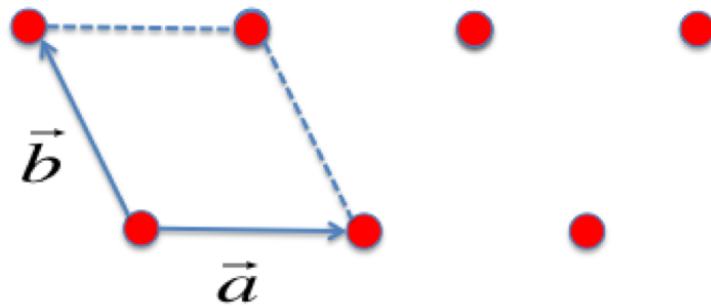
The choice of axis can be arbitrary (although some choice might be more convenient than others, as is generally the case in linear algebra). In this example the horizontal and vertical directions can be taken as the axis of choice. The distance and direction between the origin and the nearest lattice point along the axis are the **lattice vectors** \mathbf{a} and \mathbf{b} . The lattice vectors along with the angle γ between them ($\gamma = 120^\circ$ in figure 3.1b) can fully specify the lattice. Any point can be given by

$$\mathbf{r} = u\mathbf{a} + v\mathbf{b} \quad (3.1.1)$$

where u and v are positive integers. The generalization to three dimensions is trivial, requiring one further lattice vector and two more angles.



(a) Crystal Structure



(b) Crystal Structure

Figure 3.1: The atomic structure of a crystal solid (3.1a) with the atoms arranged hexagonally and a corresponding lattice (3.1b). The lattice is obtained by collecting all the points from the crystal structure which are identical to O in terms of the relative positions of their neighbours

Equation 3.1.1 also implies translational symmetry. Since it describes all the lattice points, and since all the lattice points are identical, then an observer moved from the origin of the crystal to a point dictated by the equation will notice no difference. Therefore, all crystals possess translational invariance. However some can also have various rotational symmetries. As an example the lattice presented in figure 3.1b is also invariant under a 60° rotation about an axis perpendicular to the plane. Depending on the types of symmetry that characterise a crystal, they can be categorised (for three-dimensional structures) into 14 lattices, called **Bravais** lattices. These are shown in table 3.1. For the purpose of this thesis, only the **face-centred cubic (fcc)** lattice and **body-centred cubic (bcc)** lattice are of interest. Therefore, only these will be discussed.

Within a lattice, shapes can be identified that when stacked together can produce the entire lattice. Such shapes are called **unit cells**. As the broken line in figure 3.1b shows, a unit cell can be produced by creating a parallelogram (in two-dimensions) or parallelepiped (in three-dimensions) using the lattice vectors. This is referred to as a **conventional unit**

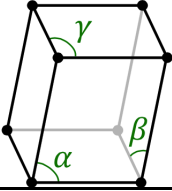
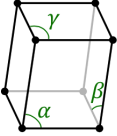
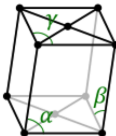
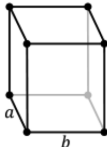
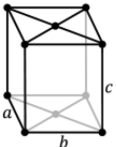
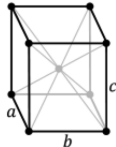
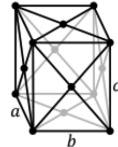
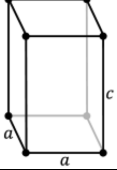
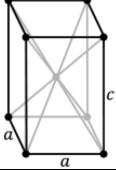
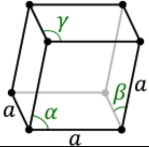
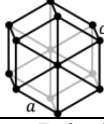
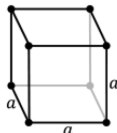
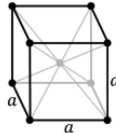
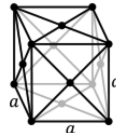
Lattice System	14 Bravais Lattices			
Triclinic	Primitive $\alpha, \beta, \gamma \neq 90^\circ$ 			
Monoclinic	Primitive $\beta \neq 90^\circ$ $\alpha, \gamma = 90^\circ$ 	Centred $\beta \neq 90^\circ$ $\alpha, \gamma = 90^\circ$ 		
Orthorhombic	Primitive $a \neq b \neq c$ 	Base-Centred $a \neq b \neq c$ 	Body-Centred $a \neq b \neq c$ 	Face-Centred $a \neq b \neq c$ 
Tetragonal	Primitive $a \neq c$ 	Body-Centred $a \neq c$ 		
Rhombohedral	Primitive $\alpha = \beta = \gamma \neq 90^\circ$ 			
Hexagonal	Primitive 			
Tetragonal	Primitive 	Body-Centred 	Face-Centred 	

Table 3.1: The 14 Bravais lattices divided into 7 lattice systems. Reproduced from the thread “Bravais Lattice” from Wikipedia

cell. The smallest possible unit cell is called a **primitive unit cell** and does not necessarily coincide with the conventional one. An important universal primitive unit cell is the polyhedron obtained by drawing the perpendicular bisectors of the lines joining a lattice point to its neighbours. This area is a locus of all the positions closer to this lattice point than any other. This primitive unit cell is known as the **Wigner-Seitz cell**.

Once the lattice is established, we need to map atoms onto it to define the crystal structure. A set of atoms, called the **basis**, is associated with the origin. Each atom in the basis is related to the origin through the vector

$$\mathbf{r} = x\mathbf{a} + y\mathbf{b}$$

where \mathbf{r} is a position vector; x and y are real numbers; and \mathbf{a} and \mathbf{b} are lattice vectors. Therefore, for each atom in the basis, a set of 2 numbers can describe its position relative to the origin. These are then copied across all lattice points to form the crystal structure. Taking figure 3.1a and 3.1b as an example, two atoms can be mapped on each lattice point. The red atoms coincide with the lattice and therefore $x = 0$ and $y = 0$. For graphene the blue atoms can be mapped onto the lattice points through the vector $\mathbf{r} = \frac{2}{3}\mathbf{a} + \frac{1}{3}\mathbf{b}$. The basis can now be written as

$$C(0, 0), C\left(\frac{2}{3}, \frac{1}{3}\right)$$

where the letter C indicates the chemical symbol of the atom in that position (in this case C for carbon). Again, extrapolating to three dimensions is trivial.

Within a crystal lattice, one can identify parallel planes (or lines in two dimensions) equally spaced between them. A set of such planes can be identified using the **Miller indices** (hkl) which show that the plane closest to the origin (excluding planes that pass through it) intersects the axes at $\frac{a}{h}, \frac{b}{k}, \frac{c}{l}$, where a, b and c are the lengths of the unit vectors. By convention, negative index values are indicated by a bar, $(\bar{h}\bar{k}\bar{l})$. Every plane in a set has the same density. Furthermore, the set of all planes must contain all the lattice points. Figure 3.2 shows two examples of commonly used lattice planes: the (100) plane (figure 3.2a) and the (111) plane (figure 3.2b)

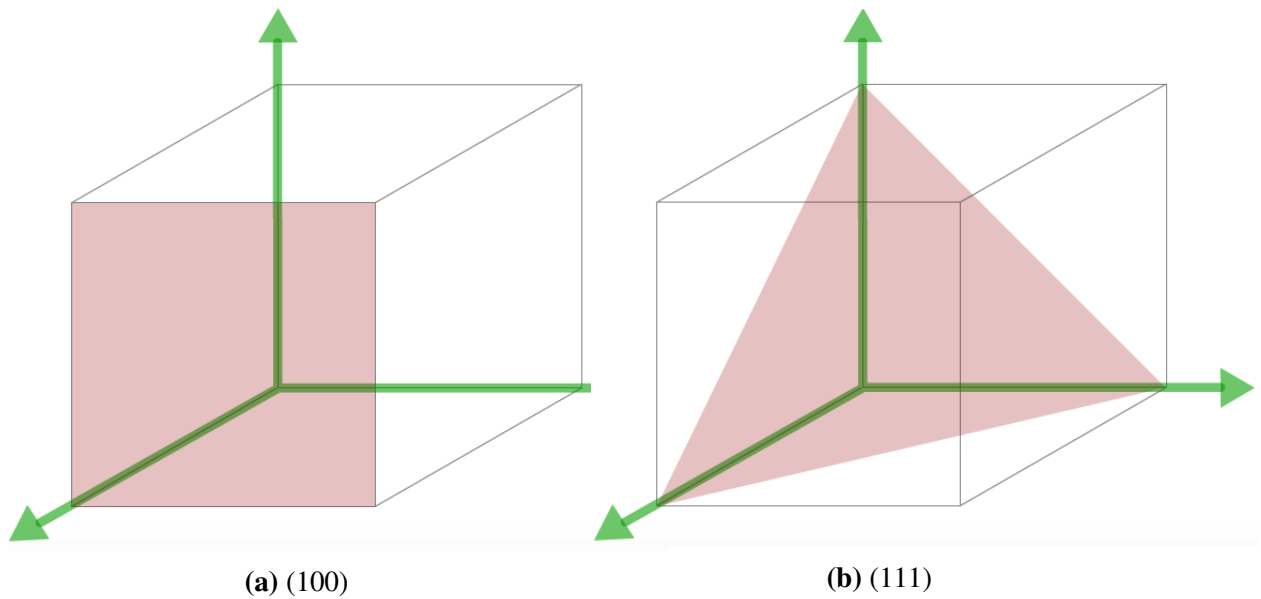


Figure 3.2: Two lattice planes (shaded) within a unit cell of a cubic lattice

The *fcc* lattice shown in table 3.1 is important for modelling solids. As shown more clearly in figure 3.3a, the conventional unit cell has lattice points on the corners of a cube, as well as on the centres of its faces. It is worth noting here, that the conventional unit cell is not primitive. The primitive unit cell is the rhombohedral unit cell illustrated in figure 3.3b. Generally, the conventional unit cell is used as it illustrates the symmetrical features of the lattice more clearly.

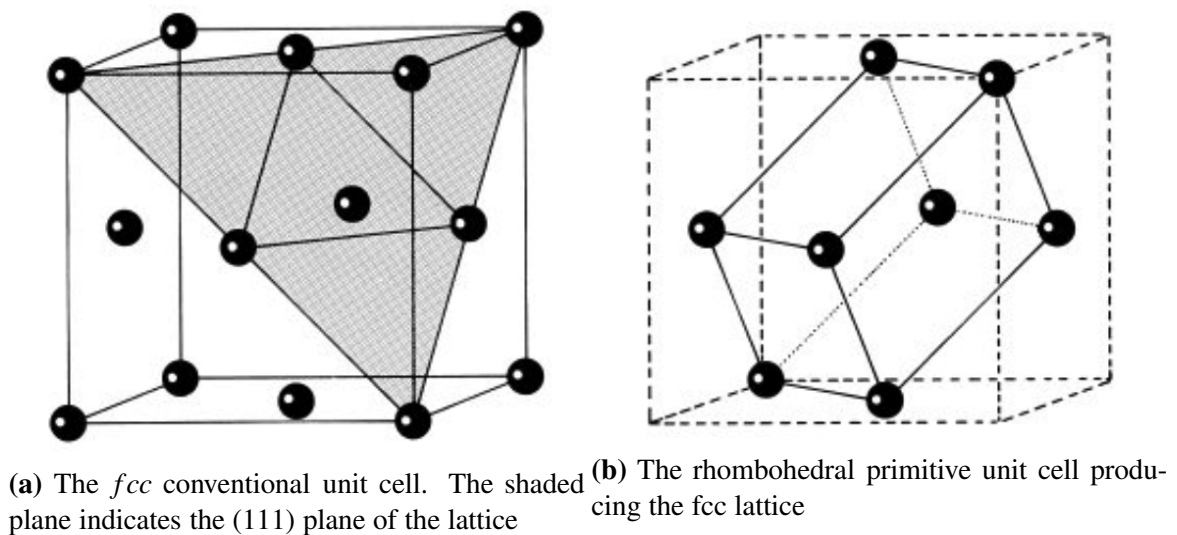


Figure 3.3: Conventional and primitive cell of *fcc* lattice. Reproduced from [13]

The *fcc* lattice is also called **cubic-closed pack**. The reason is that its (111) lattice planes (the shaded plane in figure 3.3a) form dense arrangements of atoms called **closed-**

packed layers. The planes are staggered, such that each layer overlaps with the gaps of the previous one (figure 3.4). This is ideal for modelling various solids such as ionic solids where the electrostatic Coulombic forces tend to pull the atoms closer together.

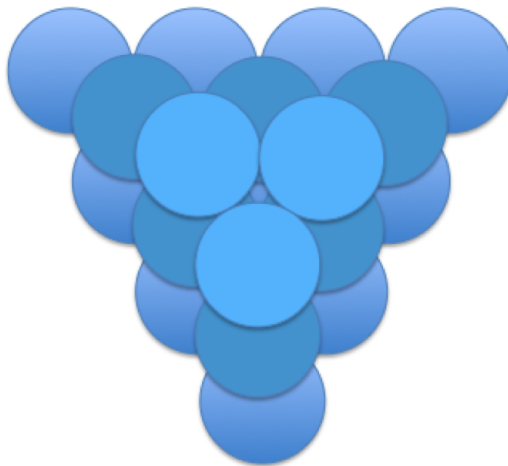


Figure 3.4: A close-packing of spheres arranged in an fcc structure

The *bcc* lattice from the cubic lattice system (table 3.1) is ideal for slightly less close-packed structures. Metallic elements such as lithium, sodium and potassium can be modelled using the *bcc* lattice. The conventional unit cell (which again is not a primitive unit cell) has four lattice points on the corners of the cube, as well as one in its centre.

3.1.2 Boundary Conditions

The computational complexity of molecular modelling techniques sets an upper limit to the system size that we can practically simulate. Usually, only a small sample of the system in question is modelled. This is done by defining a box, called a **simulation box** (or **simulation cell**) in which a set of representative atoms are placed and the system dynamics defined.

An important factor in the design of a molecular model is the behaviour of the atoms and molecules at the boundaries of this box. A simple approach is to use a **fixed** boundary condition in which the simulation cell is surrounded by void space. Although this might occasionally be a desired layout, it can have the following drawbacks:

- Atoms can leave the simulation cell. This is particularly common in fluids where the interactions are not strong enough to keep the atoms tethered to their positions. The atoms will continue their trajectory getting further away from the rest of the system. This will interfere with the calculation of properties. Additionally, the in-

creasing distance between the strayed atom and the simulation cell will often cause the simulation to halt.

- Atoms at the boundary do not generally experience the same forces as those at the centre of the system. If one considers a homogeneous solid, the atoms at the centre of the simulation cell will feel the influence of all atoms around them. At the boundary, the atoms will only be influenced from one direction. Due to the small dimensions of the simulation box, this behaviour will not accurately depict the bulk behaviour of the system.

An alternative way to treat the edges of the simulation box is to use **periodic** boundary conditions. One can think of this as stacking an infinite number of boxes identical to the simulation cell in one or more dimensions. This can be shown in figure 3.5. Of course, since computational efficiency is of paramount importance (and the reason for having this discussion) the simulation only considers the simulation cell. The periodic boundary conditions are emulated by applying the following rules:

- An atom passing through the boundaries of a simulation cell, re-enters it from the opposite boundary rather than completely departing from the system (as with fixed boundary conditions).
- The potential of an atom wraps around the simulation box. This means that an atom close to a boundary can influence the atoms in the opposite side of the box through the boundaries. This assumes the interatomic distance is within the prescribed radius of influence (as discussed later in this chapter).

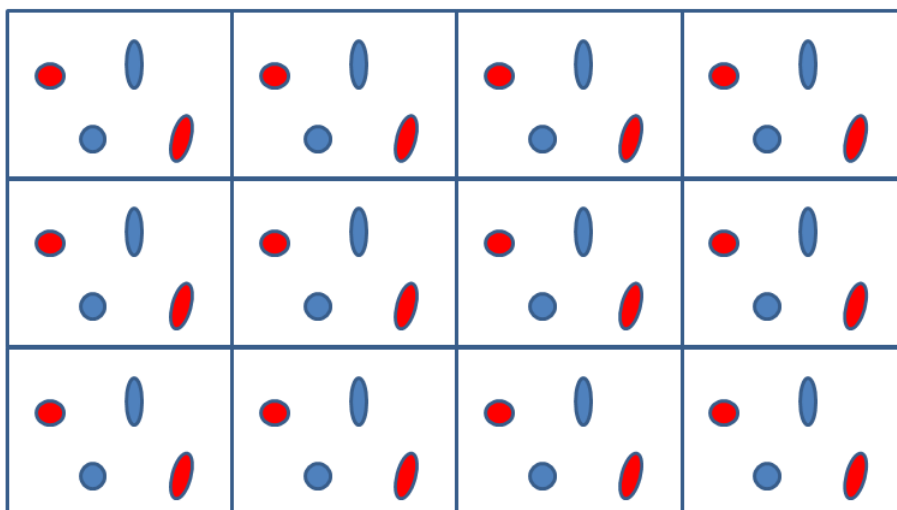


Figure 3.5: An illustration of periodic boundary conditions in two dimensions. The simulation cell is infinitely stacked in the two dimensions such that all atoms interact in a similar manner

3.2 Dynamics

3.2.1 Intramolecular Forces

Intramolecular forces refer to the strong interactions between atoms. These are responsible for the formation of molecules. From a fundamental point of view, these forces are a product of electrostatic interactions between the positively charged nucleus and negatively charged electrons that make up atoms. There is no distinction between such interactions. All intramolecular forces can be calculated by solving Schrödinger's equation. However, in order to conceptualize and simplify these interactions, they have been divided into three main categories:

- Ionic bonds
- Covalent bonds
- Metallic bonds

The following sections briefly explain these concepts. To assist in the clarity of the sections on chemical bonds, a brief section on the electronic configuration and behaviour of atoms is included first. It must be noted that in the following section electrons are depicted (and will often be referred to) as having definite positions and velocities. This description is far from accurate. In quantum mechanics, an electron can be thought of as a smear occupying a region in space. An amplitude in each position indicates the probability of finding the electron there. Here, the classical approach is considered to be sufficient for the purposes of this thesis. When required, reference to the quantum mechanical behaviour of particles will be made.

Electronic Configuration and Behaviour of Atoms

Atoms are the smallest component that can characterize a material, or more precisely a **chemical element**. They are made up of a positively charged nucleus (positive protons and neutral neutrons) surrounded by negatively charged electrons.

Figure 3.6 shows the **periodic table**. It intuitively arranges all the elements in a table that provides information on their number of protons and electronic structure. Each element is defined by its number of protons, called the **atomic number**. In the periodic table, this is presented as the integer over each element. We will now talk about electron configurations. In the following discussions, all individual atoms are considered to be neutral (i.e. the number of electrons is the same as the atomic number).

Group →	1	2	3	4	5	6	7	8	9	10	11	12	13	14	15	16	17	18	
↓Period																			
1	1 H																		2 He
2	3 Li	4 Be											5 B	6 C	7 N	8 O	9 F	10 Ne	
3	11 Na	12 Mg											13 Al	14 Si	15 P	16 S	17 Cl	18 Ar	
4	19 K	20 Ca	21 Sc	22 Ti	23 V	24 Cr	25 Mn	26 Fe	27 Co	28 Ni	29 Cu	30 Zn	31 Ga	32 Ge	33 As	34 Se	35 Br	36 Kr	
5	37 Rb	38 Sr	39 Y	40 Zr	41 Nb	42 Mo	43 Tc	44 Ru	45 Rh	46 Pd	47 Ag	48 Cd	49 In	50 Sn	51 Sb	52 Te	53 I	54 Xe	
6	55 Cs	56 Ba	*	72 Hf	73 Ta	74 W	75 Re	76 Os	77 Ir	78 Pt	79 Au	80 Hg	81 Tl	82 Pb	83 Bi	84 Po	85 At	86 Rn	
7	87 Fr	88 Ra	**	104 Rf	105 Db	106 Sg	107 Bh	108 Hs	109 Mt	110 Ds	111 Rg	112 Cn	113 Uut	114 Fl	115 Uup	116 Lv	117 Uus	118 Uuo	
		*	57 La	58 Ce	59 Pr	60 Nd	61 Pm	62 Sm	63 Eu	64 Gd	65 Tb	66 Dy	67 Ho	68 Er	69 Tm	70 Yb	71 Lu		
		**	89 Ac	90 Th	91 Pa	92 U	93 Np	94 Pu	95 Am	96 Cm	97 Bk	98 Cf	99 Es	100 Fm	101 Md	102 No	103 Lr		

Figure 3.6: Periodic table depicting all the known elements found in nature. Reproduced from Wikipedia under "Periodic Table" thread)

Electrons surrounding the atom are divided into **electron shells**. These are regions around the atom in which the electrons are most likely to be found. The shells are labelled as integer numbers. The higher the number the further away this region is from the nucleus. Each shell can hold up to a fixed number of electrons. Furthermore, each shell, starting from the first one close to the nucleus, must be entirely filled before electrons start occupying the next one (there are some exceptions to this rule at higher electron shells).

The row number in the periodic table, often referred to as the **period**, indicates the number of shells available for occupation for the elements in that row. It also defines the **valence shell**, the outermost shell of the atom. The electrons with the highest energies (which are often **but not always** occupying the valence shell) are called **valence electrons**. These are responsible for chemical reactions and the formation of bonds.

The columns of the periodic table are called **groups**. They indicate the number of electrons filling the valence shell. Each atom favours a filled valence shell as this results in a lower energy state. The tendency to fully occupy the outermost shell is called the **octet rule** since, for all but the first shell, a valence shell can hold up to eight electrons. To elaborate, consider an atom with only one electron in its outermost shell. This will be biased towards losing the electron and dropping to a lower but completely filled valence shell. On the contrary, an atom with seven electrons in its valence shell (i.e one missing to fill it entirely) will have the disposition to obtain an extra electron. The octet rule (which is a rule of thumb and not an accurate description) is responsible for molecular bonding, as well as the type of bonds between atoms.

Since the groups of the periodic table indicate how the various shells are filled, elements of the same group tend to have similar characteristics. Although discussing each group in detail would in this case be an extravagance, three groups are worth mentioning. The

elements of the last group (column 18) are referred to as **noble gases** and have their valence shell entirely filled. In turn, this makes this group the most stable and least reactive (i.e. such elements don't want to lose or gain electrons). In fact, the octet rule can be rephrased as the tendency of atoms to reach the electronic configuration of the nearest noble gas. The elements in the first group are called **alkaline metals**. These have only one valence electron and are eager to lose it in order to get to the configuration of the previous noble gas. The elements in the penultimate group before the noble gases are called **halogens** and require an additional electron to complete their valence band.

The tendency of an atom to attract electrons is called **electron affinity**. More specifically it is the energy released (lowered) when an additional electron is added. Hence, as the group number approaches that of the noble gases, the electron affinity increases (i.e. alkaline metals have low electron affinity while halogens have high).

Ionic Bonding

Ionic bonding is the attraction between negatively and positively charged atoms, known as anions and cations respectively. It often occurs between pairs of elements with a large electron affinity difference. If two atoms have neutral charge, the atom with high electron affinity will capture electrons from the atom with low electron affinity. This in turn will ionize the former into an anion and the latter into a cation. Following this ionization, the two atoms will be attracted to each other and bonded through Coulomb's forces.

The most common example of ionic bonding is between a sodium (Na) and a chloride (Cl) atom. Sodium belongs in the group of alkaline metals which, as discussed in the previous section, has low electron affinity. Chloride on the other hand, belongs to the halogen group which has very high electron affinity. An electron is transferred from the sodium atom to the chloride atom. This is followed by an electrostatic attraction that forms sodium chloride (NaCl).

In molecular models, such bonds can be formed by assigning corresponding positive and negative charges to the atoms. A Coulombic potential can be used to calculate the appropriate force between them (section 3.2.3)

Covalent Bonding

When the electron affinity of two atoms is comparable and relatively high, both atoms require more electrons in order to get to the more stable electronic configuration of noble gases. A transfer of an electron (such as in ionization bonding) will benefit one atom at the expense of another. Instead they come closer together so as to share one or more of each other's electrons. This bonding due to the sharing of electrons is called **covalent bonding**.

An example of covalent bonding can be found in water molecules. In its neutral state, a hydrogen atom has one electron. It requires an additional electron to fill its valence band (the exception to the octet rule) and reach the more stable electronic configuration of helium (a noble gas). An oxygen atom has six electrons in its valence shell. Therefore, it requires two more electrons to reach the electronic configuration of neon Ne. The mutual tendency of both oxygen and hydrogen to acquire more electrons is satisfied by forming the water molecule. Each hydrogen atom shares one of the oxygen's electrons while the oxygen atom shares an electron from each of the two hydrogen atoms. Figure 3.7 depicts a water molecule and shows how the electrons of the hydrogen atoms are shared with those of the oxygen atom through covalent bonds.

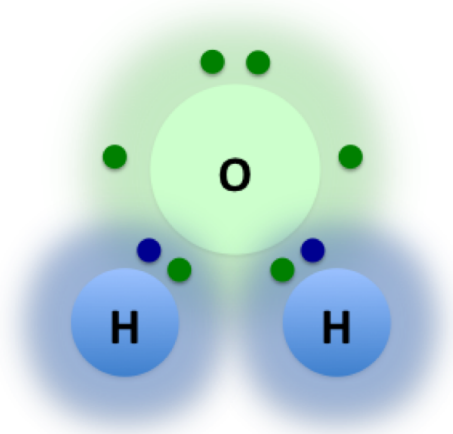


Figure 3.7: A schematic representation of a covalent bond within a water molecule between an oxygen (light green) and two hydrogen atoms (light blue). The smaller circles represent electrons with the dark blue electrons being the ones initially possessed by the hydrogen atoms and the dark green electrons being the ones initially possessed by the oxygen atom

For reasons of clarity, the figure inaccurately shows the electrons as having fixed positions and being shared equally among the two atoms. In reality, electrons spend more time closer to the oxygen atom rather than the hydrogen atoms. From a quantum mechanical viewpoint, there is significantly higher probability to find the electrons closer to the oxygen atom. The extent to which an atom within a bond attracts electrons more than the other bonded parties is called **electronegativity**. It is directly correlated with the difference in electron affinity of the atoms forming the molecule.

As a result of the different electronegativities of hydrogen and oxygen atoms, a water molecule is said to be **polar**. This means that, although the molecule as a whole is neutral, the charge is not distributed evenly across the molecule. Therefore, the region close to the oxygen atom is more negative than those close to the hydrogen atoms. This shows that ionic bonding is in fact an extreme case of covalent bonding. As mentioned earlier, from a fundamental point of view, all interactions are the same and the categorization is merely a

figure used for simplification.

Finally, covalent bonds are said to be directional. The bonded atoms are placed at angles relative to each other such that a lower energy state is achieved. The **bond angle** is an important property of molecules and is always considered while modelling them. The distance between the atoms of a bond is called the **bond length** and is also important in molecular modelling. Such aspects are considered later in this chapter (section 3.2.3)

Metallic Bonding

Metals have electrons which are not tightly bound to an atom or a covalent bond. Instead these **delocalised** electrons are shared among an atomic lattice. The electrons are often thought of as a fluid of negative charge flowing over the positively charged nuclei of the metal atoms. The electron gas flowing between metal atoms is schematically shown in figure 3.8. **Metallic bonding** refers to the strong electrostatic attraction between the positively charged nuclei and the negatively charged fluid of electrons and is what keeps metals together. This flexibility of electrons to move across the atomic lattice is what gives metals their flexibility.

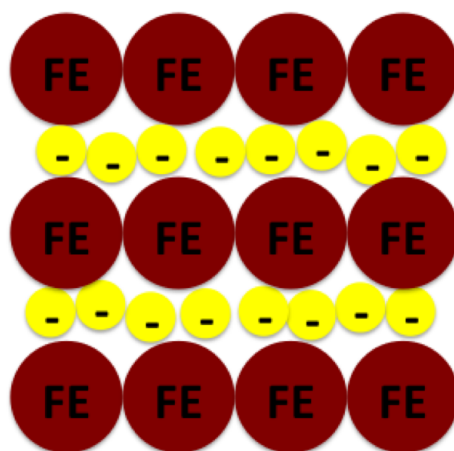


Figure 3.8: A schematic representation of a metallic bond between iron atoms (FE). The negatively charged electrons (yellow with minus sign) move freely across the lattice. The positively charged iron atoms are attracted to this electron fluid through electrostatic forces

3.2.2 Intermolecular/interatomic Forces

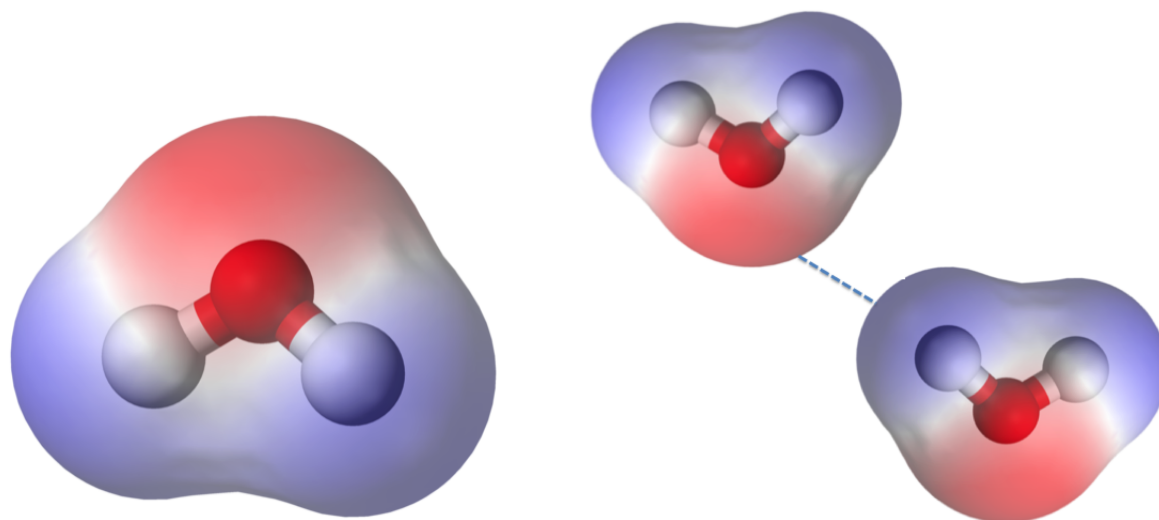
Molecules and non-reactive atoms (such as noble gases), exert forces on each other that depend on their relative distance. When the forces act between molecules they are referred to as **intermolecular**. **Interatomic** refers to the interactions between non-reactive atoms. The distance between two molecules or atoms is called **intermolecular** and **interatomic**

distance respectively. The weak nature of these forces is what distinguishes intermolecular from the intramolecular forces (chemical bonds).

Intermolecular forces contain both attractive and repulsive components. In this section, we do not include interactions between ions. We consider all molecules to be neutral. We also refer to the collection of attractive and repulsive forces that will be described as **van der Waals** forces (some texts might use different definitions).

The repulsive component of the van der Waals forces, is triggered at very short intermolecular distances. It is a product of the **Pauli exclusion principle**: a fundamental quantum mechanical concept which prevents fermions, such as electrons, from occupying the same quantum state. As the electronic shells of molecules (or non-reacting atoms) come close together, strong repulsive forces are exerted to prevent electrons from colliding and violating the Pauli exclusion principle.

The origin of the attractive forces is sometimes confusing since the molecules are considered neutral. However regions within a neutral molecule can be charged. This is a result of different electronegativities between the atoms (as explained in section 3.2.1). Such molecules are called **multipoles**. Figure 3.9a shows the negative (red shade) and positive (blue shade) regions of a water molecule. Since there are only two regions, this is called a dipole.



(a) Schematic of a water molecule. The shaded area over the atoms indicates the charge, with the blue shade indicating positive charge while the red indicates negative charge. Reproduced from Wikipedia under the thread "Chemical Polarity")

(b) Schematic of a dipole-dipole interaction between two water molecules.

Figure 3.9: Schematic representation of the polarity of water molecules (3.9a) and the dipole-dipole interactions between them (3.9b)

Therefore, electrostatic, attractive forces are exerted between oppositely charged re-

gions of different **multipole** molecules. The attraction between permanent dipoles is called **dipole-dipole** attraction. Figure 3.9b depicts such an interaction between two water molecules. It is worth noting that in the case where hydrogen is bonded with highly electronegative atoms such as oxygen, the induced dipole-dipole attraction is significantly stronger and is often called a **hydrogen bond**. This strong interaction is what gives water its high surface tension.

Based on the explanation given so far, only multipole molecules can have attractive forces between them. The problem is that we tend to visualise atoms and molecules as rigid objects with electrons having fixed positions around them. The reality is that they are highly dynamic systems with electrons moving around continuously. It is therefore the case that a non-polar molecule can momentarily have the majority of its electrons localized on one side and temporarily become a dipole. The molecule is in this case called an **induced dipole**. Attractive forces between induced dipoles are called **London dispersion forces**. Due to the statistical nature of this phenomenon, attractive forces between induced dipoles are significantly weaker than dipole-dipole attraction. London dispersion forces can occur between non-reactive elements/atoms such as the noble gases (e.g. argon, neon). The majority of the simulations of this study use liquid argon. As a noble gas, its atoms interact mostly through London dispersion forces which can be modelled using the Lennard-Jones potential (section 3.2.3)

To summarise, van der Waals forces consist of

1. Repulsive force due to Pauli exclusion principle
2. Attractive force between permanent dipoles
3. Attractive force between a permanent dipole and an induced dipole
4. Attractive force between two induced dipoles

3.2.3 Interatomic Potentials

Interatomic Potentials are mathematical functions of the atomic positions that describe the potential energy of the system. They therefore dictate how the particles interact. Correctly setting the potentials of the system is extremely important in modelling its dynamic behaviour. The total potential energy is given by:

$$\mathcal{V} = \sum_i \mathcal{V}_1(\mathbf{r}_i) + \sum_i \sum_{j>i} \mathcal{V}_2(\mathbf{r}_i, \mathbf{r}_j) + \sum_i \sum_{j>i} \sum_{k>j} \mathcal{V}_3(\mathbf{r}_i, \mathbf{r}_j, \mathbf{r}_k) + \text{higher terms} \quad (3.2.1)$$

where i and j are two arbitrary atoms; \mathbf{r}_i is the position of the atom i ; \mathcal{V} is the total potential energy; \mathcal{V}_1 is the potential of individual atoms; \mathcal{V}_2 is the potential between pairs

of atoms; \mathcal{V}_3 is the potential between triplets etc. The first term (\mathcal{V}_1) is the potential energy of an atom due to an external field. It has no relation to the positions of any other atoms in the system. This term vanishes in the absence of such a field. The second term (\mathcal{V}_2) is the pairwise potential. It describes the influence that two atoms have on each other, based on their interatomic distance r_{ij} . The third term (\mathcal{V}_3) is between three atoms. It is required when a third atom can alter the pairwise interactions (i.e. the total potential is not simply an addition of the pairwise potentials). Although this term is significant in describing the behaviour of liquids, it is rarely included in computer simulations because it adds a large computational overhead. Instead, **effective pairwise potentials** can be used which incorporate many-body effects. These are usually obtained through regression analysis of experimental data and can realistically describe the behaviour of liquids [124].

Once the potential is defined, the force acting on an atom is given by:

$$\mathbf{F}_i = -\nabla_{\mathbf{r}_i} \mathcal{V} \quad (3.2.2)$$

where i is an arbitrary atom; \mathbf{F} is the force acting on an atom i ; and $\nabla_{\mathbf{r}_i} \mathcal{V}$ is the gradient of the potential as a function of space.

An important pair potential, and the one mostly used for the simulations of this investigation, is the Lennard-Jones (LJ) 12 – 6 potential:

$$\mathcal{V}^{LJ} = 4\varepsilon \left[\left(\frac{\sigma}{r} \right)^{12} - \left(\frac{\sigma}{r} \right)^6 \right] \quad (3.2.3)$$

which has been empirically designed to match experimental results of argon. Figure 3.10 plots the LJ potential, \mathcal{V}^{LJ} as a function of the interatomic distance r . The parameter σ indicates where the curve cuts the axis. It is often called the **molecular distance**. For argon $\sigma \approx 0.3405nm$. The parameter ε is the depth of the potential well. The greater its value, the greater the strength of the interaction. For argon $\varepsilon \approx 1.65678 \times 10^{-21} J$.

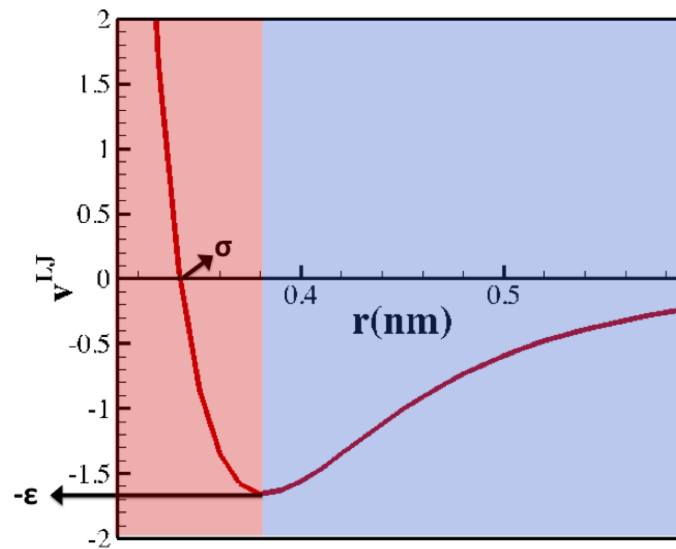


Figure 3.10: Lennard-Jones potential as a function of the interatomic distance. The function crosses the axis at a distance σ and reaches a minimum at $-\epsilon$. At short distances (shaded as red) the interatomic forces are repulsive due to the Pauli exclusion principle while at larger distances (shaded in blue), van der Waals forces are attracting the atoms

The $\left(\frac{\sigma}{r}\right)^{12}$ term (shaded as red in figure 3.10) models the interactions over very short interatomic distances. According to equation 3.2.2, the steep, negative gradient of the potential in this region results in very strong repulsive forces. These correspond to the Pauli exclusion principle which prevents collisions between electrons (section 3.2.2). The weaker, attractive van der Waals forces at larger distances (shaded as blue in figure 3.10) describe the London dispersion forces which dominate the attractive component of the interaction of noble gases (section 3.2.2).

Although the LJ potential is tailored for interactions between argon atoms, an adjustment of the parameters ϵ and σ can adapt the function for other elements. The parameters for some common materials can be found in table 3.2

Element	ε	$\sigma(nm)$
Hydrogen (H)	1.187×10^{-22}	0.281
Helium (He)	1.408×10^{-22}	0.228
Carbon (C)	7.069×10^{-22}	0.335
Nitrogen (N)	5.15×10^{-22}	0.331
Oxygen (O)	8.505×10^{-22}	0.295
Fluorine (F)	7.29×10^{-22}	0.283
Neon (Ne)	6.49×10^{-22}	0.272
Sulphur (S)	2.527×10^{-21}	0.352
Chloride (Cl)	2.3954×10^{-21}	0.335
Argon (Ar)	1.654×10^{-21}	0.341
Bromine (Br)	3.9652×10^{-21}	0.354
Krypton (Kr)	2.2643×10^{-21}	0.383

Table 3.2: Table with LJ parameters for pairwise interactions between atoms of the same element. These values are merely empirical and might vary significantly depending on the type of bonding between them

The parameters in the table describe pairwise interactions in which both atoms are of the same type. However, we often need to define interactions between unlike elements. If the LJ parameters of the individual elements are known then **mixing rules** can be used to empirically calculate the parameters for the interaction between the two different atoms. A frequently used such rule is the Lorentz-Berthelot mixing rule. Denoting the two elements by 1 and 2, it gives the in-between LJ parameters by

$$\varepsilon_{12} = \sqrt{\varepsilon_{11}\varepsilon_{22}} \quad (3.2.4)$$

and

$$\sigma_{12} = \frac{1}{2}(\sigma_{11} + \sigma_{22}) \quad (3.2.5)$$

It should be mentioned that LJ parameters (both the ones from table 3.2 and the ones obtained from equations 3.2.4 and 3.2.5) are only empirical approximations and should be treated with care as they can sometimes produce inaccurate results (for example the strong covalent bonds between carbon atoms in graphene cannot be modelled with LJ potentials).

When dealing with ions, the LJ potential needs to be complemented with a term accounting for electrostatic, Coulombic forces. This term is given by:

$$\mathcal{V}^{electrostatic}(r_{ij}) = \frac{q_i q_j}{4\pi\varepsilon_0 r_{ij}} \quad (3.2.6)$$

where q is the charge of the atoms i and j ; and ε_0 is the permittivity of free space, a characteristic of a medium describing how difficult it is to create an electric field within it.

In many cases, we require atoms to be located onto or near specific locations. We can model this by assigning spring potentials on an atom, such that when it moves away from an equilibrium position, a restoring force is applied to push it back. Hooke's law calculates this force by:

$$F = -KX \quad (3.2.7)$$

where K is the stiffness characterising the spring and X is the distance away from the equilibrium position. The larger the value of K the harder it is to move the atom far away from its equilibrium position. This technique is useful in many situations. For microfluidics, it is often employed to ensure that the channel walls keep their crystal structure while at the same time, vibrate in a manner analogous to solids.

So far we have only discussed the weak interatomic forces. Theoretically, modelling intramolecular and intermolecular interactions should be treated in a similar manner. By setting the correct potentials, strong forces should naturally bond atoms together forming molecules which then interact. However, the quantum mechanical nature of chemical bonds complicates this task significantly. There is no general way of treating chemical bonds. Instead, systems are treated based on the specific application.

For interaction between metallic systems, the **Embedded Atom Method (EAM)** is commonly used. Metallic atoms are kept together by the attractive forces between their positive nuclei and the delocalised electrons (electron fluid) which "flow" freely between them (section 3.2.1). The EAM potential models this by including, in addition to the pairwise component, a term accounting for the electron density which is also a function of pairwise distances. The pairwise component and electron density do not usually have an analytical description. Instead they are described by large files containing their values at different pairwise distances.

Covalently bonded molecules are often modelled as unbreakable entities with fixed atomic bonds. The molecular bonds are defined before the simulation runtime and have predetermined lengths, angles and torsion angles to emulate the directionality of covalent bonds (section 3.2.1). The bonds can be rigid or can allow some flexibility for atoms to vibrate.

The interaction between molecules is achieved by defining a set of sites on each molecule. These often, but not always [125], correspond to the atomic positions within the molecule. However, they can also be placed in arbitrary positions within a small volume enclosing the molecule. The sites within the same molecule do not interact among themselves since the bonds are already fixed. However, sites of different molecules interact using potentials. Any available interatomic potentials can be used for such interactions (e.g. LJ potential). In some models, the potential between sites can be adjusted based on the orientation of the two molecules [126]. The intermolecular force between two molecules is the sum of the individual forces exerted between all pairs of sites (across the two molecules).

The general conclusion of this section is that considerable research needs to be car-

ried out before modelling any system. The literature presents a huge number of different approaches, each tailored to specific applications. Even for the same system, there are usually a number of different models available. These might be appropriate under different conditions. They might also have varying degrees of accuracy and the choice is simply a matter of the available computational resources.

Attempting to discuss even a modest percentage of these methods is beyond the scope of this thesis. However, the next section briefly describes some common ways to simulate water. This should help put some of the information described here in context. Furthermore, part of our studies use water. An explanation of the various modelling techniques available is therefore important.

Water Model

The water molecule consists of two hydrogen atoms covalently bonded with an oxygen atom. Even though the total charge is neutral (i.e. equal number of electrons and protons in the molecules), electrons tend to spend more time close to the oxygen atom. This gives the region close to it a negative charge while the region close to the hydrogens have a positive charge (section 3.2.1). We will now briefly describe how the molecule can be modelled computationally.

For the purposes of MD or MC, the bonds of the water molecules are usually fixed. By this we mean that they are predetermined and cannot be broken during the simulation. Each bond can be described by its length. The length of the HO bond is $\approx 0.9584\text{\AA}$. The angle between the two bonds is $\approx 104.48^\circ$. However, different models (such as the SPC discussed below) might use slightly different parameters based on the tetrahedral molecular geometry.

Once the bonds are fixed, the next step is to define how water molecules interact. A number of models are available in the literature. They are often categorised based on the number of charges used. Remember, these can be placed at arbitrary points across the molecule and do not necessarily correspond to atomic positions.

3-site models refer to those in which the charges coincide with the three atoms of the water molecule. Each hydrogen atom is assigned a positive charge. The oxygen atom is assigned a negative charge. All atoms between different water molecules interact electrostatically via Coulombic forces (dictated by the potential of equation 3.2.6). An LJ component (equation 3.2.3) is also added. This is usually only for the interaction of oxygen atoms. Therefore, the intermolecular potential describing interactions between water molecules is given by:

$$\mathcal{V}^{inter} = \sum_{i \neq j} \left\{ 4\epsilon_{ij} \left[\left(\frac{\sigma_{ij}}{r_{ij}} \right)^{12} - \left(\frac{\sigma_{ij}}{r_{ij}} \right)^6 \right] + \frac{q_i q_j}{r_{ij}} \right\} \quad (3.2.8)$$

The 4-site models can be obtained by moving the negative charge slightly towards the hydrogen atoms along the bisector of the angle formed by the bonds. This is an example of an artificial site (does not coincide with an atom) added to provide a more accurate approximation to the polar nature of the molecule. In these models there are three charged sites, interacting through Coulombic forces, as well as one on the oxygen atom which interacts via LJ potentials. The most commonly used 4-site model is the **TIP4P** model [127].

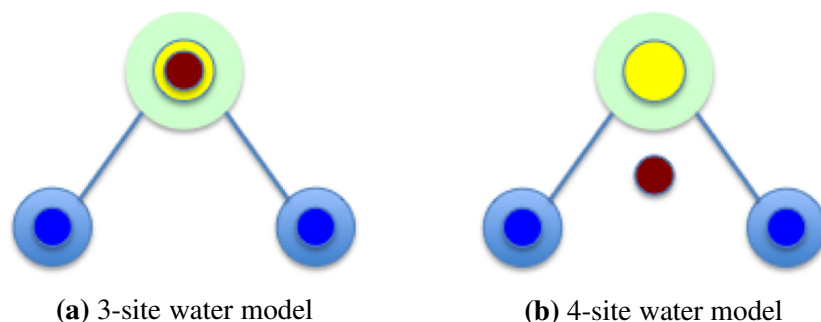


Figure 3.11: Illustration of 3-site model 3.11a and 4-site model 3.11b site models for water. The dark blue circles indicate positive charges, the red circle indicates the negative charge and the yellow circle is where the LJ potential is acting. The 3-site model has its charges on the same positions as the atoms. The 4-site model shifts the negative charge toward the hydrogens along the bisector of the angle

Although the **TIP4P** model is more accurate than 3-site models it is computationally more expensive. Furthermore, under normal conditions and temperatures, 3-site can also be very accurate [14]. For the remainder of this section we will mostly deal with 3-site models.

There are a number of 3-site models. These differ in the values of the charges, the Lennard-Jones parameters, the bond length, and the bond angle. The most common ones are the Transferable Intermolecular Potential Functions (TIPS) [128], Single Point Charge (SPC) [129], and the Transferable Intermolecular Potential 3 Point (TIP3P) [127] methods. Various extensions of these three models, such as the extended SPC (SPC/E) [130], are also available. The extensions aim to model the polarity of water, and describe its behaviour in a wide range of conditions as accurately as possible. In addition, some methods allow for some flexibility within the molecule. Intermolecular degrees of freedom are modelled by allowing the bond lengths and angles to vibrate using spring potentials. The equation describing such intramolecular interactions is

$$\mathcal{V}^{intra} = \frac{K_{len}}{2} \left[(r_{OH_1} - r_{OH}^0)^2 + (r_{OH_2} - r_{OH}^0)^2 \right] + \frac{K_{ang}}{2} (\theta_{HOH} - \theta_{HOH}^0)^2 \quad (3.2.9)$$

where K_{len} and K_{ang} is the spring stiffness of the length and angle, r_{OH_1} and r_{OH_2} are the lengths of the two bonds; r_{OH}^0 the the equilibrium bond length; θ_{HOH} is the bond angle; and θ_{HOH}^0 is the equilibrium bond angle. The intramolecular interactions of the rigid models

Model	SPC [129]	SPC/E [130]	TIP3P [127]	SPC/Fd [131]	F3C [130]	TIP3P/Fs [132]	SPC/Fw [14]
K_{len} ($kcal\ mol^{-1}\ \text{\AA}^{-2}$)	∞	∞	∞	1054.20	250	1059.162	1059.162
r_{OH}^0 (\AA)	1.0	1.0	0.9527	1.0	1.0	0.96	1.012
K_{ang} ($kcal\ mol^{-1}\ rad^{-2}$)	∞	∞	∞	75.90	60	68.087	75.90
θ_{HOH}^0 (deg)	109.47	109.47	104.52	109.5	109.47	104.5	113.24
ϵ_{OO} ($kcal\ mol^{-1}$)	0.1554253	0.1554253	0.1521	0.1554253	0.1848	0.1522	0.154253
σ_{OO} (\AA)	3.165492	3.165492	3.150574	3.165492	3.165541	3.156	3.165492
ϵ_{HH} ($kcal\ mol^{-1}$)	0	0	0	0	0.01	0	0
σ_{HH} (\AA)					0.801809		
ϵ_{OH} ($kcal\ mol^{-1}$)	0	0	0	0	0.0429884	0	0
σ_{OH} (\AA)	0	0	0	0	1.593161	0	0
q_O (e)	-0.82	-0.8476	-0.834	-0.82	-0.82	-0.834	-0.82
q_H (e)	0.41	0.4238	0.417	0.41	0.41	0.417	0.41

Table 3.3: Parameters of some 3-site models [14]

can also be described by this equation by assuming infinitely large values for the length and bond stiffness. The parameters of some frequently used, 3-site water models can be found in table 3.3.

3.3 Statistical Mechanics

3.3.1 General Overview

Computational simulations on the atomic and molecular level produce microscopic information, such as the position and momentum of every atom in the system. From a classical point of view, this information completely describes the system. However, it is of no practical use. Ideally, we would like to obtain quantities that can be compared to macroscopic observations. The world we experience is of course a product of such microscopic behaviour. Devices for experimental measurements simply record average behaviour of this atomic description. For example a pressure sensor measures a force resulting from all the atomic collisions. It must therefore be possible to have a framework to interpret the macroscopic behaviour into observable quantities. **Statistical mechanics** is the discipline that translates the collective effort of the system's constituents into macroscopic properties that can be experimentally observed (e.g. temperature, pressure and thermal conductivity).

Here, we define a **microstate** as a possible configuration of all atoms in the system. It is described by explicitly defining the position \mathbf{r} and momentum, \mathbf{p} , of every atom. It can therefore be represented as a point in **phase space**, a mathematical space in which each point completely describes the system. For a system of N atoms, the $6N$ degrees of freedom (three for position and three for momentum) of an arbitrary microstate are denoted as the point $(\mathbf{r}^N, \mathbf{p}^N)$. Statistical mechanics deals with averages of collections of microstates (or points in phase space). Such sets of microstates are called **ensembles**.

Macroscopically, a system of interest is bounded by thermodynamic constraints. Con-

sider an experiment involving a liquid confined in a steel container in thermal equilibrium with its environment (i.e. the laboratory). Since the container is closed the number of atoms N is constant (no inflow or outflow). Assuming that the operating pressures of the liquid cannot deform steel, the volume of the system V is also fixed. Finally, the temperature T of the system is equal to that of the surrounding laboratory. The thermodynamic state of this system is therefore described by the variables NVT . Other variables can also be used to define the thermodynamic state of the system. Some of the most commonly used are

- NVE : Number of atoms, volume and energy are constant
- NVT : Number of atoms, volume and temperature are constant
- NPT : Number of atoms, pressure and temperature are constant

These variables also define ensembles. For example, an NVT ensemble consists of all the microstates which have a constant number of atoms in a fixed volume at a constant temperature. The main axiom of statistical mechanics is that all states within an NVE ensemble, have an equal probability of occurring. This means that any two microstates with the same number of atoms, residing in the same volume in space, and having the same energy, have an equal probability of occurring. This uniform probability distribution is given by

$$P_{NVE}((\mathbf{r}^N, \mathbf{p}^N)) = \frac{\delta(\mathcal{H}(\mathbf{r}^N, \mathbf{p}^N) - E)}{\sum_{micro} \delta(\mathcal{H}(\mathbf{r}^N, \mathbf{p}^N) - E)} \quad (3.3.1)$$

where \mathcal{H} is the **Hamiltonian** defined as the sum of the kinetic and potential energy (i.e. total energy of the microstate); N is the number of atoms in the system; E is the macroscopically dictated energy; and δ is the Kronecker delta given by

$$\delta(n) = \begin{cases} 1 & , n = 0 \\ 0 & , n \neq 0 \end{cases} \quad (3.3.2)$$

The NVE ensemble, which is called **microcanonical**, most accurately reflects the physical behaviour of an isolated system. Instead, the **canonical** (NVT) ensemble describes systems in contact with a heat bath (as is the case between the liquid and laboratory in the aforementioned example). If we assume that the combined heat bath and system are isolated and in thermal equilibrium at temperature T , one can derive the probability of finding the system in a specific microstate [133]. This is given by the Maxwell-Boltzmann distribution

$$P_{NVT}((\mathbf{r}^N, \mathbf{p}^N)) = \frac{\exp\left(\frac{-\mathcal{H}(\mathbf{r}^N, \mathbf{p}^N)}{\kappa_B T}\right)}{\sum_{micro} \exp\left(\frac{-\mathcal{H}(\mathbf{r}^N, \mathbf{p}^N)}{\kappa_B T}\right)} \quad (3.3.3)$$

where κ_B is the Boltzmann constant.

The **isothermal-isobaric** (*NPT*) ensemble is also often used. However, it is not used in our studies and will therefore not be considered here.

Statistical mechanics derives macroscopic properties by considering the average behaviour of an ensemble of microstates. A state variable \mathcal{A}_{macro} that can be measured experimentally has an equivalent instantaneous value, $\mathcal{A}(\mathbf{r}^N, \mathbf{p}^N)$. This can be evaluated from a single microstate. The two are linked through the **ensemble average**:

$$\mathcal{A}_{macro} = \langle \mathcal{A} \rangle_{ens} = \sum_{micro} \mathcal{A}(\mathbf{r}^N, \mathbf{p}^N) P_{ens}(\mathbf{r}^N, \mathbf{p}^N) \quad (3.3.4)$$

where $P(\mathbf{r}^N, \mathbf{p}^N)$ is the probability for this microstate to occur as explained above. The sum (rather than integral) follows from the quantum mechanical understanding that the system can only be in a discrete number of configurations. From a continuum point of view the sum would be replaced by integrals over the position and momentum in the three dimensions. For now we will continue with the discrete version of the equations as it enables a clearer understanding of some of the concepts explained.

It is impossible to evaluate equation 3.3.4 computationally (and of course analytically). The number of possible microstates is inconceivably huge. It is therefore important to devise a method to sample a much smaller portion of the phase space to use for property calculations. In order to evaluate accurate results, we must select a representative subset of the entire ensemble. The sampling method depends on the molecular method employed.

The “natural” way would be to set initial values for the positions and momenta of the atoms and allow the system to evolve in time through Newton’s laws of motion. By “natural” we imply a resemblance between the sampling sequence method and the way in which physical systems evolve. The system at each point in time reflects a new point in phase space within the microcanonical ensemble (since Newton’s laws conserve energy and mass). The ensemble average is then replaced by the time average

$$\mathcal{A}_{time} = \frac{1}{t_{obs}} \int_0^{t_{obs}} \mathcal{A}(\mathbf{r}^N(t), \mathbf{p}^N(t)) dt \quad (3.3.5)$$

For an accurate approximation of \mathcal{A} we hope that after a sufficiently long time (i.e. large t_{obs}), the system will have sampled a representative portion of the phase space. The condition for this to be true is discussed below. The time-evolution-based approach for sampling the system is the framework adopted by the Molecular Dynamics method.

An alternative approach, closer to the conventional formulation of statistical mechanics, is to stochastically sample points in phase-space and calculate the ensemble average using equation 3.3.4. Of course the quality of the sample depends on the sampling scheme used. This technique is the one adopted by Monte Carlo methods. Both, the Molecular Dynamics and Monte Carlo method will be discussed briefly in sections 3.3.3 and 3.3.2 respectively.

The time average, over an infinitely long time, should produce the same results as that of the ensemble average. For this to be true, the evolution of the system through time should eventually span all the points in phase space corresponding the ensemble. Such a system is referred to as **ergodic**. However this is not always the case. If a trajectory in phase space returns to a previously visited point, the deterministic nature of Newton's equations will impose the exact same trajectory. This will form a loop in phase space which prevents unbiased sampling. If an MD simulation starts in or falls into that loop, there is a good chance that the results will not be accurate. Instead, the Monte Carlo (MC) jumps to points in phase space probabilistically. Therefore, for appropriate sampling methods the aforementioned problem can be circumvented.

Calculation of Properties

The preceding section has highlighted the general framework of statistical mechanics. Here we explicitly discuss how to calculate specific properties of interest to our studies.

An important theorem in statistical mechanics is that of **energy equipartition**. It states that every degree of freedom in the Hamiltonian contributes, on average, by $\kappa_B T$ to the total energy of the system. For an arbitrary degree of freedom, \mathcal{D} , the equipartition theorem is formulated as

$$\left\langle \mathcal{D}_n \frac{\partial \mathcal{H}}{\partial \mathcal{D}_m} \right\rangle = \delta(m - n) \kappa_B T \quad (3.3.6)$$

where $\delta(m - n)$ is the Kronecker delta defined in equation 3.3.2. For momentum degrees of freedom which appear quadratically in the Hamiltonian the theorem is formulated as

$$\left\langle \frac{\mathbf{p}_i^2}{m_i} \right\rangle = \frac{1}{2} \kappa_B T \quad (3.3.7)$$

where m is the mass of the atom. This means that the total, average kinetic energy, which is a sum over $3N$ degrees of freedom (three dimensions for all atoms) is equal to

$$\begin{aligned} \langle \mathcal{K} \rangle &= \sum_{i=1}^{3N} \left\langle \frac{\mathbf{p}_i^2}{m_i} \right\rangle = \frac{3N}{2} \kappa_B T \\ \Leftrightarrow T &= \frac{2\mathcal{K}}{3N\kappa_B T} \end{aligned} \quad (3.3.8)$$

where \mathcal{K} is the kinetic energy. The relationship links the temperature of the system with the average kinetic energy.

If we consider the atomic positions of the system, equation 3.3.6 provides a relationship for the pressure of the system. This is given by

$$p = \frac{N\kappa_B T + \langle \mathcal{W} \rangle}{V} \quad (3.3.9)$$

where p is the pressure of the system; V is the volume of the system; and \mathcal{W} is the **virial** term describing the work done on an atom by its neighbours. This is calculated using

$$\mathcal{W} = \frac{1}{3} \sum_i \mathbf{r}_i \cdot \mathbf{F}_i \quad (3.3.10)$$

In micro and nanoflows, it is important to study the distribution of the fluid atoms/molecules. Unlike macroscopic assumptions, large density gradients tend to form close to interfaces. Such inhomogeneities often provide explanations to phenomena untreated by continuum methods. For the majority of our investigations, we study the structure of the fluid by plotting density profiles in relation to the simulation box. This is achieved by dividing the domain into regions. In each such region we evaluate the number density given by

$$\rho_R = \frac{N_R}{V_r} \quad (3.3.11)$$

where R is the region in question; ρ is the number density; N is the number of atoms; and V is the volume of the region. Because of the random motion of fluid atoms, a single evaluation of the number density will contain noise. This can be reduced by calculating the ensemble (equation 3.3.4) or time (equation 3.3.5) average (see section 3.3.1).

Rather than calculating the density as a function of a fixed, spatial frame of reference, we sometimes need to understand how atoms are distributed relative to each other. A good example, relevant to this project, is the study of the liquid distribution around the solid nanoparticle in nanofluids. If the solid particle were perfectly still, the density profiles described above would be perfectly adequate for such a task. However, the nanoparticle is following Brownian motion. Consequently, its position is changing randomly and constantly. Averaging the density of fixed regions will therefore produce a smudged profile with no significant information. One way to overcome this problem is to redefine regions around the particle before each calculation of the density.

Another approach is to use Radial Distribution Function (RDF). The RDF calculates the probability of finding a pair of atoms at a distance r_{ij} in a system, compared to that of a completely random atomic configuration. More intuitively, it describes how the density of a substance varies with the radial distance from an atom. The RDF is usually derived and formulated using probability theory. Here, we provide the alternative and equivalent formulation, more convenient for computational calculations [124]. This is given by

$$g(r) = \frac{V}{N^2} \left\langle \sum_i \sum_{j \neq i} \delta(r - r_{ij}) \right\rangle \quad (3.3.12)$$

where $g(r)$ is the RDF.

Equation 3.3.12 calculates the distribution of particles around a single atom. In many cases (such as that of nanofluids) we want to calculate the average distribution of atoms of

type B around atoms of type A . For this we can use

$$\langle g(r) \rangle_A = \frac{V}{N^2} \left\langle \sum_{i \in B} \sum_{j \neq i \in B} \delta(r - r_{ij}) \right\rangle \quad (3.3.13)$$

where $\langle \rangle_A$ denotes an average over all atoms of type A and i and j iterate over all atoms of type B . Furthermore, in practice, the definition of δ needs to be relaxed so that it is equal to 1 in a range $-\Delta r < r - r_{ij} < \Delta r$. This gives the particle distribution in radial bins.

We can also calculate velocity and temperature profiles by dividing the simulation box into regions. Since the velocity of each atom is readily available, the velocity of each region is the average over all atoms. Furthermore, 3.3.8 can be used to calculate the temperature of each region.

The evaluation of **transport properties** is more complicated. Their process-dependent nature prohibits the definition of an instantaneous value that can be averaged using equations 3.3.4 or 3.3.5. Furthermore, transport properties are described by how a quantity evolves in space and time. For example, the thermal conductivity indicates how much energy moves across a material per unit time. Since MC formulations have no strict definition of time, the MD method is preferable for the calculation of such quantities.

An important phenomenon in fluids is **diffusion**. It is a process in which atoms and molecules migrate from high-concentration regions to lower ones. This phenomenon is different to advection where fluid flows in bulk due to a pressure difference. In diffusion, the motion is a product of the stochastic molecular motion. A common example is a drop of dye in water. Initially, the dye will be concentrated in one small area. However, in a very short time it will spread across the volume of the water. From a macroscopic perspective, diffusion is governed by Fick's law, given by

$$\mathbf{J}_D = -D \nabla c \quad (3.3.14)$$

where \mathbf{J}_D is the diffusion flux, c is the concentration of the diffusing substance; and D is the diffusion coefficient describing how fast the substance diffuses.

Although diffusion is commonly described between two different materials, we are often interested in **self-diffusion**. This describes the motion of atoms within a pure substance. From a microscopic perspective, the diffusion coefficient can be given by [133]

$$2tD = \frac{\partial}{\partial t} (\text{MSD}(t)) \quad (3.3.15)$$

Here, $\text{MSD}(t)$ is the Mean Square Displacement (MSD). It calculates the mean distance travelled by a set of particles compared to an initial reference point in time. It is given by

$$\text{MSD}(t) = \langle (\mathbf{r}(t) - \mathbf{r}(0))^2 \rangle = \frac{1}{N} \sum_{i=1}^N (\mathbf{r}_i(t) - \mathbf{r}_i(0))^2 \quad (3.3.16)$$

where $r_i(t)$ is the position of the particle i at the current point in time and $r_i(0)$ is its position at the initial reference point. For liquids, the mean square displacement as a function of time is a straight line. Therefore we can trivially calculate its derivative and hence the diffusion coefficient. Solids on the other hand, have atoms which oscillate around a fixed position. Therefore the MSD reaches a plateau after a very short time.

In confined fluids, of interest to this thesis, the displacement of the atoms is obviously bounded by the spatial restrictions of the system. Therefore the mean square displacement cannot be used to accurately calculate the diffusion coefficient. However, the slope can still provide qualitative information regarding the fluid behaviour.

The investigations presented here mostly concern the thermal conductivity of systems. Statistical mechanics provide two main methods to calculate it using MD; the Non-Equilibrium Molecular Dynamics (NEMD) approach [134] and Equilibrium Molecular Dynamics (EMD) approach.

The NEMD method calculates the thermal conductivity in a manner analogous to most experimental measurements. It is therefore called the **direct** method (figure 3.12). The first step is to introduce a temperature gradient in the system. This can be achieved by fixing the temperature of two regions at different values. Once the system reaches steady state conditions, the energy flux across the two regions is measured. Plotting the temperature profiles (which should be linear) the temperature gradient can be trivially measured. Then Fourier's law of conduction (equation 2.1.1) is used to calculate the thermal conductivity.

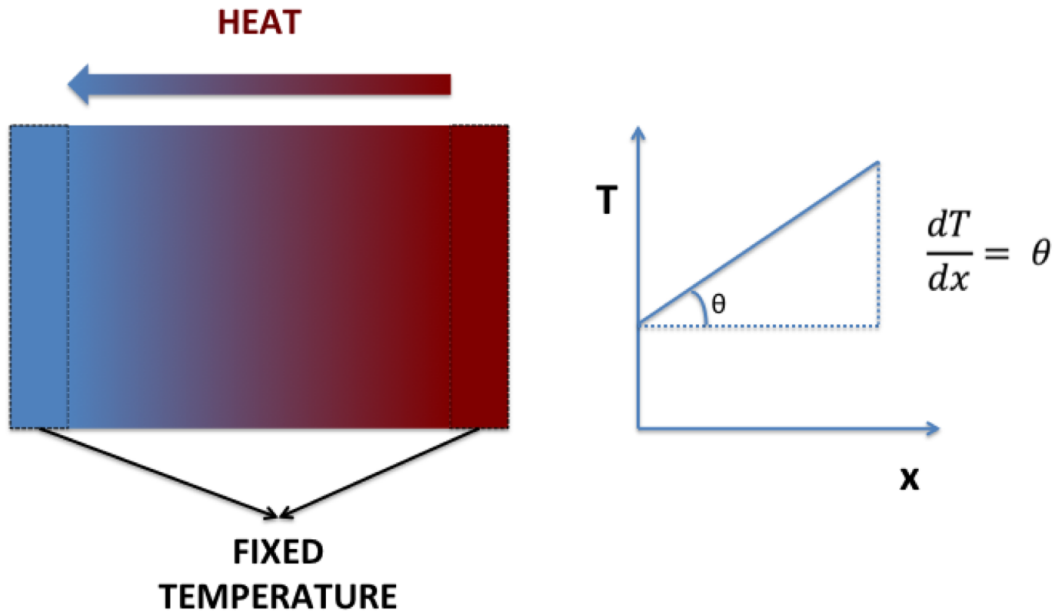


Figure 3.12: Schematic representation of the NEMD method for calculating the thermal conductivity. First a temperature difference is introduced between two regions. Once the system has reached steady state, the heat transferred from the hot to the cold region is measured. The heat and the temperature gradient extracted from the linear temperature profile are then used in Fourier’s law of conduction to realise the thermal conductivity

The ease of implementing the direct method and its intuitive nature within the engineering community has rendered it the preferred method for many. However, it has been found to be problematic under certain conditions. For example in severely confined fluids, the temperature profiles are often non-linear which complicates the calculation of the thermal conductivity [135].

The EMD method for computing the thermal conductivity is slightly more elaborate. It evaluates the property in the absence of a temperature profile, a concept which can be confusing. The confusion arises from the macroscopic understanding that under equilibrium conditions there is no energy transfer in the system. The entropy is considered to have reached a maximum with no observable fluctuations. The stochastic definition of entropy given by statistical mechanics gives it the same directionality towards higher values. However, it allows for the probability of a spontaneous decrease. This is accompanied by energy, concentration and momentum fluctuations in the system. The EMD approach monitors the dissipation patterns in such fluctuations and makes predictions about the system under non-equilibrium conditions. The **Green-Kubo** relation [136, 137] provides the framework for this computation. For the thermal conductivity, this is given by

$$\lambda = \frac{V}{\kappa_B T^2} \int_0^{t_{cor}} \langle J(0) \cdot J(t) \rangle dt \quad (3.3.17)$$

Here, J is the microscopic heat flux that quantifies the energy transfer due to the stochastic behaviour of atoms; V is the volume of the system; $\langle J(0) \cdot J(t) \rangle$ is an autocorrelation function; and t_{cor} is the correlation length (i.e. the amount of time for which the system will be sampled for the autocorrelation function). In signal processing, the autocorrelation function identifies patterns within a noisy signal. It does so by observing it at different times and comparing them to an initial reference point. The greater the resemblance to this reference point, the more the two are said to be correlated and the greater the value of the autocorrelation function. In the present case, the heat flux is observed at some arbitrary point in time. The collisions between the atoms will cause energy fluctuations in the system. The system is checked at subsequent points in time to see whether, and by how much, these fluctuations persist.

In equilibrium, these fluctuations are short-lived (which is why they are not observable macroscopically). Therefore, after a certain amount of time, depending on the system being studied, there will be no correlation between the fluctuation patterns of the new state and the one of the initial frame of reference. The autocorrelation function of the microscopic heat flux, which is referred to as Heat Flux Autocorrelation Function (HFACF), will decay to zero. Therefore, the volume under the curve will be finite and the integral of equation 3.3.17 will be well defined for a large enough correlation length. The time it takes to decay is related to the phonon relaxation time [135].

On the contrary, if there is a temperature gradient within the system, the HFACF will always detect energy transfer towards the cold region. This constant pattern will cause the HFACF to converge to a positive value. The thermal conductivity will not be well defined since for an infinite correlation length its value will also be infinite.

We have so far omitted defining the microscopic heat flux J . For calculating the thermal conductivity of a pure material in a simulation that uses pairwise potentials, it is given by

$$J = \frac{1}{V} \left[\sum_i \mathbf{v}_i E_i + \frac{1}{2} \sum_{ij} \mathbf{r}_{ij} (\mathbf{F}_{ij} \cdot \mathbf{v}_i) \right] \quad (3.3.18)$$

where i and j are atoms in the system; E_i is the kinetic and potential energy of the atom; and F_{ij} is the force between atoms i and j . For simulations using many-body potentials, the formula is adapted. Although not within the scope of this thesis, a number of investigations review various formulations of the microscopic heat flux [138, 139].

Complications arise when a binary system, such as a nanofluid, is in question. The enthalpy of mixing due to the inter-diffusion of the two materials is not accounted for by equation 3.3.18. For a more accurate calculation of the thermal conductivity, we need to consider the partial enthalpies of each substance. The microscopic heat flux takes the form

$$J = \frac{1}{V} \left[\sum_i \mathbf{v}_i E_i + \frac{1}{2} \sum_{ij} \mathbf{r}_{ij} (\mathbf{F}_{ij} \cdot \mathbf{v}_i) - \sum_i h_i \mathbf{v} \right] \quad (3.3.19)$$

where i is an arbitrary substance (one of the two substances in binary systems); and h is the partial enthalpy. An accurate calculation of this quantity using molecular dynamics requires a series of simulations within the isothermal-isobaric ensemble (NPT). However, for nanofluids this term can be satisfactorily evaluated as the sum of the averages of the potential and kinetic energies and virial term (equation 3.3.10) [34, 140]. For pure materials, the third term in the equation should vanish. Therefore, equation 3.3.19 is used for all the calculations in this study.

There are a few factors that can compromise the accuracy of the Green-Kubo relation. The first is the definition of the correlation length. If it is smaller than the time required for the HFACF to decay, then it will under predict the thermal conductivity. However, this is easy to detect and fix by plotting it against time. If it hasn't converged to zero it means the correlation length needs to be increased. In addition for accurate calculations using the Green-Kubo approach, the system size needs to be large enough to accommodate the phonon mean-free-path [141]. This depends on the system being modelled. Finally, it is worth mentioning that the HFACF is accompanied by significant statistical noise. The larger the correlation length the more the noise accumulates. Regression is often carried out in order to obtain a smoother function and reduce numerical error [142].

For the investigations presented here, we calculate the thermal conductivity exclusively using the Green-Kubo relation. The first reason is the aforementioned issue of the direct method for confined liquids. The second (and most important one) is that the nature of the HFACF provides information on the heat transfer mechanism of the system. This, rather than the absolute values of the thermal conductivity, is of primary importance to our investigations.

A final remark is that molecular models such as MC and MD do not consider the electronic structure of the atom. Therefore, the calculation of the thermal conductivity of metals using MD is not possible since energy is transferred through electrons.

3.3.2 Monte Carlo

The Monte Carlo (MC) method is a framework which randomly samples a distribution to obtain numerical results efficiently and accurately. It is a powerful tool for a wide spectrum of disciplines (e.g. computer science, mathematics, economics, physics). There is no specific formulation and each individual implementation can vary significantly.

This section briefly outlines some concepts regarding the MC method in the scope of statistical mechanics. The intention is to provide an understanding of the nature of the algorithm. Details regarding various sampling methods, optimisation techniques and random number generation are omitted here. For more details the reader is referred to the literature [124, 133].

The MC method can potentially provide an efficient means to calculate integrals over many degrees of freedom. Statistical mechanics use this to compute the ensemble average for properties of interest (equation 3.3.4). Since the momentum terms in the equation are quadratic, their integration can be computed analytically. Therefore, we only focus on how to compute the potential energy component of the ensemble average. Since we are only concerned with the positions of all atoms, we are dealing with configuration space (\mathbf{r}^N) rather than phase space ($\mathbf{r}^N, \mathbf{p}^N$). Here, we will use the canonical ensemble as a concrete example. The potential component of the ensemble average in the NVT ensemble is given by

$$\langle \mathcal{A} \rangle = \int_{\mathbf{r}^N} P_{NVT}(\mathbf{r}^N) \mathcal{A}(\mathbf{r}^N) d\mathbf{r}^N \quad (3.3.20)$$

where here we give $P_{NVT}(\mathbf{r}^N)$ in configuration space (rather than phase space)

$$P_{NVT}(\mathbf{r}^N) = \frac{\exp\left(\frac{-\mathcal{V}}{k_B T}\right)}{\int_{\mathbf{r}^N} \exp\left(\frac{-\mathcal{V}}{k_B T}\right) d\mathbf{r}^N} \quad (3.3.21)$$

In the following sections we briefly discuss how the MC method can be used to solve equation 3.3.20

A naive MC approach

First consider an arbitrary integral

$$\mathcal{F} = \int_a^b f(x) dx \quad (3.3.22)$$

where f is the function being integrated. We can re-write this integral as

$$\mathcal{F} = \int_a^b f(x) dx = \int_a^b \frac{f(x)}{P(x)} P(x) dx \quad (3.3.23)$$

where P is an arbitrary probability density function. The equation is the statistical average (expected value) of the quantity $\frac{f(x)}{P(x)}$ and we can write it as

$$\langle \mathcal{F} \rangle \approx \left\langle \frac{f(x)}{P(x)} \right\rangle_{N_{trials}} \quad (3.3.24)$$

where N_{trials} is the number of points sampled from $P(x)$ in the range $[a, b]$. The larger it is the more accurate the estimate for \mathcal{F} (law of large numbers).

We refer to this approach as “naive” since it does not take into account the nature of the function being integrated (in this case $f(x)$). A simple example demonstrating the inefficiency of such an approach is the integration of a gaussian distribution with a small standard deviation. Using the unbiased sampling method described above, most of the computational time would be spent on values of x for which $f(x)$ is insignificant (i.e. past the standard deviation).

We face the same problem in statistical mechanics. A microstate can be in a large (infinite according to continuum mechanics) number of different configurations. However most of those are not physically probable. For example the canonical ensemble contains configurations with overlapping atoms. The probability of such states occurring ($P_{NVT}(\mathbf{r}^N)$) is therefore minute and their contribution towards the calculation of a quantity \mathcal{A} is negligible. The unbiased sampling method discussed here would spend most of its computational resources on such insignificant states. Furthermore, a very large sample size would be required to produce an accurate estimation. This is because, eventually we also require trials from the significant parts of the distribution.

What we require is a method for sampling more meaningful values. This is the theory of importance sampling described next.

Importance sampling

Importance sampling is a method that overcomes the above problem by sampling regions important to the integral.

In equation 3.3.23 we said that the choice of P is arbitrary. However, it can be shown that for the same sample size, the error is reduced if the term $\frac{f(x)}{P(x)}$ is a smooth function of x [133]. In fact, the optimal solution would be for $\frac{f(x)}{P(x)}$ to be constant.

For the calculation of a property \mathcal{A} in the canonical ensemble, a suitable choice for P is $P_{NVT}(\mathbf{r}^N)$ (equation 3.3.21). Combining equation 3.3.20 and 3.3.24, along with the choice of $P(x) = P_{NVT}(\mathbf{r}^N)$ we get

$$\langle \mathcal{A} \rangle = \langle \mathcal{A} \rangle_{N_{\text{trials}}} \quad (3.3.25)$$

All we have done so far is to simplify the functional form of the problem. The real essence of the solution is to devise a method to sample states (\mathbf{r}^N) according to their probability $P_{NVT}(\mathbf{r}^N)$. A common method to produce a sequence of states is by simulating a **Markov chain**; a random walk through the space of interest (in this case the configuration space) in which the next step depends exclusively on the current one. The path is generated based on a given set of rules which depend on the specific application.

We now want to generate a set of points based on a probability distribution $P(x)$. Lets denote the current state as x . In general, the system will move to a new state x' with a

probability given by the **transition operator** $P(x \rightarrow x')$. A useful condition to start with is that of detailed balance which is formulated by

$$P(x)P(x \rightarrow x') = P(x')P(x' \rightarrow x) \quad (3.3.26)$$

This says that the probability of leaving state x to go to x' is the same as that leaving from x' to go to x . Once we obtain a number of samples in a state x which corresponds to $P(x)$ (which remember is the desirable outcome), equation 3.3.26 maintains this equilibrium condition. It does so by reciprocating any states leaving from x by an equal number of states arriving to it from other states. Rearranging the above equation we get

$$\frac{P(x \rightarrow x')}{P(x' \rightarrow x)} = \frac{P(x)}{P(x')} \quad (3.3.27)$$

The MC move consists of two steps, both of which are encoded in the transition operator. First, the next state must be proposed. This is achieved by a proposal distribution $g(x \rightarrow x')$. Second, a set of rules must determine whether or not this proposed state should be accepted. This is done through the acceptance operator $A(x \rightarrow x')$. The transition operator can then be written as

$$P(x \rightarrow x') = g(x \rightarrow x')A(x \rightarrow x') \quad (3.3.28)$$

Substituting equation 3.3.28 into 3.3.27 we get

$$\frac{A(x \rightarrow x')}{A(x' \rightarrow x)} = \frac{P(x')g(x' \rightarrow x)}{P(x)g(x \rightarrow x')} \quad (3.3.29)$$

The choice of the acceptance and proposal operators varies between different implementations. It is often the case that the proposal operator is chosen to be symmetric (i.e. $g(x' \rightarrow x) = g(x \rightarrow x')$). It would therefore vanish from the above equation. In statistical mechanics, the most frequently used model is the **Metropolis method**. If we assume a symmetric proposal operator (which is often the case in practice), the Metropolis scheme formulates the probability of acceptance by

$$A(x \rightarrow x') = \begin{cases} \frac{P(x')}{P(x)} & , P(x') < P(x) \\ 1 & , P(x') \geq P(x) \end{cases} \quad (3.3.30)$$

The above says that if $P(x') \geq P(x)$ then the new state is accepted immediately. Otherwise the state is accepted with probability equal to the ratio $A(x \rightarrow x') = \frac{P(x')}{P(x)} < 1$. To determine whether the latter case is accepted, a random number is chosen between 0 and 1. If this random number is smaller than $A(x \rightarrow x')$ then the x' is accepted and becomes the new x . Otherwise it is rejected and the state remains the same.

Returning to our problem of statistical mechanics, the probability distribution from which the system should be sampled is $P_{NVT}(\mathbf{r}^N)$. Recall from earlier that the difficulty in using this function is the normalising factor, which integrates over the entire configuration space. However, if we substitute this into eq 3.3.30 then the ratio of the probabilities

eliminates the normalising factor and leaves

$$A(\mathbf{r}^N \rightarrow \mathbf{r}'^N) = \begin{cases} \frac{P_{NVT}(\mathbf{r}'^N)}{P_{NVT}(\mathbf{r}^N)} = \exp\left(-\frac{\mathcal{V}(\mathbf{r}'^N) - \mathcal{V}(\mathbf{r}^N)}{\kappa_B T}\right) & , P_{NVT}(\mathbf{r}'^N) < P_{NVT}(\mathbf{r}^N) \\ 1 & , P_{NVT}(\mathbf{r}'^N) \geq P_{NVT}(\mathbf{r}^N) \end{cases} \quad (3.3.31)$$

We now give a more intuitive explanation to this equation. It states that if the energy of the system of the proposed state \mathbf{r}'^N is lower than that of \mathbf{r}^N (this is the case in which $P_{NVT}(\mathbf{r}'^N) \geq P_{NVT}(\mathbf{r}^N)$) then then the current state is immediately changed into \mathbf{r}'^N . If however, the energy of the proposed state is higher, then there is only a probability of being accepted which is given by the Boltzmann factor $\exp\left(-\frac{\mathcal{V}(\mathbf{r}'^N) - \mathcal{V}(\mathbf{r}^N)}{\kappa_B T}\right)$. This probability depends on the ratio of the two energies. The larger the energy of the proposed state is in comparison to the current state, the smaller the probability of switching states. Therefore, the trajectory in configuration space has a tendency towards lower energy states. This resembles the laws of motion as given by equation 3.2.2 in which the force on a system is trying to change its state to one with a lower potential energy.

In the metropolis scheme, the generation of the next trial state ($g(\mathbf{r}^N \rightarrow \mathbf{r}'^N)$) is implemented by randomly displacing some of the atoms.

In general, the algorithm for the metropolis method consists of three steps

1. Randomly select an atom and calculate its potential energy $\mathcal{V}(\mathbf{r}^N)$
2. Displace the atom by a random distance Δ so that its new position is $r' = r + \Delta$
3. Accept this displacement with a probability given by 3.3.31.

The states produced should give a good sample to calculate the ensemble average. Of course, the error is still dependent on the sample size: the larger the sample the more accurate the results.

3.3.3 Molecular Dynamics

Molecular Dynamics (MD) is a computational method for simulating the physical behaviour of a system. The positions and momenta of all atoms evolve in time using Newton's equations of motion

$$F = m \frac{d^2 \mathbf{r}}{dt^2} \quad (3.3.32)$$

The system is sampled at different timesteps during this natural evolution. The samples accumulated during the simulation can be used for the calculation of the time average (equation 3.3.5). Assuming the system is ergodic and that the runtime was long enough to allow for a sufficient exploration of the system, an accurate estimation of the property in question should be evaluated.

Generally, an MD run has the following steps

- Initialization of system
- Calculation of interatomic forces
- Integration of equations of motion
- Calculation of statistical time averages

These are discussed in the following sections

System Initialisation

A crucial part of MD is a correct initialisation of the system. We need to provide the solver with necessary information to solve the equation of motion. This includes the size of the simulation box, the potentials between atom types, operating initial temperature of the system, and density. The next step is to set the positions and velocity of all the atoms.

First of all, the potential of the system needs to be defined (see section 3.2.3). This enables the calculation of the force (equation 3.2.2) that will subsequently be used for calculating the new atomic positions (equation 3.3.32).

The initial positions of the particles are also important. Crystalline materials such as CNTs and graphene are defined by their symmetric structure. The atoms need to be placed accurately to reflect this symmetry. This can be achieved by defining a lattice and a basis (section 3.1). The atoms can then be placed on the lattice points. The size of the unit cell will also define the density of the crystal.

Fluids on the other hand, do not have fixed positions for their atoms. They are moving randomly in constantly varying directions. It might therefore seem that they can be positioned randomly. Such a distribution however, might produce an undesirable behaviour. If atoms overlap, strong forces (due to the Pauli exclusion principle) will repel them with high velocities. One way of dealing with this problem is to restrict the atomic motion such that they can only move up to a limited distance at each timestep. After some time, the atoms will move away from each other and the restrictions can be relaxed.

Fluid particles can also be placed initially on a lattice (as is the case for solid crystals). Although they will inevitably move into an amorphous and variable configuration, this ensures that no overlapping occurs during the initial timesteps.

The atoms need to be allocated initial velocities. The velocities are selected based on a probability distribution. This is usually a uniform or a Gaussian function. Usually we

want the system to start at a specific temperature. If the velocities were selected from a uniform distribution, they can be rescaled so that the average kinetic energy produces the desired temperature, as per the equipartition theorem (equation 3.3.8). For the Gaussian distribution, the mean and standard deviation are set accordingly so that the selected values result in the requested temperature.

Calculation of forces

Given the relevant potentials, the calculation of the force is theoretically simple (equation 3.2.2). This however, is the most time-consuming part of an MD simulation. Even if only pairwise interactions are considered, for a system of N atoms, there are $\frac{N(N-1)}{2}$ pairs to be considered at every timestep. A naive approach will therefore have a time complexity of $O(N^2)$.

A minor optimisation technique is to define a cut-off distance r_c . This defines a radius around a particle beyond which the interatomic interactions will be disregarded. The cut-off distance needs to account for the nature of the potentials of the atoms being modelled. It should be large enough to include distances in which the potential is significant. Although this can save a significant amount of time, all pairs will still need to be checked whether or not they fall within arbitrarily defined proximity.

Various speed-up methods are available [133]. One of the most effective and frequently used are the **Verlet lists** (often referred to as **neighbour lists**) [143]. A distance r_v greater than the aforementioned cut-off distance is defined. For each atom i , the particles within a radial distance r_v from it are stored in a list. For subsequent timesteps, the forces can be calculated directly by considering the atoms in these lists. This operation has a computational complexity of $O(N)$. If an atom moves more than $r_v - r_c$ at any timestep, the Verlet lists must be re-computed (which again is $O(N^2)$).

Integration of equations of motion

For MD, Newton's second law (equation 3.3.32) is usually integrated using the **Verlet algorithm**. It is often preferred due to its simplicity and accuracy. The equation is

$$\mathbf{r}(t + \Delta t) = 2\mathbf{r}(t) - \mathbf{r}(t - \Delta t) + \frac{\mathbf{F}(t)}{m}\Delta t^2 + O(\Delta t^4) \quad (3.3.33)$$

where Δt here denotes the molecular timestep and the term $O(\Delta t^4)$ the order of error.

This equation is derived by summing the Taylor expansions of $\mathbf{r}(t + \Delta t)$ and $\mathbf{r}(t - \Delta t)$. The sum eliminates any terms containing the velocity. We can still obtain it by considering

the trajectory calculated from the Verlet algorithm

$$v(t) = \frac{r(t + \Delta t) - r(t - \Delta t)}{2\Delta t} + O(\Delta t^2) \quad (3.3.34)$$

However the accuracy is of the order Δt^2 . In many cases this might not be satisfactory. There are other methods for calculating the velocity more accurately, although these will not be discussed here.

Calculation of time-averages

The calculation of time-averages is explained in more detail in section 3.3.1. Once the system is initialised and the simulation starts running, the system is sampled at regular intervals. At the end of the simulation these are averaged together in an attempt to predict the macroscopic property.

It is common practice however, to allow for an initial **equilibration phase**. This is a period given for the system's parameters (e.g. temperature, pressure) to relax. During this period, we generally avoid taking samples for the calculation of properties. The length of the equilibration phase depends on the system. It is generally advised to calculate and output state variables at each timestep to check for convergence.

Thermostats (NVT)

Newton's laws of motion conserve energy and mass. Therefore, any time averages calculated are equivalent to the ensemble averages in the microcanonical ensemble (*NVE*). However, the canonical (*NVT*) and isothermal-isobaric (*NPT*) ensembles are of practical importance.

Monte Carlo methods can simply adjust their sampling distribution function to reflect any ensemble. In MD this is more complicated due to its fundamental microcanonical-based nature. It either requires to adjust equation 3.3.32 or somehow incorporate MC moves. Although the isobaric ensemble is very useful and commonly used in MD simulations, it is of no interest to this study and will therefore be ignored. Here we focus on how the *NVT* ensemble can be simulated. A large number of studies investigate accurate methods for controlling temperature. Here we briefly discuss two of the most commonly used techniques.

In section 3.3.1 the *NVT* example was defined by considering the system in question as being in contact with a heat bath. The **Andersen** thermostat [144] tries to model the interaction between the system and heat bath. This is emulated by introducing stochastic collisions on particles in the system. At each timestep each atom has a uniform probability

to “collide”. The strength of the interaction between the heat bath and the system is defined by the frequency parameter. The probability of a particle colliding increases with increasing frequency. In the event of a collision of an atom, its velocity is reset by selecting it from the Maxwell-Boltzmann distribution. In the absence of a collision an atom still behaves according to equation 3.3.32.

An alternative approach for setting the temperature of the system is the **Nose-Hoover** thermostat [145, 146]. This approach adjusts the equation of motion. Using Lagrangian mechanics, a reformulation of Newton’s equations, auxiliary, artificial dimensions are introduced to manifest the *NVT* ensemble. This is the most commonly used thermostat in MD simulations.

Another approach to set the temperature of a system is to rescale its atomic velocities accordingly so that the average kinetic energy gives the desired temperature (equation 3.3.8). The rescaling does not change the relationship between the velocities of different atoms. This approach however, does not correspond to any statistical ensemble [133]. It is therefore often avoided during the calculation of properties. However, it is commonly used to regulate temperature, either during equilibration phase (after which the rescaling stops) or for parts of the system that are not considered for the calculation of any properties.

3.4 Conclusions

In this section we have provided the general background required for an understanding of the models and tools used in the chapters to follow.

First we provided an brief introduction to crystallography. This might seem irrelevant to the topic of this thesis. The concepts described are however used for the creation of the solid channel walls. Furthermore, many studies on fluids initially place the atoms on a crystal lattice to avoid any overlapping. In our studies, liquid atoms are placed randomly (see section 3.3.3) for reasons described later (see chapter 4).

Next we provided a very brief introduction to intramolecular and intermolecular interactions. The section also describes some techniques that are often used to realise such forces computationally. One could skip the physical description of these chemical interactions and directly focus on section 3.2.3. The systems considered here have well established modelling techniques that can be used without knowledge of their underlying physics. However, we strongly believe that a more in-depth understanding of these concepts facilitates a more collective view of the models and the results.

Finally, we have also given a short introduction to statistical mechanics. This is crucial for understanding the methodologies employed here for calculating system properties. In addition, we briefly explain the main concepts behind MD and MC. All of the studies in

this thesis use MD. Since MC does not have a strict definition of time, it is not so suitable for the calculation of transport properties. Since the thermal conductivity is the primary interest of the studies, MD is the most reasonable choice.

The molecular dynamics code used here is the open source program Large Scale Atomic/Molecular Massively Parallel Simulator (LAMMPS)[147]. Its extensibility (since it is open source) and its involved community are both attractive traits.

Thermal Behaviour of Confined Liquids

4.1 Introduction

In this section we study how the simple act of confining a liquid affects its thermal properties. As discussed in the introduction, MD simulations have proven to be effective for understanding such systems. The majority of investigations on nanoflows focus on the slippage of the fluid adjacent to the channel walls [148–151]. These have successfully resolved discrepancies between experimental work [152, 153] and the applicability of the no-slip condition often employed in Computational Fluid Dynamics (CFD) simulations.

However, thermal properties have also been investigated. The thermal conductivity has been studied before as a function of the channel width [154, 155]. The same studies have observed that the thermal conductivity and diffusion coefficient are anisotropic between the directions parallel and normal to the walls. In addition, investigations have correlated the Kapitza resistance (thermal resistance at the solid-liquid interface) [156, 157] with the wall and liquid properties as well as the channel width.

We believe however, that more attention is needed on the thermal behaviour of such nanofluidic environments. Furthermore, our main focus is not to estimate accurate values of the thermal conductivities under various conditions. We are mostly interested in understanding the physical mechanisms that promote heat transfer, and how they differ from those in unconfined liquids.

In this chapter, we focus on the thermal conductivity in the directions parallel to the channel walls. The aforementioned anisotropy of properties in nanochannels [154, 155] suggests that our conclusions do not apply in the direction normal to the channel walls and do not accurately describe the total thermal conductivity of the system (averaged over all three directions). The conscious decision of studying the parallel direction stems from our understanding that most thermal management applications attempt to transfer heat in the streamwise direction, that is, parallel to the channel walls.

4.2 Computational Model

Here we describe the MD model for liquid argon confined in two parallel, idealised solid walls (figure 4.1). Many of the units used are in reduced units (see appendix A). However, the thermal conductivity is converted to units of SI for a trivial comparison with the experimental observed value for argon.

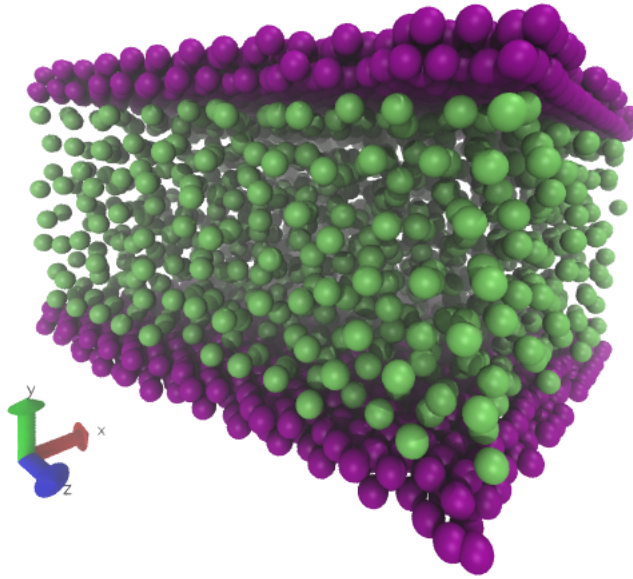


Figure 4.1: MD model of liquid argon confined in a nanochannel, visualized using VMD

First, we define the potentials describing the dynamics of the system. As a noble gas, argon atoms interact via London dispersion forces. These can be modelled through a Lennard-Jones (LJ) potential (section 3.2.3). The LJ parameters for the argon particles are $\epsilon_{ll} = 1.0\epsilon$ and $\sigma_{ll} = 1.0\sigma$, where ϵ and σ are the strength of the interaction and molecular length, respectively. For the interactions between the solid walls and liquid argon particles, $\epsilon_{wl} = 0.8\epsilon$ and $\sigma_{wl} = 0.75\sigma$ are used. The wall atoms are fixed using spring potentials of stiffness $\kappa = 500\epsilon\sigma^2$. This allows them to vibrate while interacting naturally with the liquid particles[156].

Next we discuss the geometrical structure of the system. The walls of the channel are fixed perpendicular to the y -direction (parallel to the xz plane). The dimensions in the x and z directions are $L_x = 14.14\sigma$ and $L_z = 16.33\sigma$, respectively. L_y is the distance separating the walls (in the y -direction) and varies across different cases, ranging between 3 and 27. Periodic boundary conditions are used along the channel to emulate its perpetual

continuation.

The solid particles of the walls are placed on two (111) fcc lattice planes (see 3.1). This forms closed-group layers that minimize the gaps for liquid atoms to escape. The argon particles are initially placed randomly in the channel. The number of inserted particles is adjusted depending on the volume of the system to realize a constant density of $0.84\rho^*$, where ρ^* is the reduced density. The random positioning of atoms introduces significant overlapping, which can cause problems to the simulation. We resolve this by restricting the motion of each atom to a maximum distance of 0.01σ per time step (see section 3.3.3). This restriction is relaxed after $20000\delta t$.

Instead, we could have placed the liquid atoms on a lattice. This would directly overcome the problem of overlapping. However, in the current model, two lattices would be required: one for the walls and one for the liquid atoms (the wall will obviously have much smaller lattice parameters due to its higher density). Furthermore, the simulation box must be defined to match exactly an integer number of “wall” unit cells. If not, the crystal structure of the walls will break at the periodic boundaries. Therefore, at certain channel widths the separation between the two walls might not exactly fit an integer number of unit cells for the liquid atoms. In such cases the density would be slightly lower.

The regulation of the temperature of the system is achieved solely through the walls by rescaling the velocities of their atoms in each lattice plane [148, 149, 156]. This means that four thermostats are used on the system (two for each of the two walls). The regulation of the liquid temperature is achieved by conducting heat to and from the walls without any artificial adjustments. This method of temperature control is preferred rather than assigning thermostats to the entire system, which can sometimes lead to unrealistic results [158]. The system is brought into thermal equilibrium at a temperature of $0.71T^*$, where T^* is the reduced temperature. This value, with the aforementioned density, corresponds to the liquid state of argon [38, 140]. The state of the system is updated using the micro-canonical (*NVE*) ensemble with a time step of $\delta t \approx 2fs$. After an initial equilibration phase of $10^6\delta t$ the system is sampled for a further $4 \times 10^7\delta t$ to calculate the thermal conductivity.

The thermal conductivity of the liquid is calculated using the Green-Kubo relations (equation 3.3.17) using equation 3.3.19 for the calculation of the microscopic heat flux J . However, here we only focus on λ_x , the thermal conductivity in the x direction (parallel to the walls).

4.3 Validation and Uncertainty

The thermal conductivity of pure argon (i.e. without the walls) was calculated to be $0.130W/mK$ which has a 1.5% error from the experimental value ($0.132W/mK$) under the same conditions [134].

In addition, we want to eliminate methodology-related uncertainty. The first factor to take into account is whether or not the total time of our simulation allows for the convergence of the thermal conductivities. We show this by plotting the output of the Green-Kubo for some of the cases considered (the ones of the following section), as a function of the simulation time. The results show a very good convergence (figure 4.2).

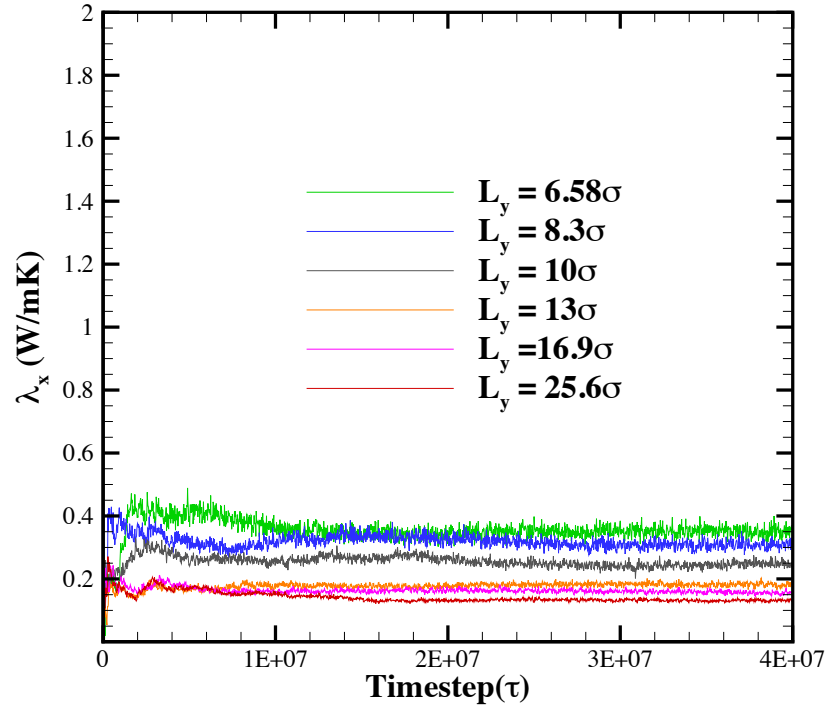


Figure 4.2: Convergence of the thermal conductivity for the various channel widths

The Green-Kubo relation can introduce error when the dimensions of the system are too small (see section 3.3.1). To account for such uncertainties, the thermal conductivity of a channel of width 6.58σ has been calculated for different lengths in the x -direction (the direction in which the thermal conductivity is calculated). The channel lengths considered are 7.07σ , 10σ , 14.6σ , 22.6σ and 42σ . The results fluctuate around a mean value $E(\lambda) = 0.3712\text{W/mK}$ with a standard deviation equal to 0.0142 (figure 4.3). The results show that the first point slightly underestimates the value of the thermal conductivity, deviating by 6.8% from the mean value. The remaining points lie very close to the mean, with a deviation of up to 2.9% for the channel of length 22.6σ . Finally, the value 14.6σ used for this study deviates by only 2.1% . We can generally see that channels beyond 10σ in length are suitable for the calculation of the thermal conductivity.

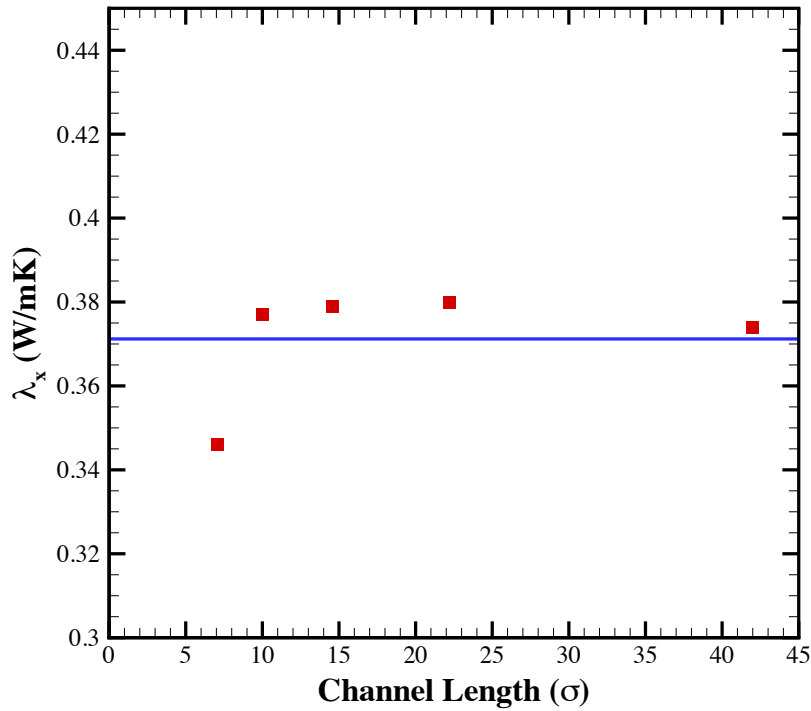


Figure 4.3: Convergence of the thermal conductivity for the various channel widths

4.4 Crystal-like heat transfer of liquids in nanochannels

In this section we study how the simple act of confining a liquid in nanometer-sized characteristic dimensions alters its thermodynamic properties.

The HFACF provides vital information as to how energy fluctuations in the system dissipate. In turn, it illuminates the mechanics of heat transfer within the system. Figure 4.4 plots the HFACF in the longitudinal (x) direction for unrestricted and confined argon (the z direction yields identical results). The results identify a significantly different dissipation pattern of energy perturbations between the two cases. While bulk, unconfined argon presents a sudden, monotonic decay (≈ 400 timesteps) the restricted liquid presents a two-stage decay; one coinciding with its unrestricted counterpart and a second gradual curve extending in time until it finally converges at ≈ 10000 timesteps. As equation 3.3.17 suggests, the larger area under the HFACF of the confined liquid implies a higher thermal conductivity compared to its bulk counterpart.

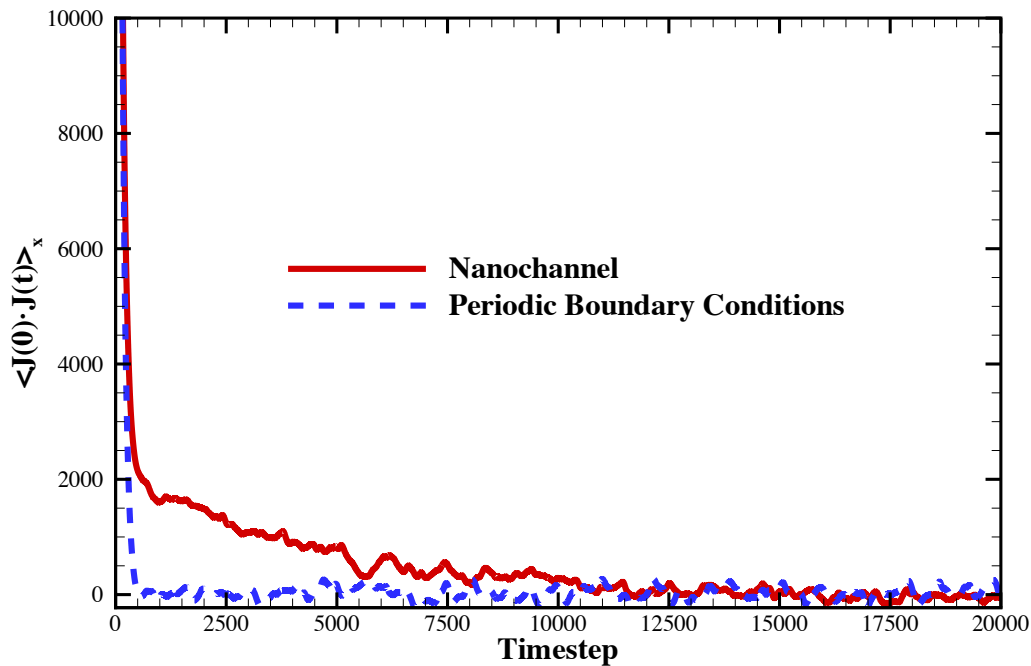


Figure 4.4: HFACF in the x-direction for unrestricted liquid argon (blue) and for liquid argon in a nanochannel (red)

The monotonic nature and short length of decay of bulk argon is the cause of the diffusive nature of heat transfer in liquids. The structural complexity and random collisions of its atoms enable energy transfer between neighbouring atoms over short timescales.

The different trends observed between the two curves suggest a significant change in the thermal behaviour of the liquid. It was speculated that this is due to diffusion arising from the density variations across the channel width. However, as Figure 4.5 suggests, the liquid stratification occurs only in the direction normal to the wall. In the parallel directions, which are those of interest to this study, the density is in fact uniform and hence, no net movement should exist along the channel. Furthermore, studies have suggested that confinement increases the frequency of collisions, inevitably resulting in more efficient energy transfer [155]. This, however, would not significantly prolong the convergence of the HFACF as energy is still transferred mostly between neighbouring atoms; the confined liquid would simply be more correlated at the initial timesteps of the function compared to the unconfined liquid. An analogy is the comparison between two unconfined liquids under different temperatures. The more vibrant atomic motion at higher temperatures will result in the HFACF starting from a greater value. Yet, the correlation length will not differ significantly.

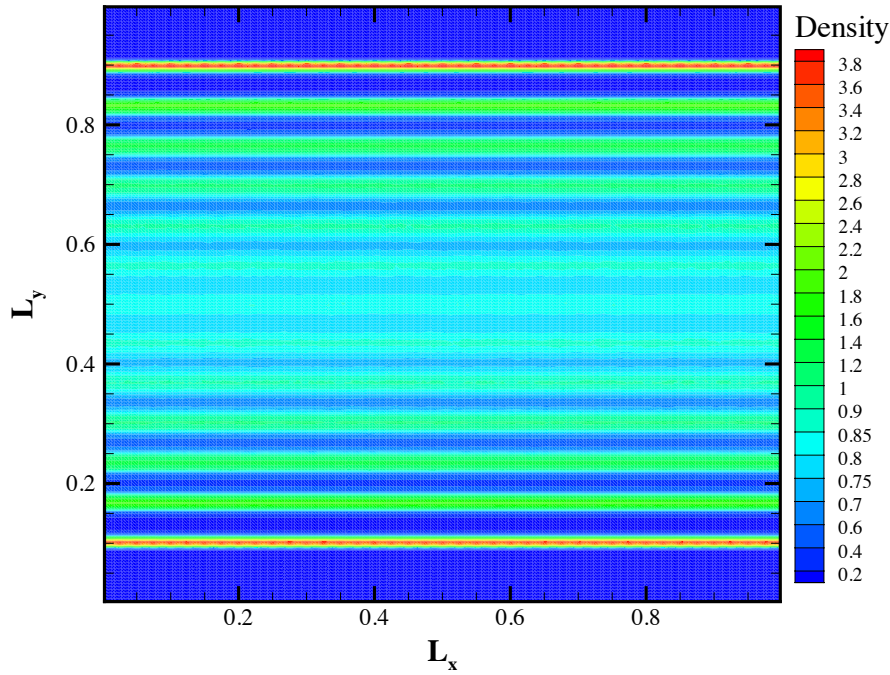


Figure 4.5: Density contours in the xy plane averaged over time

Previous studies have shown that the transition from liquid or amorphous solid to crystal argon is accompanied by the exact same change in the HFACF [135] as that observed between unconfined and confined liquid argon in the present investigation. Similarly, other crystalline materials have shown similar trends [159, 160]. The phenomenon is attributed to the existence of long-range phonons in perfect crystals. The phonons carry energy over longer distances and timescales, causing the HFACF to decay more slowly. In a similar manner, the two-stage decay of the confined liquid is attributed to a significant increase of the phonon mean-free-path compared to bulk liquids. Under confinement, the liquid forms solid-like strata across its width. The imposed structure enables the influence of atomic motion to propagate in a wave-like manner persisting over longer distances. Of course, as a liquid, its atoms still undergo random motion. Hence, the first part of the decay corresponds to the abrupt, stochastic collisions between liquid particles, while the second part corresponds to long-range phonons that propagate unscattered, transferring energy.

In order to parameterise the thermal conductivity of the liquid into its short-range, diffusive and long-range components, a sum of two exponential functions

$$\frac{\langle J(t) \cdot J(0) \rangle}{d} = A_{ac,sh} \exp(-t/\tau_{ac,sh}) + A_{ac,lg} \exp(-t/\tau_{ac,lg}) \quad (4.4.1)$$

was fitted onto the HFACF [80, 135], where the subscripts ac , sh and lg refer to acoustic, short-range and long-range phonons respectively. Studies have suggested that optical

phonons contribute to the short-range portion of the decay[80]. However, the monatomic nature of the fluid in question rules that out[135]. Fig. 4.6 indicates that the fitting captures the curve very well.

In Eq. 4.4.1 the parameters $A_{ac,sh}$, $A_{ac,lg}$ and $\tau_{ac,sh}$, $\tau_{ac,lg}$ are the strengths and time constants of the short and long range phonons respectively and d is the number of dimensions over which the HFACF is calculated. In possession of these parameters, the thermal conductivity can be calculated as [135]

$$\begin{aligned}\lambda_{FIT} &= \frac{1}{k_B V T^2} (A_{ac,sh} \tau_{ac,sh} + A_{ac,lg} \tau_{ac,lg}) \\ &\equiv \lambda_{ac,sh} + \lambda_{ac,lg}\end{aligned}\quad (4.4.2)$$

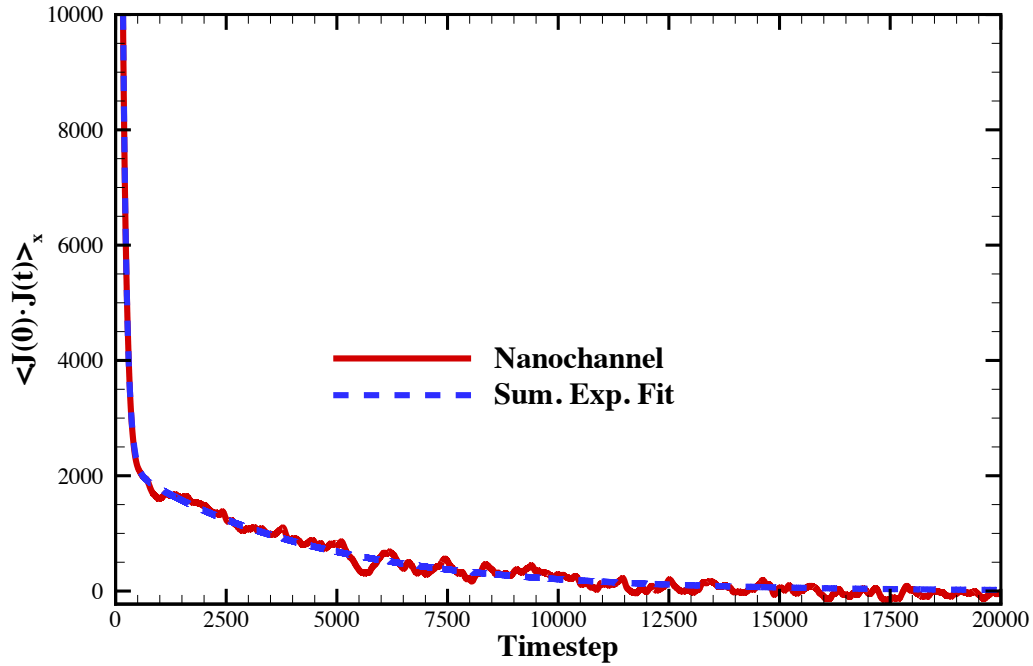


Figure 4.6: HFACF of a liquid in a 6.58σ channel and the sum of two exponential functions fitted onto it

Figure 4.7 plots the thermal conductivity of liquid argon as a function of the wall separation. The four curves correspond to the values obtained directly from the integral of HFACF (green line with circles), from the exponential fit (red line with diamonds) and the individual long range (blue line with triangles) and short-range (black line with squares) effects (as calculated by equation 4.4.2). With the exception of the first point, the direct integral shows an inverse proportional correlation converging to experimental observations of the thermal conductivity of bulk liquid argon under the same temperature [134] ($\approx 0.132W/mK$). The

deviation of the first point is ascribed to all liquid particles being in close proximity to both channel walls, which inevitably affects the liquid structure and motion. This is presented in figure 4.8 using the 1D density profiles across the channel width for channel widths of 3σ , 10σ and 25.6σ . The results show that although the peaks and troughs of the two larger channels coincide, the narrowest channel shows an entirely different oscillation pattern.

The values produced from the exponential fitting form a curve of the same shape. Although the results coincide at the higher wall separations, a difference of up to 8% exists in the lower values. Since the exponential functions overlap with the HFACF almost entirely, the above differences are attributed to noise in the HFACF calculations associated with the long correlation-length accumulation effects [157]. Hence, the smoother curve obtained from the fitting probably reflects a numerically more accurate behaviour than the one obtained from the raw data [161].

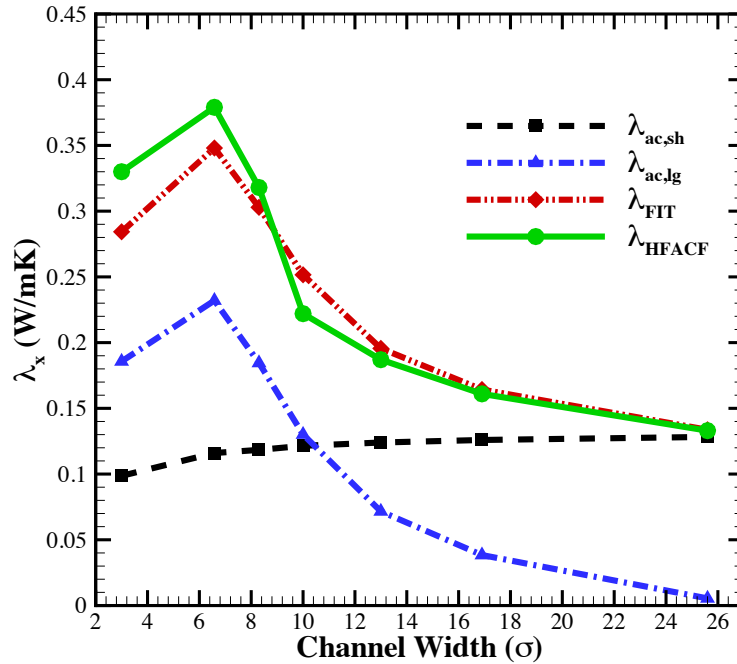


Figure 4.7: The thermal conductivity of the system as a function of the wall separation. The four curves represent the property as obtained by a direct integral of the HFACF (green), by using Eq. 4.4.2 (red), and the individual short (black) and long (blue) range effects

The decomposition of the thermal conductivity into its long and short-range components can shed light on the underlying physical mechanisms of thermal transport in nanochannels. The thermal conductivity attributed to short range phonons, $\lambda_{ac,sh}$, gradually increases for channel widths less than 10σ . This behaviour reflects the inability of the liquid atoms to move and collide freely since for $L_y < 10\sigma$ all argon particles are bounded within discrete dense layers (figure 4.8). This liquid stratification is significantly more

pronounced for the narrowest channel ($L_y = 3\sigma$) than it is for the channel of width 10σ , thus resulting in an increase of thermal diffusion and, therefore, of $\lambda_{ac,sh}$. As the width of the channel increases further ($L_y \geq 10\sigma$), free particles start occupying the centre of the channel and $\lambda_{ac,sh}$ asymptotically converges to the thermal conductivity of bulk argon.

The results of the thermal conductivity associated with the long range phonons, $\lambda_{ac,lg}$, show a trend identical to λ_{EXP} , with a maximum value reached for a nanochannel of width $L_y = 6.58\sigma$. For greater channel widths, both curves start decreasing exponentially. For channel widths smaller than 10σ , the thermal conductivity of the liquid is dominated by long-range phonons. This is shown in figure 4.7 where, within the specified range (i.e. $L_y \leq 10\sigma$), $\lambda_{ac,lg}$ has higher values than $\lambda_{ac,sh}$. At $L_y \approx 10\sigma$ the two curves cross each other, and for channel widths greater than 10σ the long range effects become insignificant in the total thermal conductivity. The value of $\lambda_{ac,lg}$ continues to decrease until it completely vanishes at $L_y = 25.6\sigma$.

The values extracted from HFACF ($A_{ac,sh}$, $A_{ac,lg}$, $\tau_{ac,sh}$ and $\tau_{ac,lg}$) and the derived thermal conductivities (λ_{EXP} , $\lambda_{ac,sh}$ and $\lambda_{ac,lg}$) are averaged values over the entire, non-homogeneous system. This includes density fluctuations near the solid-liquid interface. The mean free path of phonons depends significantly on the density of the medium through which it propagates. Hence, the heat transfer capacity within the channel varies across different regions. This differs from studies on perfect crystals, where the phonon strength and relaxation time reflect intensive properties of the bulk material [80, 135]. The diminishing pattern of the long-range component of heat transfer as the channel width increases, implies that phonons propagate more effectively along the stratified layers of liquid. As the channel becomes wider and the volume fraction of the discrete density layers decays, so does the effect from phonons. However, both longitudinal and transverse phonons are allowed in unconfined liquids [162] and it is therefore expected that, depending on the channel properties, such vibrations can persist in the center of the channel. We have conducted investigations for systems with different liquid densities and operating temperatures, and found that higher-energy phonons are initiated. These can persist in the non-stratified part of the channel, thus allowing their effects to be evident also in significantly bigger channels. These results are shown in the following sections.

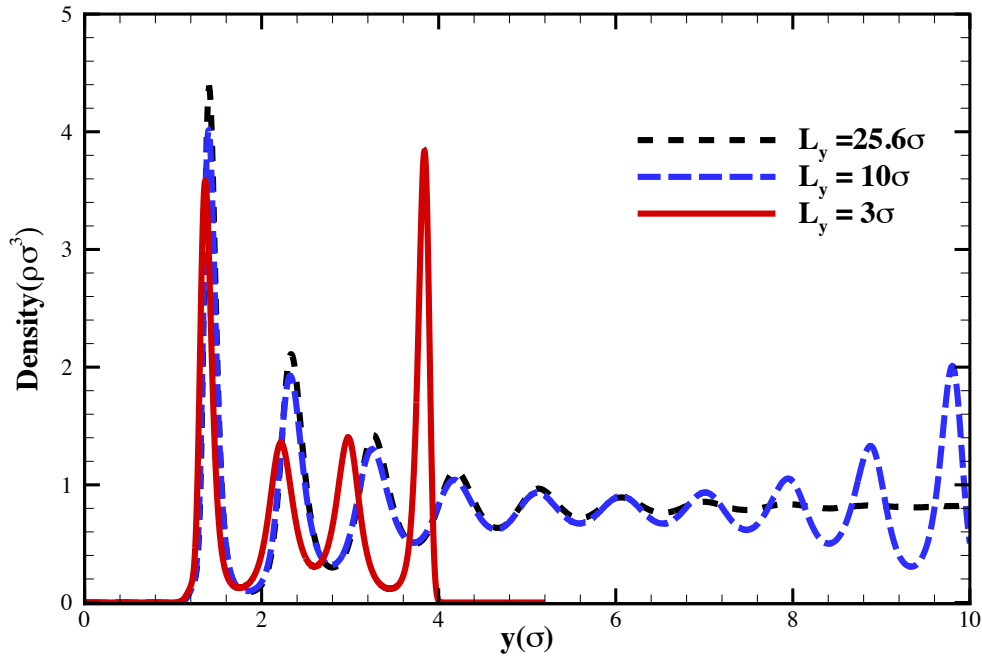


Figure 4.8: Density profiles in the direction of confinement for 3 different wall separations

Although there are no experimental data against which the computational results of this investigation can be verified, MD simulations can be considered as the most accurate simulation approach to investigate the thermodynamic behavior of liquid argon in nanochannels. It is shown that confining the liquid to nanoscale characteristic dimensions can significantly enhance the thermal conductivity, by approximately 2.8 times compared with the unconfined liquid. By observing the dissipation pattern of energy fluctuations in the system this phenomenon is attributed to the existence of long-range phonons, which mostly propagate along the solid-like, structured liquid strata close and parallel to the channel walls. As the channel width increases, the long-range component of the thermal conductivity decays to that of bulk argon. Although experimental verification is still required, we believe that the finding of this study can be used for the design of efficient thermal management tools.

4.5 Parametric analysis

The preceding section has shown that confined and unconfined liquids transfer heat in different ways. To the best of our knowledge this observation is new. Based on other studies on crystal solids, we have presented a framework for decomposing the thermal conductivity into its short-range (normally evident in unrestricted liquids) and long-range effects.

In this section we study how some of the system parameters affect the propagation of phonons and the thermal conductivity. The parameters studied are:

- Strength of interaction between the walls and the liquid.
- Density
- Temperature.

To be accurate with our definitions, when we lower the density of the system we can no longer talk about liquid argon. Instead, in these sections we will often refer to our fluid as a **monatomic liquid**. Of course, we are still assuming atoms of neutral charge which are interacting through London-dispersion forces. Since these tend to be modelled by the Lennard-Jones potential, we also refer to the liquid as a Lennard-Jones fluid.

4.5.1 Solid-Liquid Interactions

In this section we investigate how the strength of the interaction between the solid walls and the liquid affects the thermal conductivity. The range of values used for ε_{wl} is $0.4\varepsilon \leq \varepsilon_{wl} \leq 1.0\varepsilon$.

Figure 4.9 shows the thermal conductivity for a channel width of 6.58σ against ε_{wl} . The four curves correspond to the values as calculated from a direct integral of the HFACF (green); as obtained from the exponential fitting of equation 4.4.1 (red); and the short (black); and long (blue) range components of the equation. Again, the line obtained from the exponential function fits the raw data very well (within 4% error).

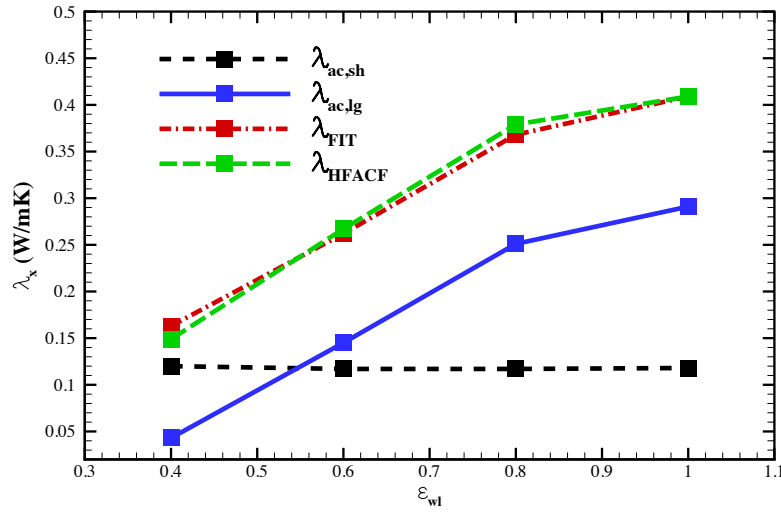


Figure 4.9: The thermal conductivity as a function of the interaction strength between the solid walls and the liquid, ϵ_{wl}

The results show that the total thermal conductivity increases with the strength of the solid-liquid interaction. This is in no way surprising. As ϵ_{wl} decreases, the liquid starts behaving more like its unrestricted counterpart. Therefore we expect that the long-range component of the thermal conductivity would also vanish.

The decomposition of the thermal conductivity into its short and long range components illustrates this more clearly. It is interesting to see that as ϵ_{wl} increases, $\lambda_{ac,sh}$ decreases (albeit very slightly). The increasing interaction results in stronger forces acting on the fluid particles, keeping them tethered to their positions. This in turn reduces the collision frequency between them and the diffusive, short-range component decreases.

The long-range component of the thermal conductivity is the most important when it comes to its dependence on ϵ_{wl} . $\lambda_{ac,lg}$ increases with increasing ϵ_{wl} . As the solid-liquid interaction increases in strength, the liquid atoms become more organised and solid-like. This imposed structure can facilitate the propagation of phonons more effectively.

Summary

To summarise this section, we have studied how the solid-liquid interaction affects the thermal conductivity of confined liquids. When the interaction is weak, the liquid behaves more like its unrestricted counterpart. Therefore, for values of $\epsilon_{wl} < 0.55\epsilon$ the short-range component of the thermal conductivity is dominant. Beyond this value, heat transfer is

mostly dominated by the longer-range effects of phonons.

4.5.2 Density

Here we study how the thermal conductivity varies with a change in the system density. The model employed is identical to the one in the previous section with the exception of the density. We study the system under four densities: $\rho = 0.75\rho^*$, $\rho = 0.78\rho^*$, $\rho = 0.81\rho^*$, $\rho = 0.84\rho^*$.

Fig. 4.10 plots the thermal conductivity, in the x -direction parallel to the wall, of a liquid in a channel of width 8.3σ against the liquid density. The four curves show the values as calculated by a direct integral of the HFACF; the values calculated using Eq. 4.4.2; as well as the short and long range components of the equation. The points obtained from the exponential fitting (λ_{FIT}) are within 5% of the original curve. The diffusive ($\lambda_{ac,sh}$) and long-range ($\lambda_{ac,lg}$) effects of the thermal conductivity are also presented in order to shed light on the synergy of the two thermal transport mechanisms.

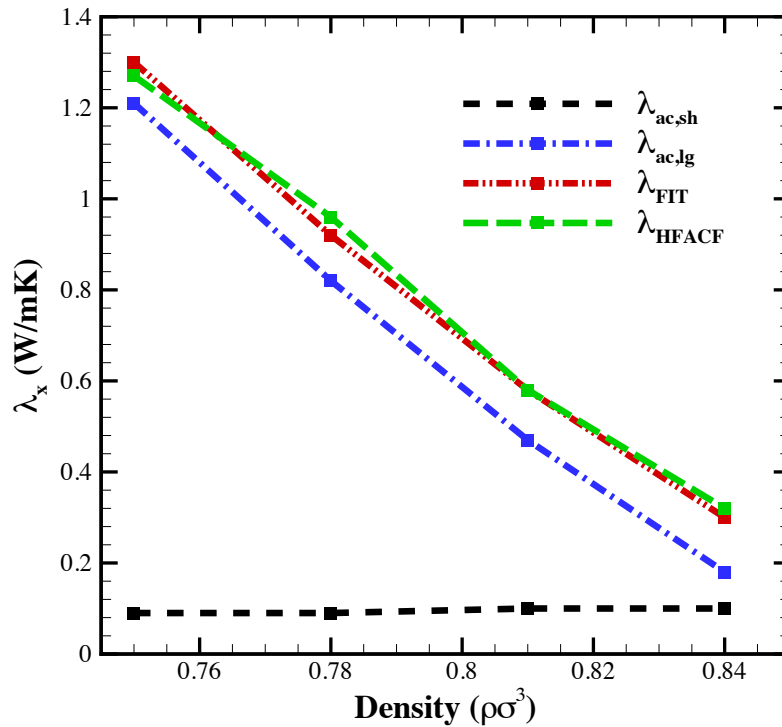


Figure 4.10: Decomposition of the thermal conductivity of a liquid in a channel of 8.3σ as a function of the liquid density.

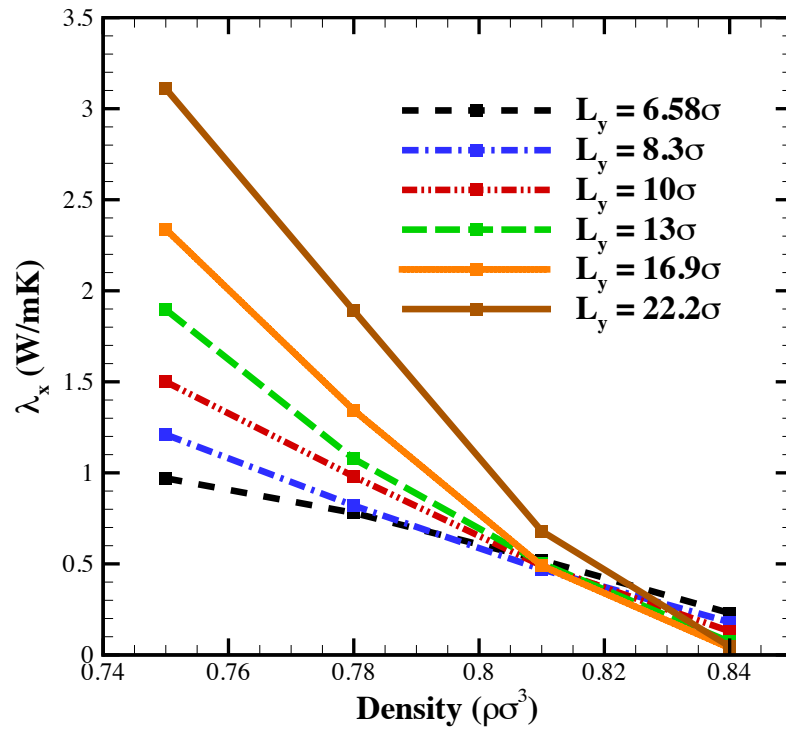
The salient observation of Fig. 4.10 is the inverse correlation between the total thermal conductivity and the liquid density. This behaviour is fascinating as it is in contrast to unrestricted liquids. Under no spatial restriction the increasing density also increases the collision frequency between liquid molecules. This in turn enables a more efficient transfer of energy and therefore a higher thermal conductivity [155, 163]. This conventional understanding of fluids is illustrated by the short-range, diffusive part of the thermal conductivity whose value increases, albeit marginally, as the channel becomes more crammed with liquid particles. The deviation of this component is orders of magnitude smaller than the decrease of the long-range component. Hence, it contributes very little to the total heat conduction. Consequently, the rest of this study will focus on the nature of the long-range phonons propagating parallel to the channel walls.

Figure 4.11a plots the long-range component of the thermal conductivity as a function of the density for various channel wall separations. All curves show the same diminishing behaviour with increasing density. However, the cases for wider channels show significantly higher thermal conductivities at lower liquid densities. As the density increases, the lines intersect and cross each other. Therefore, for higher densities, the narrower channels have slightly higher thermal conductivities. We illustrate this more clearly by plotting the same values of the thermal conductivity as a function of the wall separation distance for different values of the liquid density (figure 4.11b). The results show that the slope of the curve significantly depends on the density. For the highest density value ($\rho^* = 0.84$) we see that the thermal conductivity decays rapidly as the channel width increases (these are the cases shown in the previous section). As the density decreases the gradient of this curve increases. For a value of $\rho^* = 0.81$ the thermal conductivity seems unaffected by the channel width. For $\rho^* = 0.78$ and $\rho^* = 0.75$ the thermal conductivity increases significantly with increasing channel width. In fact, the thermal conductivity triples between the channel of width $L_y = 6.6\sigma$ and $L_y = 22\sigma$.

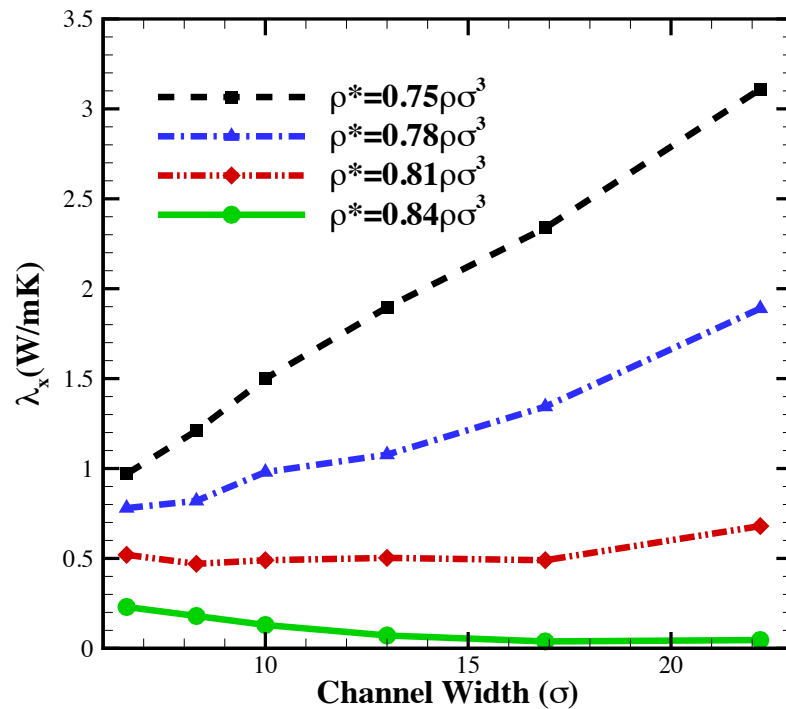
We attribute this inverse correlation between the thermal conductivity and the density to the increased collision frequency. Although in unrestricted liquids it marginally increases the thermal conductivity, here it impairs the vibrational motion of the particles and in turn the long-range phonons discussed in the previous section.

The relationship between the thermal conductivity and the size of the channel is linked to the effect of atomic motion under confinement. As the width of the channel increases, the atoms can move more freely (especially in the direction normal to the wall). At higher densities this translates into a random motion, again increasing thermal diffusion but interfering with the long-range phonons. At lower densities, it manifests itself as vibrations of larger amplitudes, which carry more energy with them. It is, however, surprising to see an increase in λ for widths beyond $L_y = 10\sigma$, as the centre of the channel starts filling up with loose particles. The solid-like liquid layers, which are assumed to be responsible for the propagation of the phonons, occupy a diminishing part of the overall system. This means that phonons can in fact persist even in the centre of the channel.

To further investigate this claim we consider the HFACF in the y direction. As phonons



(a) Thermal conductivity plotted against the liquid density for various wall separations.



(b) Thermal conductivity plotted against the wall separation of the channel for various liquid densities.

Figure 4.11: Thermal conductivities against the density of the liquid (4.11a) and the wall separation of the channel (4.11b).

backscatter across solid-liquid interfaces or density variations the HFACF oscillates about zero. The period of this oscillation is related to the phonon mean free path [34]. Therefore, by comparing the oscillatory pattern of the HFACF in the y direction we can see whether or not phonons persist in larger channels.

Furthermore, in 3D systems, any vibration gives rise to 3 phonon modes: two transverse ones and one longitudinal. Therefore, the behaviour of the HFACF in the y direction is directly linked to the x and z directions. For example, a longitudinal phonon in the y direction is accompanied by two transverse phonons; one in the x direction and one in the z direction.

Figure 4.12 shows the HFACF in the y direction, for liquids of different densities confined in a channel of width 6.58σ . Both the amplitude and period of the curve increase with decreasing density. The larger amplitude indicates more energetic phonons. This is a result of the extra space available for the atoms to oscillate at lower densities. The period (which corresponds to the phonon mean free path) increases due to the smaller number of scattering events at lower densities.

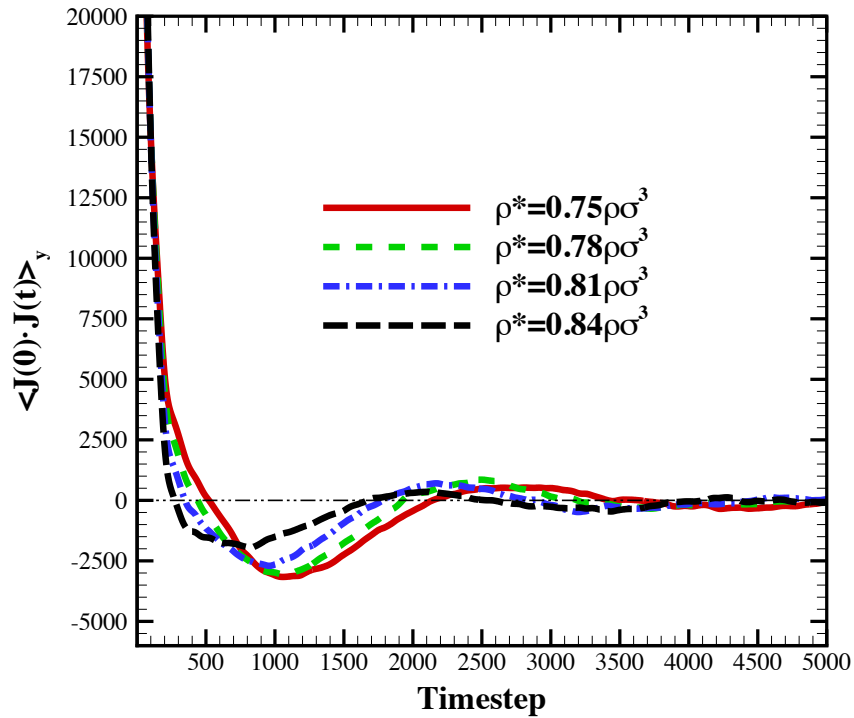


Figure 4.12: HFACF of liquid in a 6.58σ -width channel in the y direction for various densities.

If phonons were only significant in the stratified parts of the liquid, then the period of the HFACF in the y direction should not change with increasing channel width. Phonons

originating from the walls will always scatter after a fixed distance (i.e. same mean free path) corresponding to the width of the stratified part of the channel. Furthermore, as phonons are operating on a smaller percentage of the overall system, the amplitude of oscillation of the HFACF will be smaller. This behaviour can be seen in Fig. 4.13b, for a liquid with $\rho^* = 0.84$. In the narrowest channel where the entire width is stratified, the curve oscillates about zero. As the channel width increases, the stratified part of the channel occupies a smaller percentage of the system. The period of the oscillation remains the same but the amplitude decreases. This indicates that for a liquid with density $\rho^* = 0.84$ phonons are only significant in narrower channels.

For the lowest density $\rho^* = 0.75$ the HFACF in the y direction behaves differently (figure 4.13a). As the channel width increases, both the amplitude and period of the HFACF increase significantly. This is true for channel widths beyond $L_y = 10\sigma$ where the liquid stratification occupies a continuously smaller volume close to the channel walls and liquid distribution increasingly becomes more uniform. This shows that the phonons initiated from the wall can persist beyond the stratified part of the channel.

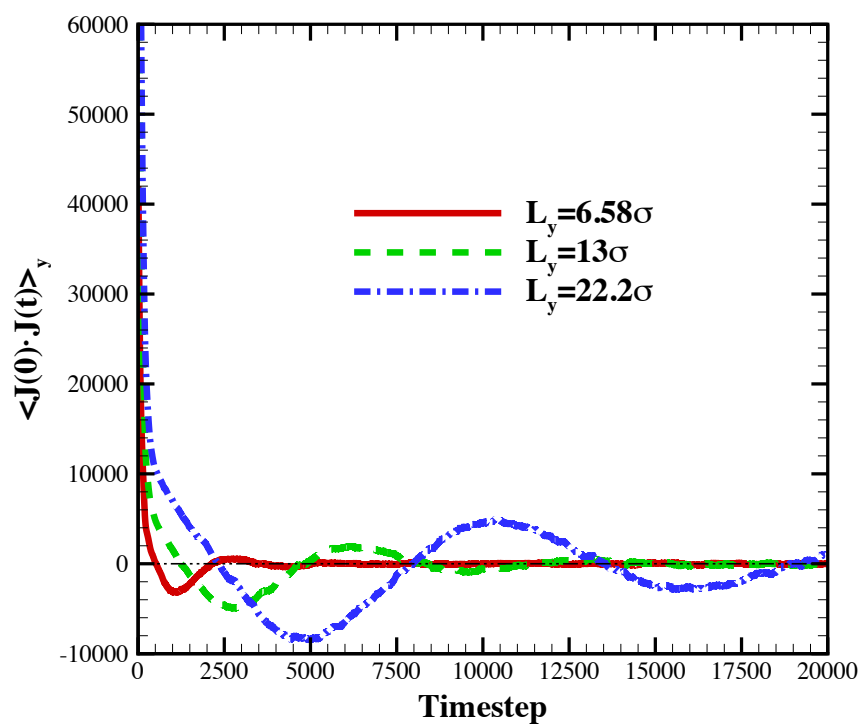
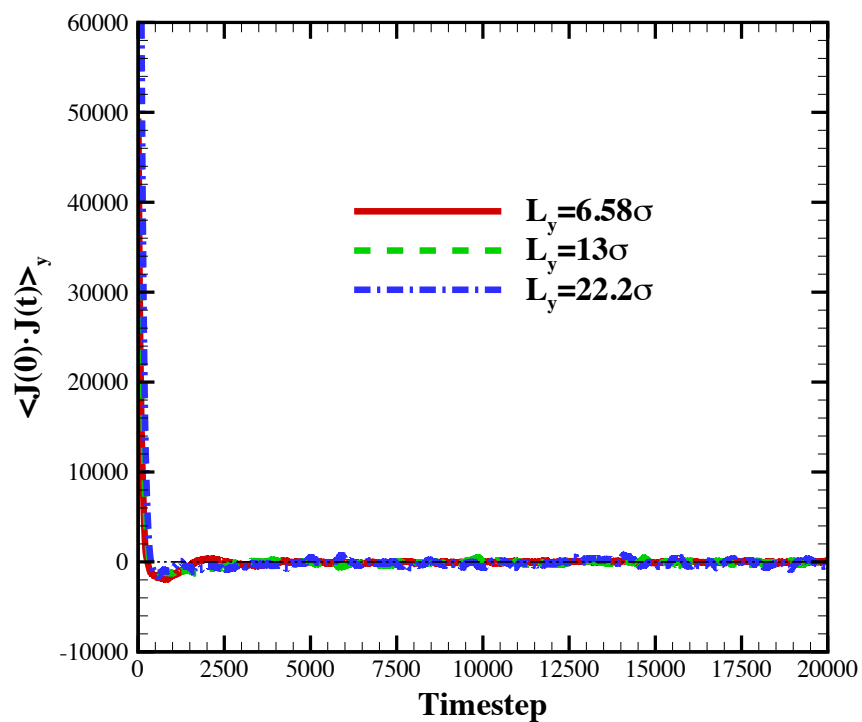
(a) $\rho^* = 0.75\rho\sigma^3$ (b) $\rho^* = 0.84\rho\sigma^3$

Figure 4.13: The HFACF in the y direction for various wall separations for $\rho = 0.75\rho^*$ (4.13a) and $\rho = 0.84\rho^*$ (4.13b)

In this section, we have shown that under certain circumstances, phonons can persist in larger channels. Previous studies have shown that liquids can indeed facilitate both longitudinal and transverse phonons. However, only transverse phonons of frequencies greater than $\frac{1}{t_r}$ exist where t_r is time below which the atomic structure of the liquid remains unaltered [162, 164]. At lower densities t_r is relatively large due to a smaller number of collisions. Therefore, phonons of a wider spectrum of frequencies are transferring energy.

The sensitivity of phonons based on the distribution and structure of particles is not unusual in solids. A good example is graphene. The carbon atoms in graphene can oscillate uninterrupted, enabling high energy phonons to travel uninterrupted over long distances (assuming high quality graphene). Graphite, made out of parallel layers of graphene, has a much lower thermal conductivity (see section 2.3). The reason is that phonons scatter across the parallel graphene planes [165]. Even when measuring the thermal conductivity of graphene experimentally, the material is suspended in order to prevent any scattering on interfaces [166]. In a similar manner, the liquid particles at lower densities have the spatial luxury to oscillate, efficiently carrying energy.

Based on macroscopic intuition, we know that beyond a certain channel width, the thermal conductivity of all densities must eventually diminish to the values of the equivalent unrestricted liquids. Unfortunately, the crippling demand of computational resources by MD does not allow us to explore this limit. This is where mesoscale and hybrid-molecular continuum approaches would be ideal.

Summary

To summarise this section, we have studied how the thermal conductivity of confined liquids is affected by their density. In contrast to unrestricted fluids, the thermal conductivity increases with decreasing density. This is a result of more energetic phonons travelling unscattered over longer distances. We have also found that for lower values of the density, phonons can even persist in larger channels.

4.5.3 Temperature

In this section we study how the thermal conductivity of confined liquids depends on the temperature. The model employed is exactly the same as the above sections, with the density fixed at $\rho = 0.84\rho^*$. The range of temperatures used is $0.71T^* \leq T \leq 1.3T^*$.

Figure 4.14 shows the long-range portion of the thermal conductivity as a function of temperature for various wall separation distances. The results show an exponential correlation between the thermal conductivity and the system temperature. This suggests that phonons of higher energy levels are available at high temperatures.

This behaviour is consistent with the quantum mechanical description of phonons. We have seen that particles classed as fermions, such as electrons, obey the Pauli exclusion principle (see section 3.2.2). However phonons, along with other force carrying particles (e.g. photons), form another class of fundamental particles called **bosons**. An unlimited number of bosons can be in the same state. The average number of such particles in an energy level is given by the famous **Bose-Einstein statistics**. For phonons this is given by

$$\langle n(\omega) \rangle = \frac{1}{\exp\left(\frac{\hbar\omega}{k_B T}\right) - 1} \quad (4.5.1)$$

where $\langle n(\omega) \rangle$ is the average number of phonons with frequency ω (related to the energy by $E = \hbar\omega$); and \hbar . This equation shows that a smaller number of phonons is available for higher frequencies (and therefore energies). However, as the temperature increases, so does the number of phonons occupying these higher energy levels.

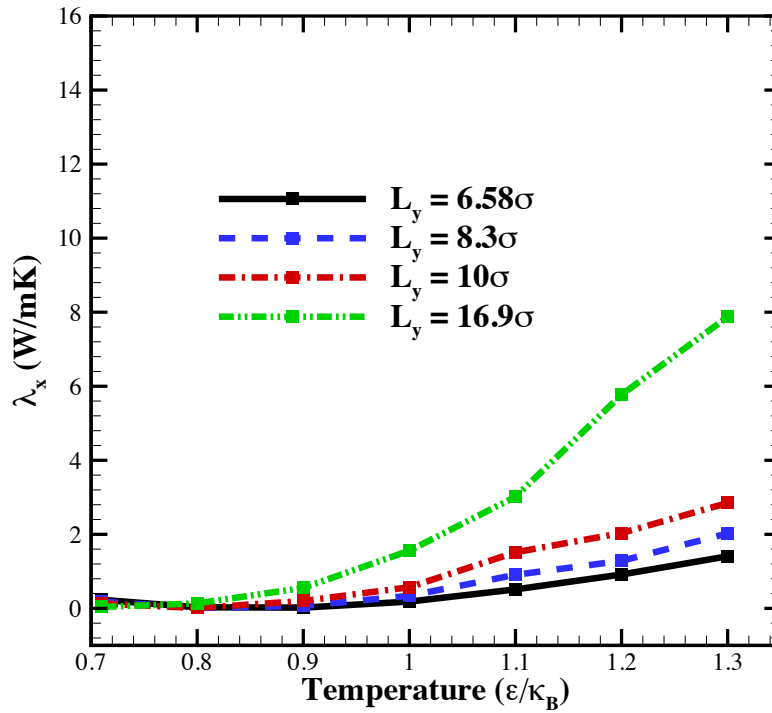


Figure 4.14: Thermal conductivity against the system temperature for 4 different wall separations

For a more classical, intuitive explanation, the higher temperatures enable oscillations of larger amplitude. For a more rigorous explanation, Fig. 4.15 shows the density profiles of the liquid next to the wall for two different system temperatures. It shows that as the temperature increases, the maximum values of the peaks decrease while the width of each profile increases. The size and number of atoms in each system, however, is exactly

the same. Therefore, the density of the system does not differ in any way. The different nature of the two profiles is a product of the different atomic motion. The wider curve for the higher temperature, shows that the atoms perform oscillations of greater amplitudes. Because of that, the probability of finding an atom near the peak decreases. However, it is more likely to find an atom at a distance (corresponding to the amplitude of oscillation) away from the peak. Therefore, the density profile for the higher temperature is wider with a smaller local maximum. The greater the amplitude, the greater the energy accompanied with that oscillation and the more heat is transferred.

As the size of the simulation and liquid properties are identical for the two curves, we deduce that the alterations of the density profiles are a result of an increasing vibrational amplitude. The additional energy through the higher temperature causes a more exaggerated oscillation of the fluid particles, resulting in them spending less time close to their equilibrium positions, giving the profiles a wider shape with lowered local maxima.

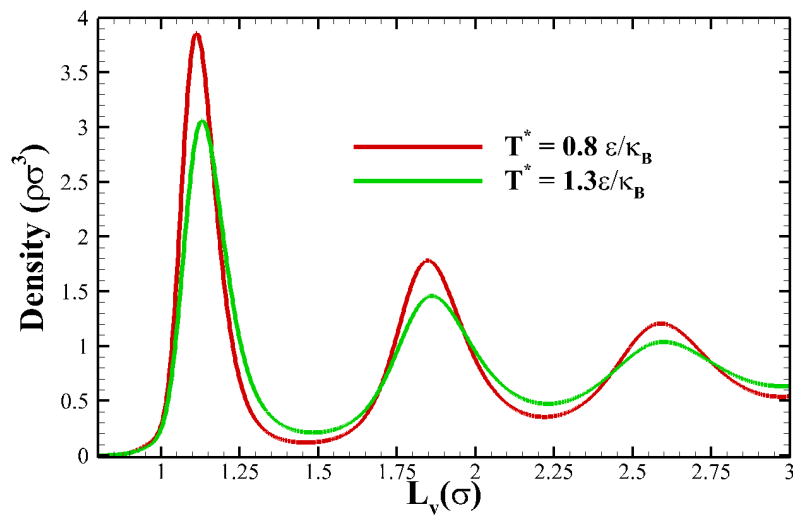


Figure 4.15: Density profiles in the direction of confinement for 2 different system temperatures

The thermal conductivity of unrestricted liquids is also enhanced (very slightly) with an increasing temperature. As the temperature increases, the atoms become much more energetic and their motion more chaotic. The diffusion and frequency of collision increases. In turn, energy is transferred more efficiently. This is obviously different to the case of confined liquids. The spatial restriction converts the stochastic atomic motion into a structured oscillations of larger amplitudes, which carry much larger amounts of energy.

Summary

To summarise this section, we have studied how the thermal conductivity of confined liquids behaves as a function of temperature. The results show an increasing pattern which is attributed to a larger number of high energy phonons available in the system. This is in agreement with the Bose-Einstein statistics. Furthermore, the density profiles show that at higher temperatures the atoms perform oscillations of greater amplitude.

4.6 Conclusions

In this section we have studied how confinement affects the thermal conductivity of a Lennard-Jones fluid. The main findings are listed as follows

- Simply restricting a monatomic liquid, increases its thermal conductivity significantly.
- The strength of the interaction between the liquid and channel walls influences the heat conductance of the system. For weak interactions the thermal conductivity is dominated by the short-range diffusive component. This is similar to unrestricted liquids. As the interaction becomes stronger the thermal conductivity increases and is mostly dominated by long-range phonons
- The liquid density has significant effects on the thermal conductivity of the liquid. As the density decreases the thermal conductivity is significantly enhanced. This is in contrast to unrestricted liquids. The behaviour is attributed to a smaller number of scattering events as the channel is less “cluttered” at lower densities.
- For lower values of the liquid density, phonons persist even in the center of the channel where no stratification occurs. Under such conditions the thermal conductivity is enhanced even in larger channel widths.
- For higher system temperatures, phonons of higher energy are available, which enhance the thermal conductivity of the liquid.

Generally, we have found that the long-range component of the thermal conductivity in confined liquids is very sensitive. More so than solids, the motion of liquid atoms is susceptible to many parameters. These can compromise their vibrational motion by increasing the frequency of scattering events. It is therefore of practical importance to understand under which conditions such effects can be harnessed for more effective heat transfer.

The results obtained here involve a system with no fluid flow. It remains an open question as to whether such effects are still significant under flow conditions. We expect that

high velocities will interfere with these delicate lattice vibrations causing the aforementioned thermal conductivity enhancements to vanish. However, we believe that under low velocity laminar flows, such effects will still play a major role in the heat transfer capacity of the system. For example, future heat exchangers might be focused on liquids flowing through wicks under capillary forces.

Furthermore, our studies involve monatomic liquids which interact via weak London dispersion forces. Other liquids, such as water, have molecules that are more tightly bound to each other (see section 3.2.1). Therefore, one would expect that under confinement, the thermal conductivity will significantly increase. Previous studies have indeed shown that the thermal conductivity of water increases under confinement (although the mechanism of heat transfer was not studied) [155]. However, the confining solid in these studies is a SWNT. Carbon-based materials are hydrophobic which, based on our results, suppress the propagation of phonons.

We believe that an appropriate selection of the operating liquid and the material of the channel can have a major effect on the thermal conductivity of the system. Here, we have provided a framework providing design considerations to improve the thermal conductance of thermal management devices. Of course there are many steps between this theoretical study and the practical application of the presented findings. These will be discussed in the concluding chapter.

Thermal Behaviour of Confined Nanofluids

During the review of the literature (see section 2.4) we have discussed the fact that nanofluids exhibit thermal conductivities often beyond the predictions of theoretical models. There are a number of MD studies of the thermodynamic properties of nanofluids, providing various explanations of the observed enhancement [34, 140, 167, 168].

Here, we study the thermal conductivity of these suspensions under spatial restrictions. This area has received very little attention. However, the vision of nanofluids as cooling liquids in micro and nanochannel heat sinks renders such investigations crucial. The systems studied here involve very narrow channels (up to 10σ in channel width) with a single particle located at the centre. Under flow conditions, clogging and abrasion might become serious problems for such systems. However, we believe that the findings presented here can shed light on the behaviour of nanofluids in larger channels (i.e. microchannels).

In this chapter we consider two nanofluids:

- Copper-argon nanofluids, confined in idealised walls. This is a model very similar to those employed for pure liquids (4) with the addition of the nanoparticle
- Copper-Water nanofluid confined in smooth, graphene-based walls.

As we mentioned in the introductory chapter, the results shown here were obtained before those of chapter 4. In fact, it is the results of section 5.2 which compelled us to study confined liquids without the nanoparticle. Although this section has been extended to accommodate the results of chapter 4, the sections to follow are not a continuation of the preceding chapter. It is a future endeavour to study exactly how the addition of the particle affects the lattice vibrations of chapter 4.

5.1 Thermal Conductivity of copper-argon Nanofluids in Nano-channels

In this section we study a nanofluid consists of a copper particle suspended in liquid argon. The suspension is confined in a channel of idealised solid walls. The goal is to study how its thermal conductivity changes with increasing volume fraction and decreasing channel width.

5.1.1 Computational Model

The computational model consists of argon atoms confined in a channel of nanometer characteristic dimensions, as well as a copper particle suspended in the centre of the system. The model is almost identical to those used in chapter 4. The main difference is that a sphere of liquid atoms was scooped from the center of the channel and was replaced by copper atoms (figure 5.1). These have mass $m = 1.6m^*$ (i.e. 1.6 times that of the atomic mass of liquid argon).

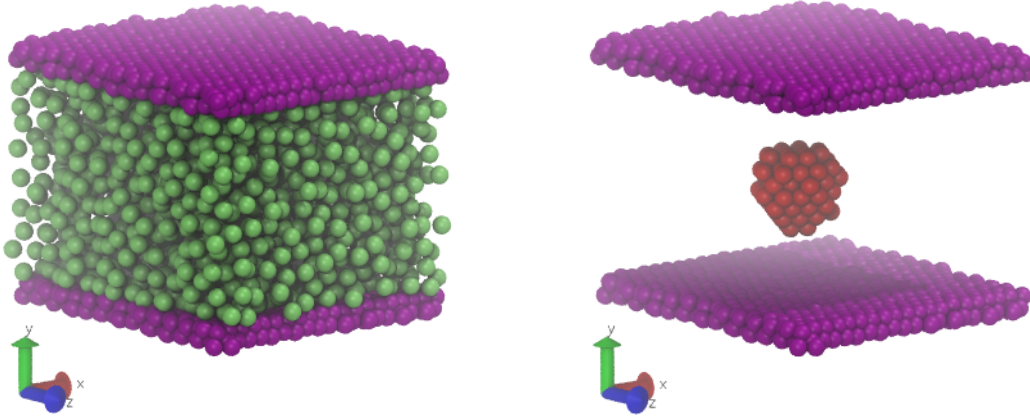


Figure 5.1: Schematic representation of the MD model of a copper-argon nanofluid confined within two idealized walls. On the right hand image the argon particles are made transparent

All interactions are modelled through a Lennard-Jones (LJ) potential (equation 3.2.3). For computational efficiency, interatomic interactions beyond a cut-off distance $r_c = 2.2\sigma$ are disregarded. The LJ parameters for the potential between argon particles are $\epsilon_{ll} = 1.0\epsilon$ and $\sigma_{ll} = 1.0\sigma$, while for the wall-argon interactions the values $\epsilon_{wl} = 0.6\epsilon$ and $\sigma_{wl} = 0.75\sigma$ are used (same as before). For the copper particle the parameters $\epsilon_p = 39.676\epsilon$ and $\sigma_p = 0.738\sigma$ are used. For the particle-argon interaction we use the Lorentz-Berthelot mixing rule (equations 3.2.4 and 3.2.5). The resulting LJ parameters are $\epsilon_{pl} = 6.3\epsilon$ and $\sigma_{pl} = 0.8693\sigma$. Finally, for the wall-particle interactions, the values $\epsilon_{wp} = 39.0\epsilon$ and

$\sigma_{wp} = 0.85\sigma$ are employed. The number of argon atoms varies with the channel width, while retaining a constant density $\rho_i^* = 0.84m\sigma^{-3}$ and temperature $T^* = 0.7\epsilon k_B^{-1}$.

The simulation timestep is $\delta t \approx 2fs$. An initial equilibration phase of 2×10^6 timesteps is performed to allow the temperature and energy of the system to settle. The simulations are then performed for a further 2×10^7 timesteps and the positions at each timestep are taken from the microcanonical ensemble (*NVE*). For the calculation of HFACF, a correlation length of 2×10^5 timesteps is used, which gives the autocorrelation function sufficient time to decay.

5.1.2 Results and Discussion

The thermal conductivity has been calculated for channels of various widths. The radius of the particle remains fixed. Therefore, the increasing channel width results in a decrease in the volume fraction of the solid particle.

Figure 5.2 shows the calculated thermal conductivities as a function of the channel width. As the channel size increases, the volume fraction of particles in the system decreases. With the exception of the first point (in which the particle is less than 3σ away from the walls of the channel), a linear relationship governs the thermal conductivity with the channel width:

$$y = -0.0009x + 0.167 \quad (5.1.1)$$

The thermal conductivity of pure argon (red curve) shows an entirely different pattern to that for the nanofluid. It is lower for narrow channels and slightly increases with increasing channel width. Hence, in this case, the enhanced thermal conductivity in narrower channels is related to the nanoparticle and not to the effect of confinement on any (pure) liquid.

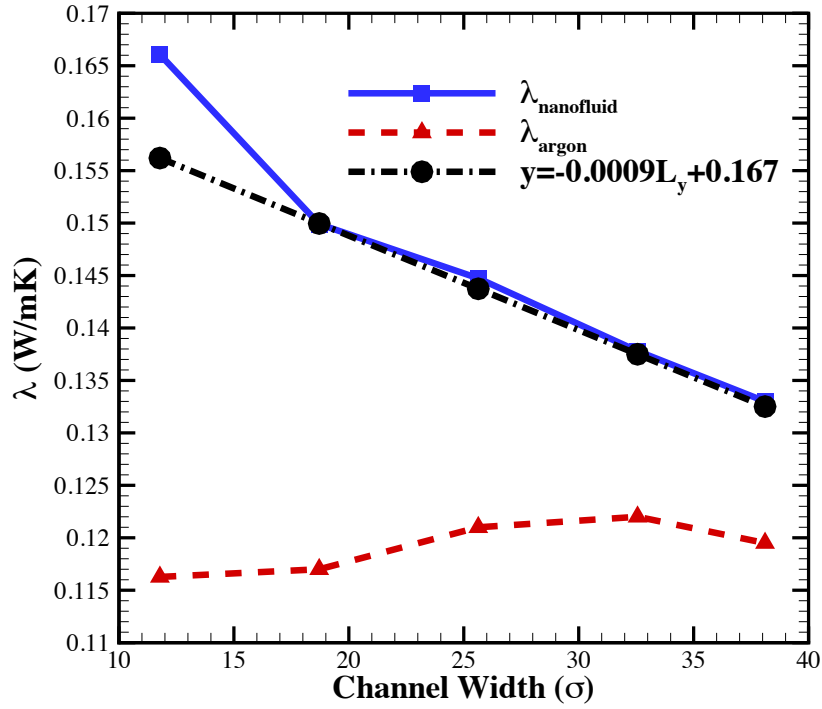


Figure 5.2: Thermal conductivity of the nanofluid (blue) and pure argon (red) as a function of the channel width. The black line is obtained through regression of all but the first point of the thermal conductivity of the nanofluid

We briefly digress to explain the differences between the relationship of the thermal conductivity and channel width found in this section (figure 5.2) with the behaviour described in chapter 4 (see figures 4.7 and 4.11b). Firstly, the solid-liquid interaction used in this section ($\epsilon_{wl} = 0.6\epsilon$) is lower than the majority of the studies in the preceding chapter ($\epsilon_{wl} = 0.8\epsilon$). We have shown that this significantly lowers the long-range effects of the thermal conductivity (see figure 4.9). Furthermore, the values of the channel width considered here are greater than 10σ . According to our results, for the same density ($\rho = 0.84\rho^*$), the long range effects decay rapidly at channel widths $L_y \geq 10\sigma$ (see figure 4.7). Finally, in this section we calculate the total thermal conductivity and not only the components in the parallel directions. The conductivity in the direction normal to the wall is known to be impaired under such severe confinement [155]. This is also evident from the HFACF in the normal direction (see figure 4.13b). The curves take negative values due to the backscattering of phonons rather than extending and gradually decaying as in the x and z directions [34]. This anisotropy is further discussed for nanofluids later in this section.

Figure 5.3 plots the same thermal conductivities as a function of the particle loading. The values predicted by the classical model (equation 2.4.1) are also plotted. As the volume

fraction increases, the MD results predict significantly higher thermal conductivities, while as the particle loading approaches zero the two converge close to $\approx 0.132\text{W/mK}$, which is the thermal conductivity of liquid argon at temperature $0.71k_B/\epsilon$ [134].

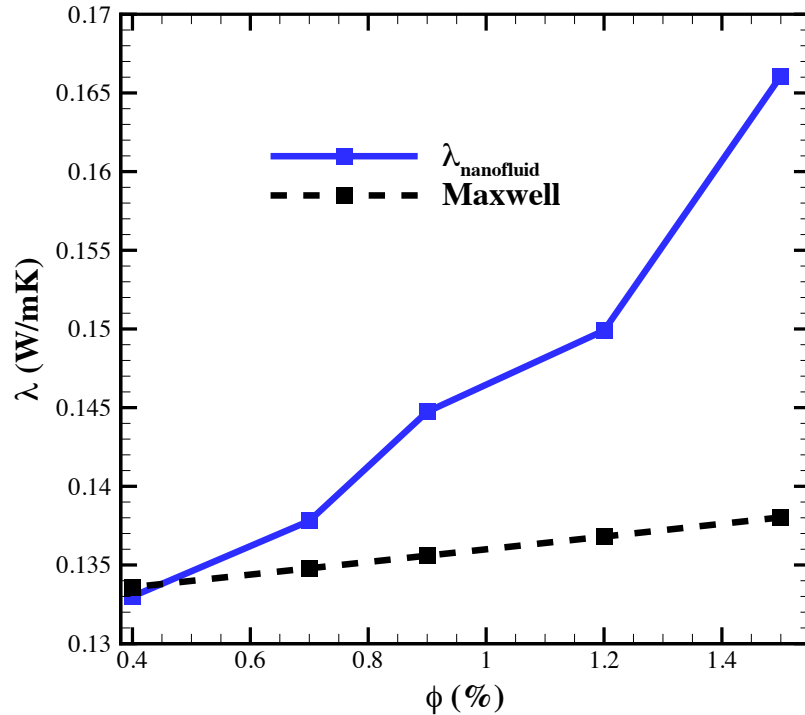


Figure 5.3: Thermal conductivity of the nanofluid as a function of the volume fraction

The radial distribution function (RDF) in figure 5.4 shows the nature of the liquid distribution around the nanoparticle. As the channel width increases, the density of the nanolayer around the particle decreases, with the density differences being larger between the layers 10 and 17 (figure 5.4).

The density profiles of the argon atoms close to the channel walls are shown in figure 5.5. In contrast to the particle nano-layer which decreases in density with increasing channel size, the local maxima of the layers close to the wall seem to increase. The two phenomena are not independent. For small channel widths, the particle pulls argon atoms away from the liquid layers close to the wall. This lowers the maxima of the density profiles.

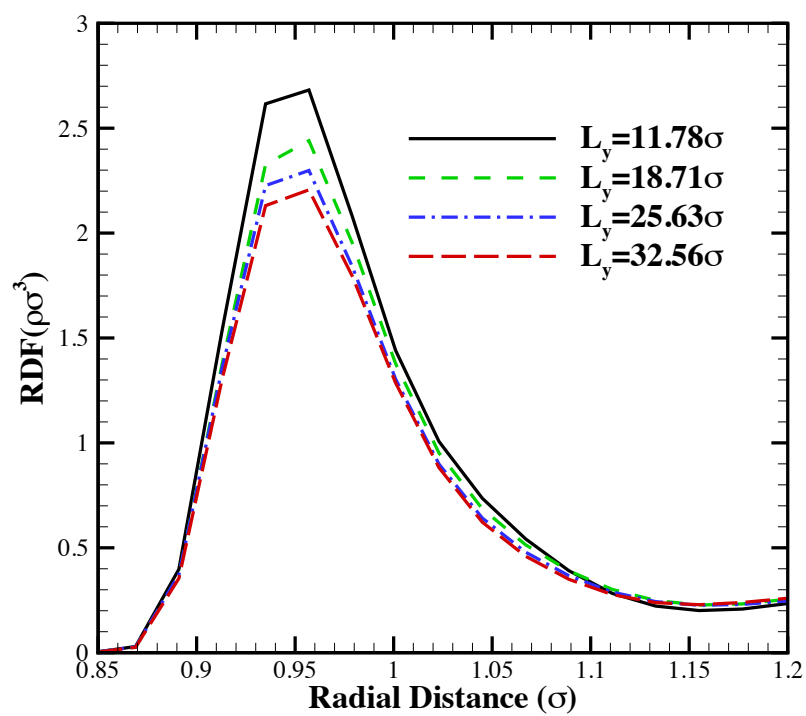


Figure 5.4: Radial distribution function of the liquid around the nanoparticle

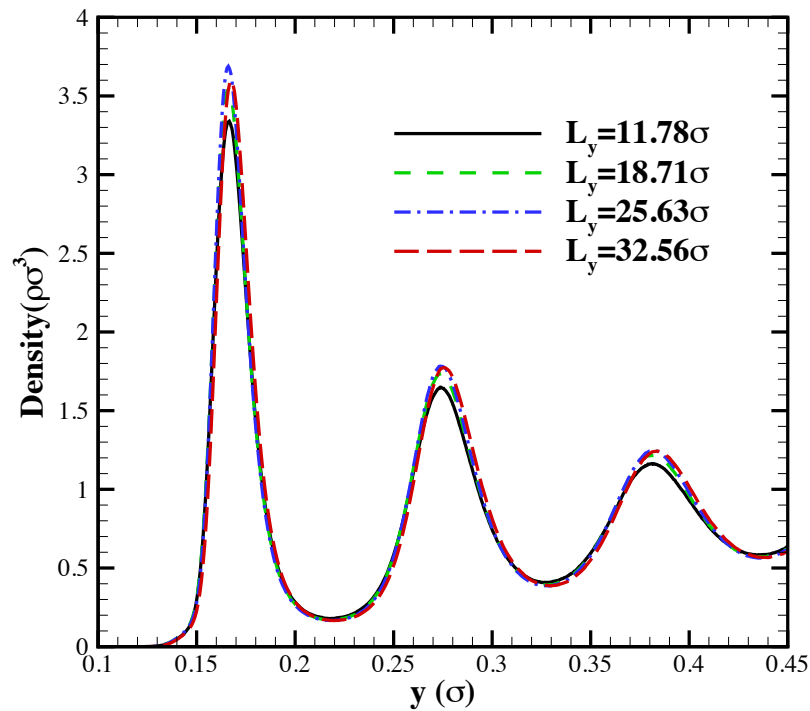


Figure 5.5: Density profiles of the liquid close to the channel wall

We also investigate the anisotropic behaviour of thermal conductivity with respect to the x , y (normal to the walls) and z direction. The thermal conductivity in the y direction increases when increasing the channel width and gradually reaches a plateau (figure 5.6). This is the opposite of the behaviour of thermal conductivity in the directions parallel to the channel walls (figure 5.2). The anisotropy in the y direction is attributed to the lower collision frequencies between the argon atoms, near the wall, which results in a less efficient transfer of energy. Past papers have confirmed a similar behaviour in pure liquids (with no nano-particles) [155, 169]. The slight deviation of the results from the plateau for the largest channel width (figure 5.2) is due to fluctuations arising from the Green-Kubo approach.

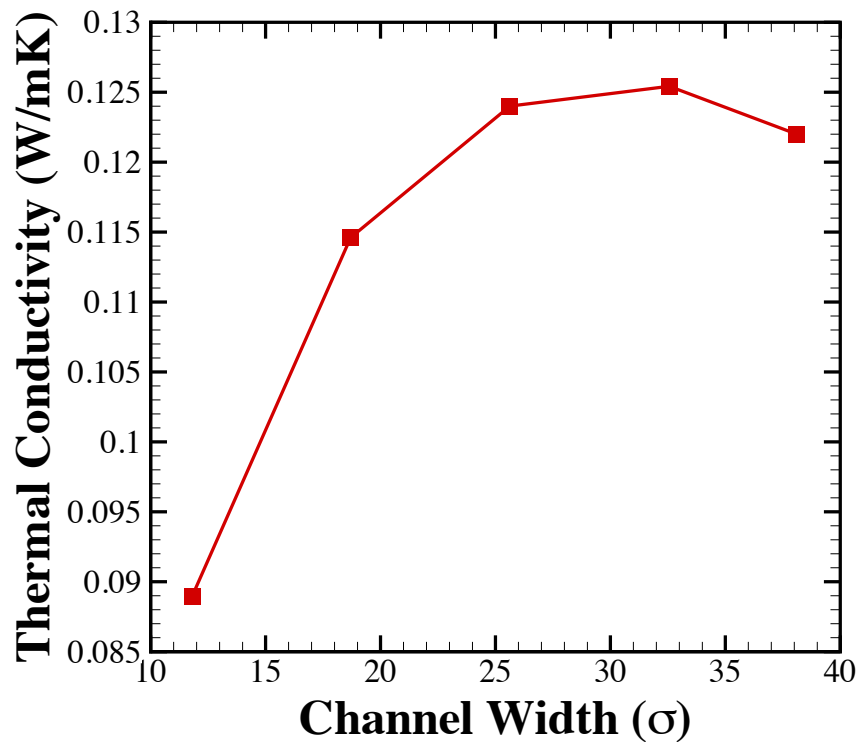
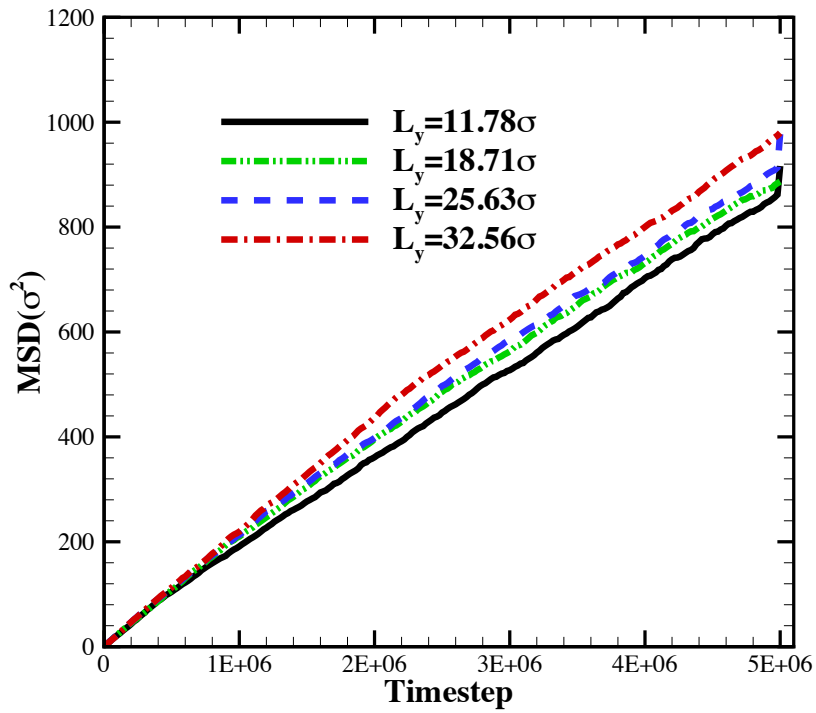
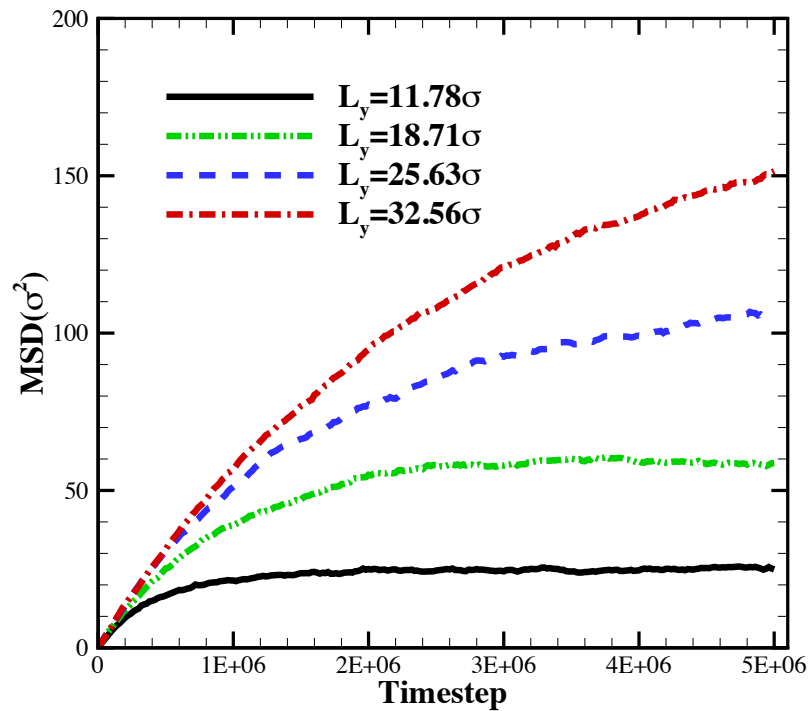


Figure 5.6: Thermal conductivity of nanofluid in the y direction as a function of the channel width

The anisotropic behaviour in the direction normal to the walls is also reflected in the Mean Square Displacement (MSD) for different channel widths (figure 5.7b). Although the MSD is considered to provide uncertain results for the diffusion coefficient in confined fluids, it clearly shows here, in a qualitative manner, the anisotropy in the y direction, where the MSD curves reach a plateau for different channel widths.



(a) MSD of nanofluid



(b) MSD of nanofluid in the direction normal to the channel walls

Figure 5.7: Total MSD (5.7a) and its component in the normal direction (5.7b directions)

5.1.3 Summary

To summarise this section, we have studied the thermal conductivity of an argon-copper nanofluid confined in a nanochannel. The results reveal that, in addition to the increasing volume fraction, confinement can also enhance the thermal conductivity of the nanofluid. Furthermore, an investigation of the liquid distribution shows that this is due to the organised liquid structures forming around the nanoparticle. From small channel widths, the density and thickness of these nanolayers increases significantly. This order imposed on the system is responsible for the enhancement of the thermal conductivity. Finally, the anisotropic behaviour of nanofluids was investigated, showing that the thermal conductivity in the direction normal to the walls increases when increasing the channel width. This behaviour deviates from the results for total thermal conductivity. It is a product of the impaired atomic motion in the normal direction due to the severe spatial restriction, which lowers the efficiency of heat transfer.

5.2 Water-Copper

In this section we study a nanofluid composed of a copper particle suspended in liquid water. The nanofluid is confined in a nanochannel made of graphene walls. We investigate how the thermal conductivity changes with increasing volume fraction, for various channel widths.

5.2.1 Computational Model

The computational model consists of water molecules confined in a channel of nanometer characteristic dimensions. The walls of the channel are fixed perpendicular to the z direction (parallel to the xy plane). This might be slightly confusing as in all other studies the channels were perpendicular to the y direction (the change is related to implementation details in LAMMPS). L_z , the distance separating the walls (in the z direction), is a parameter of interest to this study and is therefore varied across different cases. Periodic boundary conditions are used along the x and y direction, emulating the perpetual continuation of the channel. In the z direction, the boundaries coincide with the walls and fixed boundary conditions are used.

Each set of walls consists of two graphene planes. In each plane, the carbon atoms are arranged in a hexagonal tessellation (see section 3.1). The length of the sides of these hexagons is $1.42\overset{\circ}{\text{A}}$. The carbon atoms are tethered to their initial lattice positions via spring potentials with $\kappa = 500$.

Interactions between carbon atoms are modelled using LJ potentials with $\epsilon = 0.0684$

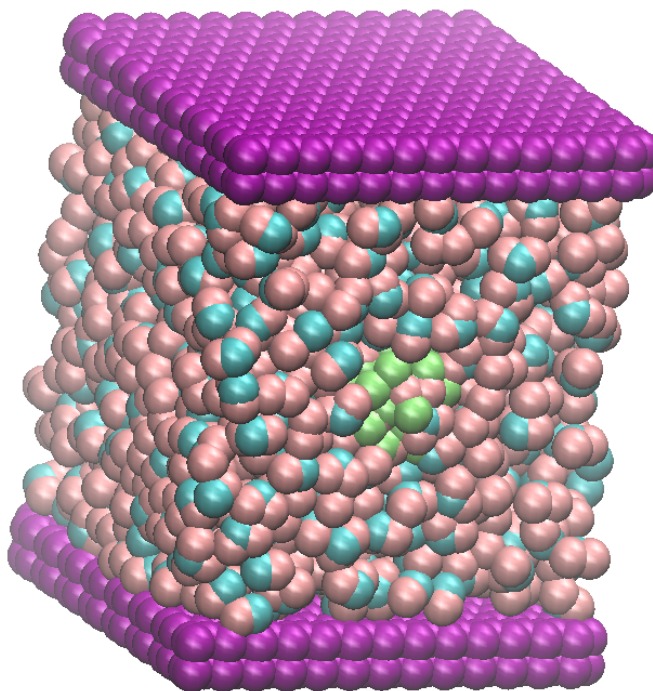


Figure 5.8: Schematic representation of atomistic model. The oxygen (light blue) and hydrogen (light pink) make up the water molecule. The copper nanoparticle (green) can be seen slightly protruding in the centre

and $\sigma = 3.407\text{\AA}$ [170].

Generally 4-site models are more accurate. However, here we use the SPC/Fw model [14] for its simplicity. Furthermore this model accurately portrays the behaviour of water under the conditions considered here (i.e. room temperature). The intermolecular interactions are given by equation 3.2.8. Intramolecular degrees of freedom are modelled using equation 3.2.9. The parameters for the SPC/Fw are given in table 3.3.

The graphene walls, the water molecules and the copper particle interact through a Lennard-Jones potential (equation 3.2.3). The parameters are calculated using the Lorentz-Berthelot mixing rules (equations 3.2.4 and 3.2.5) and are given in table 5.1

The simulation step used is $\delta t = 1\text{fs}$. After an initial equilibration phase of $130,000\text{fs}$ the simulations are performed for a further $10 \times 10^6\text{fs}$. The state of the walls is updated according to the microcanonical (NVE) ensemble whereas the positions and momenta of the nanofluid atoms are taken from the canonical ensemble(NVT). For the calculation of the HFACF a correlation length of $2 \times 10^3\text{fs}$ is used.

Atoms	$\epsilon(Kcal/mole)$	$\sigma(\text{\AA})$
C - C	0.0684	3.407
C - O	0.3920	3.19
C - H	0	3.82
Cu - C	0.8096	2.838
Cu - H	0.2720	1.625
C - O	1.1981	2.693
Cu - Cu	9.57	2.270

Table 5.1: Lennard Jones parameters between atoms of the system. C represent the carbon atoms of the graphene walls, H and O represent the hydrogen and oxygen atoms of the water molecules and Cu refers to the copper atoms that constitute the nanoparticle

5.2.2 Results and Discussion

Figure 5.9 shows the calculated thermal conductivities as a function of the volume fraction ϕ for various channel widths. The nature of the curves, parabolic rather than the linear behaviour predicted by the classical effective medium theory based models, is similar to previous investigations that studied unrestricted nanofluids [140].

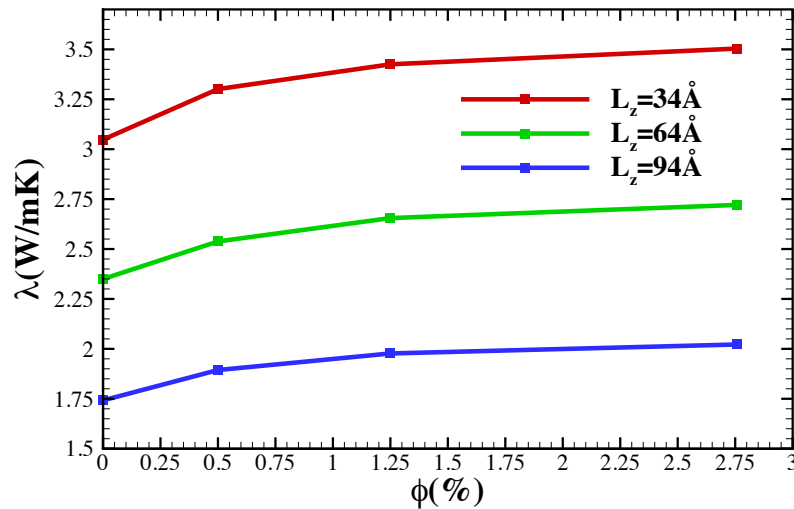


Figure 5.9: Thermal conductivity of the nanofluid as a function of the volume fraction for 3 different wall separations.

Although all curves have the same shape, they are separated by an offset. The narrower channels have significantly higher thermal conductivity. Figure 5.10 shows the same results against the wall separation distance. All curves present a diminishing pattern as the channel width increases. This is true even in the absence of a particle (i.e. 0% volume frac-

tion). In the narrowest channel, the thermal conductivity of pure water is $\approx 3.048\text{W/mK}$; approximately five times that of bulk water ($\approx 0.6\text{W/mK}$). This should come as no surprise following the previous chapter (chapter 4). However, our goal here is to study how the thermal conductivity is enhanced as a direct result of the particle loading.

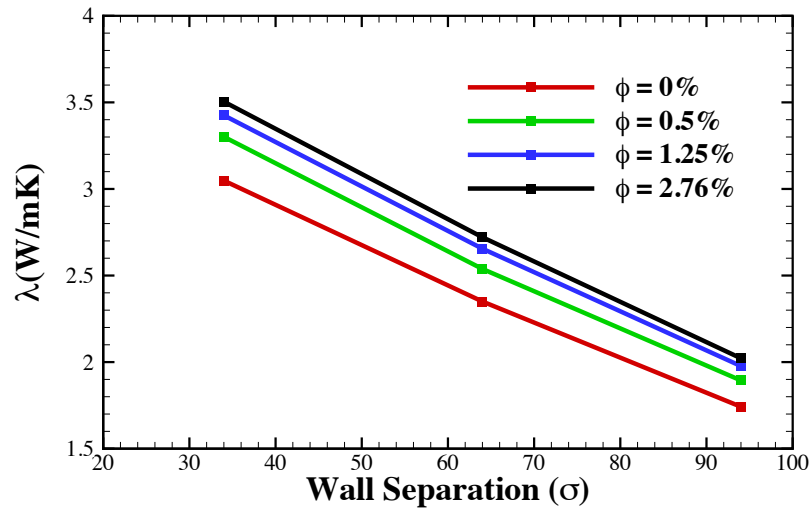


Figure 5.10: Thermal conductivity of nanofluid as a function of the wall separation for 4 different volume fractions.

To find the enhancement against the particle loading we normalise the thermal conductivities by the value of pure water in the same channel (figure 5.11). At low volume fractions, the enhancements seem to coincide for all channel widths. However, as the volume fraction increases, enhancement is greater for the wider channels. For a particle concentration $\phi = 2.75\%$, there is a 10% increase in the thermal conductivity of the base liquid of the 94\AA -width channel compared to that of width 34\AA .

So far we have shown that, although the absolute thermal conductivity increases with decreasing channel width, at least part of this enhancement is independent of the particle. On the contrary, in narrower channels an increasing volume fraction results in a smaller increase in the thermal conductivity. To explore the origins of this behaviour, the structure of the liquid particles is analysed. Figure 5.12 shows the density profiles of two channels with different wall separation distances for pure water and a nanofluid with particle loading $\phi = 2.76\%$. In both cases the addition of the particle pulls the density layers close to the wall towards the centre of the channel. However, in the channel with smaller width, the particle is closer to the walls. Its effect on the liquid stratification is therefore much greater. In turn this completely disfigures the density profiles, in comparison to those with pure water (figure 5.12a). In fact, the oscillatory nature of the profiles is almost entirely flattened. (As shown in the offset of figure 5.12a, there is a lack of symmetry between the profiles close to the two walls. This indicates that the particle has spent most of its time closer to the upper wall, which is why the profiles on the right hand side are more distorted)

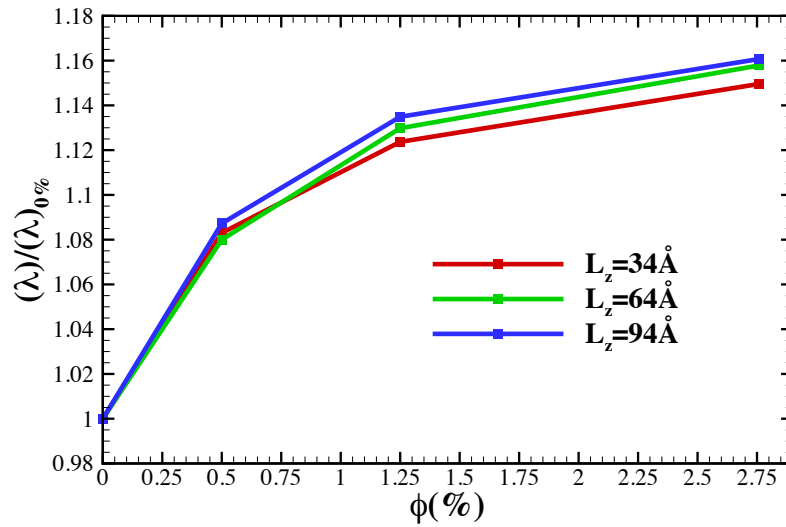
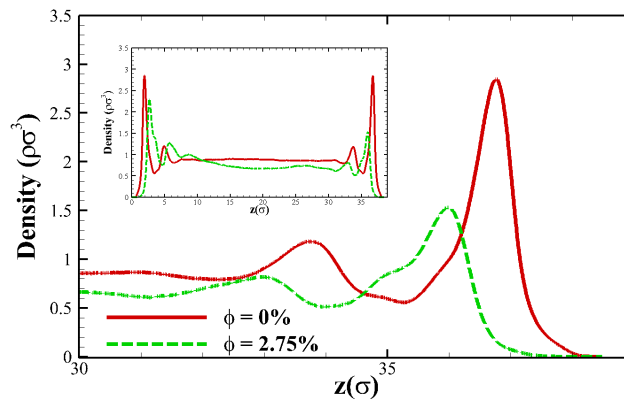
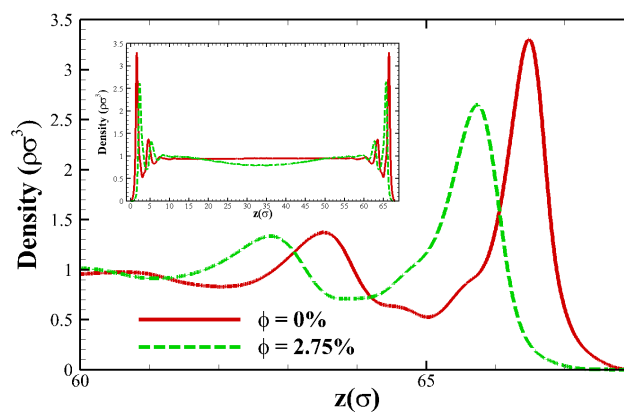


Figure 5.11: Normalized thermal conductivity of the nanofluid as a function of the volume fraction for 3 different wall separations.



(a) 30 Å wall separation distance



(b) 60 Å wall separation distance

Figure 5.12: Density profiles for pure water ($\phi = 0\%$) and a nanofluid with particle loading $\phi = 2.75\%$ for two different wall separation distances

As the channel walls are pulled further apart, the effect of the particle on the liquid structure becomes less intense (figure 5.12b). In the wider channel, the density peaks are still displaced significantly. Furthermore, the maxima of the peaks are lowered. However, the profiles preserve their oscillatory pattern.

We therefore believe that the enhancement of the thermal conductivity with the particle loading is impaired at narrower channel widths due to the damage caused to the liquid structure by the particle. This explains the results of figure 5.11. However, this is not purely the result of the interaction between the nanoparticle and liquid. It also reflects the inability of the hydrophobic graphene to hold on to its neighbouring water molecules. Under a different wall-liquid interaction, the effect of the nanoparticle on the stratified liquid can be significantly less. This is validated in the previous section in which the walls were interacting (relatively) strongly with the argon particles. The addition of the nanoparticle slightly lowered the local maxima of the thermal density profiles close to the walls. It did not displace them or change their shape as in the current case (see figure 5.5). We believe that the effect of confinement on the thermal conductivity of nanofluids depends significantly on how the various materials interact with each other.

The displacement of the liquid water towards the centre of the channel can also significantly affect the Kapitza resistance (thermal resistance at the solid-liquid interface) of the system. With the addition of the particle, the water is not wetting the graphene surface as much. This lack of contact results in a less efficient energy transfer between the liquid and solid phases [156, 171]. Depending on the specific application, this can have devastating results (e.g. if the heat is supposed to be conducted into the liquid through the walls rather than the start of the channel). Therefore for practical use, the interaction between the particle, liquid and walls must be considered carefully.

5.2.3 Summary

To summarise this section, we have studied the effect of confinement on a water-copper nanofluid confined between graphene walls. The initial observation is that the thermal conductivity, for all volume fractions of the particle, increases with decreasing channel width. However, we know from the previous chapter that confinement enhances the thermal conductivity of liquids even in the absence of a particle. In order to isolate the effect of the particle on the thermal conductivity, we calculate the thermal conductivities normalised by the value of pure water under the same confinement. Surprisingly, we find that the enhancement is in fact smaller in narrower channels. We attribute this behaviour to the particle's destructive effect on the stratified liquid close to the solid walls. This is a result of the hydrophobic graphene walls which are unable to hold the structure of the water molecules close to them, as the particle pulls them towards the centre of the channel. This distortion of the liquid structure can also have significant effects on the thermal resistance at the solid-liquid interface. Such outcome might be highly undesirable in cases where the excess heat is entering through the channel walls.

5.3 Conclusions

In this section we have studied how confinement affects the thermal conductivity of nanofluids. The main findings can be summarised as follows:

- The thermal conductivity of a confined copper-argon nanofluid increases with increasing volume fraction, beyond the predictions of classical models (equation 2.4.1)
- In very narrow channels, the thermal conductivity presents an unexpected jump. This is attributed to the structured nanolayers formed around the particle, which are greater in width and density than in the wider channels.
- The thermal conductivity of confined liquids is anisotropic. Furthermore, in the y direction, the thermal conductivity increases with increasing channel width, even when the volume fraction is decreasing. This suggests that confinement might actually have a greater influence on the thermal conductivity of liquids than the percentage of particles in the system (at least for the volume fractions considered here).
- The thermal conductivity of a copper-water nanofluid increases with decreasing channel width for all volume fractions
- By considering the normalised thermal conductivities, the enhancement of the nanofluid purely due to the adding and increasing particle loading decreases at narrower channels. This decrease is attributed to the destructive effect that the particle has on the liquid structure close to the channel walls.
- The effect of the particle on the density profiles is not consistent between different nanofluids. It is the hydrophobic nature of graphene that allows the particle to pull the water molecules towards the center of the channel. This phenomenon is absent in the cases of a copper-argon nanofluid confined between idealised walls.
- The displacement of the water away from the channel walls might have undesirable effects on the Kapitza resistance.
- Generally, the materials (for the liquid, particle and channel) cannot be considered independently. Instead, the interactions between them and their resulting effects must be carefully considered for any practical application.

Conclusions and Future Work

The technological advances of the last few decades resulted in overheating of electronic devices. The resulting high temperatures can cause the circuits to malfunction and even permanently damage the device. The thermal conductivity of traditional materials, such as aluminium and copper, cannot compensate for the generated heat. Although liquid cooling is more effective, highly demanding applications (e.g. military systems) are beyond their capacity.

The work of this thesis has made contributions towards potential improvements of thermal management techniques. A review of the literature identified nanofluids as a promising candidates as cooling liquids. However, a lack of understanding as to the physical behaviour of these systems is holding them back from commercial use. We have carried out molecular studies to gain insight, from first principles, into the effect of confinement on such systems. During this investigation, we have also found that even pure liquids transfer heat in an entirely different manner when restricted spatially. The main conclusions of the thesis can be summarised as follows:

- The thermal conductivity of copper-argon nanofluids increases along with the level of confinement. This increase is attributed to the structured liquid layering around the nanoparticles, which increase in both thickness and density in narrower channels.
- The thermal conductivity of nanofluids in nanochannels is anisotropic. The total thermal conductivity increases with decreasing channel width (as explained in the previous point). However, it decreases in the direction normal to the walls, even with decreasing volume fraction of the nanoparticle. This shows that the effect of confinement is actually greater on a liquid than the effect of the particle loading.
- The thermal conductivity of a water-copper nanofluid confined in graphene walls also increases with decreasing channel width. This is true for all volume fractions. However, normalising these thermal conductivities by that of pure water (0% volume fraction) in the same channel, it is clearly shown that the increase is entirely due to the level of confinement. In fact, these normalised thermal conductivities show

that the effect of the particle loading might be less significant in narrower channels. Following these results, our interest was diverted to the confinement of pure liquids.

- Fluids under confinement form structured layers close, and parallel to the channel walls. These solid-like layers enable the propagation of phonons with a longer mean free path, relative to those in unrestricted liquids. This can significantly enhance the thermal conductivity.
- Based on studies on solid crystals [135], we decomposed the thermal conductivity of confined liquids into its (normal) short-range, diffusive component and its long-range, ballistic components. As the channel width increases, the effect of long range phonons quickly decays to zero.
- The thermal conductivity of a liquid under confinement increases with decreasing density. This is a very interesting finding as it contradicts the behaviour of unrestricted liquids. Under no spatial restriction, an increasing density results in an increased frequency of particle collisions and a more efficient transfer of energy. In this investigation however, we have shown that under confinement, the extra availability of space allows atoms to vibrate more. Phonons travel over longer distances due to the lower frequency of collisions and the thermal conductivity is increased. Furthermore, for lower densities, the long range effects of the thermal conductivity persist in much wider channels.
- The thermal conductivity of confined liquids increases due to the availability of more energetic phonons.
- The thermal conductivity of confined liquids is higher for hydrophilic walls. As the strength of the interaction between the wall and the liquid increases, the liquid atoms close to the walls become more solid-like. This allows a more efficient propagation of phonons.

In this work we have identified phenomena which, to the best of our knowledge, have not been discovered and documented before. These can potentially play an important role in the design and optimisation of thermal management tools. However, the findings presented here are still in their infancy. A significant amount of both experimental and computational work is still required to advance from a theoretical framework to practical solutions. The major concrete steps required are:

- The most important future step is experimental verification. We appreciate the difficulty in conducting experiments in nanochannels that directly correspond to our simulations. The main two challenges are
 - Our models have used walls with no roughness. This approach provides an idealised, upper limit. However, even the most modern nanofabrication techniques cannot produce channels with entirely smooth walls.

- Experimentally measuring the thermal conductivity in nanochannels is a complicated task. We do not know of any equipment which can accurately make such observations without interfering with the system itself.
- Following the experimental challenges of the previous point, an important next step with respect to computational modelling is to introduce roughness on the channel walls. In recent years, there are a number of papers providing methodologies for modelling realistic surfaces [172, 173] (e.g. using fractals). Investigations have shown that, although nanoflows exhibit slippage when the channel walls are smooth, the introduction of roughness quickly realises the macroscopic no-slip conditions. It is therefore of practical importance to see if the phenomena discovered here would also vanish under more realistic conditions. Such areas are currently being investigated within our research group.
- The general understanding is that the thermodynamic behaviour of confined liquids and nanofluids is delicate and susceptible to changes in the system. It is of interest to see how the long range component of the thermal conductivity changes under flow conditions. We believe that for low flow rates such effects will still be evident. A particularly interesting example with practical implications, is to study the thermal behaviour of fluids moving through a wick via capillary forces.
- The results presented here are only limited to nanochannels. A big step forward is to see how some of the effects introduced in our studies scale in microchannels. As explained in the introduction, in such systems the computational complexity of MD becomes overwhelming. In recent years however, significant advances have been made in mesoscale and hybrid molecular continuum (HMCM) methods. Such multiscale approaches should be used to see whether long range phonons still persist in larger channels for low-density liquids (since the long-range components of the thermal conductivity in high-density liquids vanished in wide nanochannels).

To summarise, we believe that the research described in this thesis has introduced interesting theoretical and practical concepts that should be useful in the design and understanding of novel means of cooling electronic systems. Although further research and development will be necessary before these ideas can be exploited in practical applications, the potential benefits are significant and our research group is already taking the next steps in this direction.

Appendices

Reduced Units

Reduced units, also referred to as Lennard-Jones Units, are dimensionless units of measurement. They are frequently used instead of traditional units (e.g. International System of Units) for molecular simulations of monatomic systems whose interactions are governed by LJ potentials.

The basic concept is that the unit of any quantity can be expressed as a combination of the parameters m^* , σ^* and ε^* . Although we can set these arbitrarily, most studies set them to the mass and Lennard-Jones parameters of argon: $m^* = 6.63385 \times 10^{-26}$, $\varepsilon^* = 1.65 \times 10^{-21} J$ and $\sigma^* = 0.3405 nm$. Using these values, table A.1 converts some useful quantities to SI units.

Quantity	Reduced Unit	SI Unit
Energy	ε^*	$1.65 \times 10^{-21} J$
Length	σ^*	$0.3405 nm$
Mass	m^*	$6.63385 \times 10^{-26} kg$
Temperature	T^*	$121.0145 K$
Density	ρ^*	$1680.3 Kg/m^3$
Time	t^*	$2.1461 \times 10^{-12} s$
Thermal Conductivity	λ^*	$0.018885 W/mK$
Viscosity	η^*	$9.07818 \times 10^{-5} kg/m.s$

Table A.1: Reduced units

Bibliography

- [1] J.R. Culham, W.A. Khan, M.M. Yovanovich, and Y.S. Muzychka. The influence of material properties and spreading resistance in the thermal design of plate fin heat sinks. *Journal of electronic packaging*, 129:76, 2007.
- [2] J. Ku. Operating characteristics of loop heat pipes. *SAE transactions*, 108(1):503–519, 1999.
- [3] Kwok-hung Cheung, Triem T Hoang, Jentung Ku, and Tarik Kaya. Thermal performance and operational characteristics of loop heat pipe (nrl lhp). Technical report, SAE Technical Paper, 1998.
- [4] J Hone, MC Llaguno, NM Nemes, AT Johnson, JE Fischer, DA Walters, MJ Casavant, J Schmidt, and RE Smalley. Electrical and thermal transport properties of magnetically aligned single wall carbon nanotube films. *Applied Physics Letters*, 77(5):666–668, 2000.
- [5] P Kim, Li Shi, A Majumdar, and PL McEuen. Thermal transport measurements of individual multiwalled nanotubes. *Physical review letters*, 87(21):215502, 2001.
- [6] Savas Berber, Young-Kyun Kwon, and David Tomanek. Unusually high thermal conductivity of carbon nanotubes. *Physical review letters*, 84(20):4613, 2000.
- [7] Takeshi Nihira and Tadao Iwata. Thermal resistivity changes in electron-irradiated pyrolytic graphite. *Japanese Journal of Applied Physics*, 14(8):1099, 1975.
- [8] MG Holland, CA Klein, and WD Straub. The lorenz number of graphite at very low temperatures. *Journal of Physics and Chemistry of Solids*, 27(5):903–906, 1966.
- [9] A de Combarieu. Thermal conductivity of quasi single-crystal graphite and effects of neutron irradiation. i. measurements. Technical report, Centre d’Etudes Nucleaires, Grenoble, France, 1967.
- [10] J.W. Jiang, J.S. Wang, and B. Li. Thermal conductance of graphene and dimerite. *Physical Review B*, 79(20):205418, 2009.
- [11] D.H. Kumar, H.E. Patel, V.R.R. Kumar, T. Sundararajan, T. Pradeep, and S.K. Das. Model for heat conduction in nanofluids. *Physical Review Letters*, 93(14):144301, 2004.

- [12] J. Eapen, R. Rusconi, R. Piazza, and S. Yip. The classical nature of thermal conduction in nanofluids. *Journal of Heat Transfer*, 132:102402, 2010.
- [13] John R Hook and Henry Edgar Hall. Solid state physics (the manchester physics series), 2000.
- [14] Yujie Wu, Harald L Tepper, and Gregory A Voth. Flexible simple point-charge water model with improved liquid-state properties. *The Journal of chemical physics*, 124(2):024503, 2006.
- [15] Zachary Grant Mills, Wenbin Mao, and Alexander Alexeev. Mesoscale modeling: solving complex flows in biology and biotechnology. *Trends in biotechnology*, 31(7):426–434, 2013.
- [16] Jongin Hong, Joshua B Edel, and Andrew J Demello. Micro-and nanofluidic systems for high-throughput biological screening. *Drug discovery today*, 14(3):134–146, 2009.
- [17] Serge G Lemay. Nanopore-based biosensors: the interface between ionics and electronics. *ACS nano*, 3(4):775–779, 2009.
- [18] Mubarak Ali, Patricio Ramirez, Salvador Mafé, Reinhard Neumann, and Wolfgang Ensinger. A ph-tunable nanofluidic diode with a broad range of rectifying properties. *ACS nano*, 3(3):603–608, 2009.
- [19] Frederic Laugere, Rosanne M Guijt, Jeroen Bastemeijer, Gert van der Steen, Axel Berthold, Erik Baltussen, Pascalina Sarro, Gijs WK van Dedem, Michiel Vellekoop, and Andre Bossche. On-chip contactless four-electrode conductivity detection for capillary electrophoresis devices. *Analytical chemistry*, 75(2):306–312, 2003.
- [20] David B Tuckerman and Roger Fabian W Pease. High-performance heat sinking for vlsi. *Electron Device Letters, IEEE*, 2(5):126–129, 1981.
- [21] D. Drikakis and N. Asproulis. Multi-scale computational modelling of flow and heat transfer. *International Journal of Numerical Methods for Heat and Fluid Flow*, 20(5):517–528, 2010.
- [22] N. Asproulis and D. Drikakis. An artificial neural network-based multiscale method for hybrid atomistic-continuum simulations. *Microfluidics and Nanofluidics*, 15(4):559–574, 2013.
- [23] N. Asproulis and D. Drikakis. Surface roughness effects in micro and nanofluidic devices. *Journal of Computational and Theoretical Nanoscience*, 7(9):1825–1830, 2010.
- [24] Sydney Goldstein. *Modern developments in fluid dynamics: an account of theory and experiment relating to boundary layers, turbulent motion and wakes*, volume 1. Clarendon Press, 1938.

- [25] George Keith Batchelor. *An introduction to fluid dynamics*. Cambridge university press, 2000.
- [26] Joel Koplik, Jayanth R Banavar, and Jorge F Willemsen. Molecular dynamics of fluid flow at solid surfaces. *Physics of Fluids A: Fluid Dynamics (1989-1993)*, 1(5): 781–794, 1989.
- [27] Karl P Travis, BD Todd, and Denis J Evans. Departure from navier-stokes hydrodynamics in confined liquids. *Physical Review E*, 55(4):4288, 1997.
- [28] M Wang, J Liu, and S Chen. Electric potential distribution in nanoscale electroosmosis: from molecules to continuum. *Molecular Simulation*, 34(5):509–514, 2008.
- [29] JA Eastman, SUS Choi, S Li, W Yu, and LJ Thompson. Anomalously increased effective thermal conductivities of ethylene glycol-based nanofluids containing copper nanoparticles. *Applied Physics Letters*, 78(6):718–720, 2001.
- [30] SUS Choi, ZG Zhang, W. Yu, FE Lockwood, and EA Grulke. Anomalous thermal conductivity enhancement in nanotube suspensions. *Applied Physics Letters*, 79(14): 2252–2254, 2001.
- [31] Hrishikesh E Patel, Sarit K Das, T Sundararajan, A Sreekumaran Nair, Beena George, and T Pradeep. Thermal conductivities of naked and monolayer protected metal nanoparticle based nanofluids: manifestation of anomalous enhancement and chemical effects. *Applied Physics Letters*, 83(14):2931–2933, 2003.
- [32] JC Maxwell. *A treatise on electricity and magnetism*, 2nd edn, clarendon, 1881.
- [33] RL Hamilton and OK Crosser. Thermal conductivity of heterogeneous two-component systems. *Industrial & Engineering chemistry fundamentals*, 1(3):187–191, 1962.
- [34] Phillbot Keblinski, SR Phillpot, SUS Choi, and JA Eastman. Mechanisms of heat flow in suspensions of nano-sized particles (nanofluids). *International journal of heat and mass transfer*, 45(4):855–863, 2002.
- [35] Seok Pil Jang and Stephen US Choi. Role of brownian motion in the enhanced thermal conductivity of nanofluids. *Applied physics letters*, 84(21):4316–4318, 2004.
- [36] William Evans, Jacob Fish, and Pawel Keblinski. Role of brownian motion hydrodynamics on nanofluid thermal conductivity. *Applied Physics Letters*, 88(9): 093116–093116, 2006.
- [37] W Yu and SUS Choi. The role of interfacial layers in the enhanced thermal conductivity of nanofluids: a renovated maxwell model. *Journal of Nanoparticle Research*, 5(1-2):167–171, 2003.

- [38] Ling Li, Yuwen Zhang, Hongbin Ma, and Mo Yang. Molecular dynamics simulation of effect of liquid layering around the nanoparticle on the enhanced thermal conductivity of nanofluids. *Journal of Nanoparticle Research*, 12(3):811–821, 2010.
- [39] Jacob Eapen, Wesley C Williams, Jacopo Buongiorno, Lin-wen Hu, Sidney Yip, Roberto Rusconi, Roberto Piazza, et al. Mean-field versus microconvection effects in nanofluid thermal conduction. *Physical review letters*, 99(9):095901, 2007.
- [40] S. Krishnan, S.V. Garimella, and S.S. Kang. A novel hybrid heat sink using phase change materials for transient thermal management of electronics. *Components and Packaging Technologies, IEEE Transactions on*, 28(2):281–289, 2005.
- [41] R. Kandasamy, X.Q. Wang, and A.S. Mujumdar. Transient cooling of electronics using phase change material (pcm)-based heat sinks. *Applied Thermal Engineering*, 28(8):1047–1057, 2008.
- [42] P Teertstra, MM Yovanovich, JR Culham, and T Lemczyk. Analytical forced convection modeling of plate fin heat sinks. In *Semiconductor Thermal Measurement and Management Symposium, 1999. Fifteenth Annual IEEE*, pages 34–41. IEEE, 1999.
- [43] J Richard Culham and Yu S Muzychka. Optimization of plate fin heat sinks using entropy generation minimization. *Components and Packaging Technologies, IEEE Transactions on*, 24(2):159–165, 2001.
- [44] Robert W Keyes. Heat transfer in forced convection through fins. *Electron Devices, IEEE Transactions on*, 31(9):1218–1221, 1984.
- [45] RW Knight, JS Goodling, and DJ Hall. Optimal thermal design of forced convection heat sinks-analytical. *Journal of Electronic Packaging*, 113(3):313–321, 1991.
- [46] Roy W Knight, DJ Hall, JS Goodling, and RC Jaeger. Heat sink optimization with application to microchannels. *Components, Hybrids, and Manufacturing Technology, IEEE Transactions on*, 15(5):832–842, 1992.
- [47] Arel Weisberg, Haim H Bau, and JN Zemel. Analysis of microchannels for integrated cooling. *International Journal of Heat and Mass Transfer*, 35(10):2465–2474, 1992.
- [48] Andrei G Fedorov and Raymond Viskanta. Three-dimensional conjugate heat transfer in the microchannel heat sink for electronic packaging. *International Journal of Heat and Mass Transfer*, 43(3):399–415, 2000.
- [49] V. Singhal, S.V. Garimella, and A. Raman. Microscale pumping technologies for microchannel cooling systems. *Applied Mechanics Reviews*, 57:191, 2004.
- [50] S.V. Garimella, V. Singhal, and D. Liu. On-chip thermal management with microchannel heat sinks and integrated micropumps. *Proceedings of the IEEE*, 94(8):1534–1548, 2006.

- [51] V. Singhal. *A novel micropump for integrated microchannel cooling systems*. PhD thesis, PURDUE UNIVERSITY, 2006.
- [52] T Kishimoto and S Sasaki. Cooling characteristics of diamond-shaped interrupted cooling fin for high-power lsi devices. *Electronics Letters*, 23(9):456–457, 1987.
- [53] Benjamin A Jasperson, Yongho Jeon, Kevin T Turner, Frank E Pfefferkorn, and Weilin Qu. Comparison of micro-pin-fin and microchannel heat sinks considering thermal-hydraulic performance and manufacturability. *Components and Packaging Technologies, IEEE Transactions on*, 33(1):148–160, 2010.
- [54] Ali Kosar, Chih-Jung Kuo, and Yoav Peles. Hydrofoil-based micro pin fin heat sink. In *ASME 2006 International Mechanical Engineering Congress and Exposition*, pages 563–570. American Society of Mechanical Engineers, 2006.
- [55] G. Hetsroni, A. Mosyak, Z. Segal, and G. Ziskind. A uniform temperature heat sink for cooling of electronic devices. *International Journal of Heat and Mass Transfer*, 45(16):3275–3286, 2002.
- [56] Ali Koşar and Yoav Peles. Boiling heat transfer in a hydrofoil-based micro pin fin heat sink. *International Journal of Heat and Mass Transfer*, 50(5):1018–1034, 2007.
- [57] Charles C Roberts Jr. A review of heat pipe liquid delivery concepts. *Journal of Heat Recovery Systems*, 1(4):261–266, 1981.
- [58] Yu F Maidanik. Loop heat pipes. *Applied Thermal Engineering*, 25(5):635–657, 2005.
- [59] Yu F Gerasimov, Yu F Maidanik, GT Shchegolev, GA Filippov, LG Starikov, VM Kiseev, and Yu E Dolgirev. Low-temperature heat pipes with separate channels for vapor and liquid. *Journal of Engineering Physics and Thermophysics*, 28(6):683–685, 1975.
- [60] Jury E Dolgirev, Valery F Kholodov, Jury F Maidanik, and Sergei V Vershinin. Heat transfer apparatus, May 7 1985. US Patent 4,515,209.
- [61] Yu G Fershtater and Yu F Maidanik. Analysis of the temperature field in the capillary structure of an “antigravity” heat pipe. *Journal of Engineering Physics and Thermophysics*, 51(2):897–900, 1986.
- [62] Jane Baumann and Suraj Rawal. Viability of loop heat pipes for space solar power applications. In *AIAA Thermophysics Conference, 35th, Anaheim, CA*, pages 11–14, 2001.
- [63] Stéphane Launay, Valérie Sartre, and Jocelyn Bonjour. Parametric analysis of loop heat pipe operation: a literature review. *International Journal of Thermal Sciences*, 46(7):621–636, 2007.
- [64] Michael Pauken and José I Rodriguez. Performance characterization and model verification of a loop heat pipe. Technical report, SAE Technical Paper, 2000.

- [65] R. Chandratilleke, H. Hatakeyama, and H. Nakagome. Development of cryogenic loop heat pipes. *Cryogenics*, 38(3):263–269, 1998.
- [66] Y.F. Maydanik, S.V. Vershinin, M.A. Korukov, and J.M. Ochterbeck. Miniature loop heat pipes—a promising means for cooling electronics. *Components and Packaging Technologies, IEEE Transactions on*, 28(2):290–296, 2005.
- [67] Donya Douglas, Jentung Ku, and Tarik Kaya. Testing of the geoscience laser altimeter system (glas) prototype loop heat pipe. *AIAA Paper*, (99-0473), 1999.
- [68] M. Hamdan and E. Elnajjar. Loop heat pipe: Simple thermodynamic.
- [69] M.I. Katsnelson. Graphene: carbon in two dimensions. *Materials today*, 10(1):20–27, 2007.
- [70] Kostya S Novoselov, Andre K Geim, SV Morozov, D Jiang, Y_ Zhang, SV Dubonos, IV Grigorieva, and AA Firsov. Electric field effect in atomically thin carbon films. *science*, 306(5696):666–669, 2004.
- [71] C.J. Morath, H.J. Maris, J.J. Cuomo, D.L. Pappas, A. Grill, V.V. Patel, J.P. Doyle, and K.L. Saenger. Picosecond optical studies of amorphous diamond and diamond-like carbon: Thermal conductivity and longitudinal sound velocity. *Journal of applied physics*, 76(5):2636–2640, 1994.
- [72] Lanhua Wei, PK Kuo, RL Thomas, TR Anthony, and WF Banholzer. Thermal conductivity of isotopically modified single crystal diamond. *Physical review letters*, 70(24):3764, 1993.
- [73] J Hone, M Whitney, C Piskoti, and A Zettl. Thermal conductivity of single-walled carbon nanotubes. *Physical Review B*, 59(4):R2514, 1999.
- [74] J Hone, MC Llaguno, MJ Biercuk, AT Johnson, B Batlogg, Z Benes, and JE Fischer. Thermal properties of carbon nanotubes and nanotube-based materials. *Applied Physics A*, 74(3):339–343, 2002.
- [75] J. Hone. Carbon nanotubes: thermal properties, 2004.
- [76] W Yi, L Lu, Zhang Dian-Lin, ZW Pan, and SS Xie. Linear specific heat of carbon nanotubes. *Physical Review B*, 59(14):R9015, 1999.
- [77] M.A. Osman and D. Srivastava. Temperature dependence of the thermal conductivity of single-wall carbon nanotubes. *Nanotechnology*, 12:21, 2001.
- [78] S. Ghosh, W. Bao, D.L. Nika, S. Subrina, E.P. Pokatilov, C.N. Lau, and A.A. Balandin. Dimensional crossover of thermal transport in few-layer graphene. *Nature materials*, 9(7):555–558, 2010.
- [79] J. Che, T. Çağın, W. Deng, and W.A. Goddard III. Thermal conductivity of diamond and related materials from molecular dynamics simulations. *The Journal of Chemical Physics*, 113:6888, 2000.

- [80] Jianwei Che, Tahir Çağın, Weiqiao Deng, and William A Goddard III. Thermal conductivity of diamond and related materials from molecular dynamics simulations. *The Journal of Chemical Physics*, 113(16):6888–6900, 2000.
- [81] J.H. Seol, I. Jo, A.L. Moore, L. Lindsay, Z.H. Aitken, M.T. Pettes, X. Li, Z. Yao, R. Huang, D. Broido, et al. Two-dimensional phonon transport in supported graphene. *Science*, 328(5975):213–216, 2010.
- [82] A.A. Balandin. Thermal properties of graphene and nanostructured carbon materials. *Nature materials*, 10(8):569–581, 2011.
- [83] M. Kasimir, K. Gharagozloo-Hubmann, S. Trotsenko, GJF Czempiel, V. Datsyuk, and S. Reich. Thermal interface materials based on carbon nanotubes and their thermal characterization. In *Thermal Investigations of ICs and Systems (THERMINIC), 2010 16th International Workshop on*, pages 1–6. IEEE, 2010.
- [84] K.M.F. Shahil and A.A. Balandin. Graphene-based thermal interface materials. In *Nanotechnology (IEEE-NANO), 2011 11th IEEE Conference on*, pages 1193–1196. IEEE, 2011.
- [85] S. Subrina, D. Kotchetkov, and A.A. Balandin. Heat removal in silicon-on-insulator integrated circuits with graphene lateral heat spreaders. *Electron Device Letters, IEEE*, 30(12):1281–1283, 2009.
- [86] SUS Chol. Enhancing thermal conductivity of fluids with nanoparticles. *ASME-PUBLICATIONS-FED*, 231:99–106, 1995.
- [87] JC Maxwell. A treatise on electricity and magnetism., vol. 1 clarendon press, 1873.
- [88] SC Cheng and RI Vachon. The prediction of the thermal conductivity of two and three phase solid heterogeneous mixtures. *International Journal of Heat and Mass Transfer*, 12(3):249–264, 1969.
- [89] David J Jeffrey. Conduction through a random suspension of spheres. *Proceedings of the Royal Society of London. A. Mathematical and Physical Sciences*, 335(1602):355–367, 1973.
- [90] C.H. Li and GP Peterson. The effect of particle size on the effective thermal conductivity of al₂o₃-water nanofluids. *Journal of applied physics*, 101(4):044312–044312, 2007.
- [91] C.H. Chon, K.D. Kihm, S.P. Lee, and S.U.S. Choi. Empirical correlation finding the role of temperature and particle size for nanofluid (alo) thermal conductivity enhancement. *Applied Physics Letters*, 87:153107, 2005.
- [92] KS Hong, T.K. Hong, and H.S. Yang. Thermal conductivity of fe nanofluids depending on the cluster size of nanoparticles. *Applied Physics Letters*, 88:031901, 2006.

- [93] S.K. Das, N. Putra, P. Thiesen, and W. Roetzel. Temperature dependence of thermal conductivity enhancement for nanofluids. *Journal of Heat Transfer*, 125:567, 2003.
- [94] C.H. Li and GP Peterson. Experimental investigation of temperature and volume fraction variations on the effective thermal conductivity of nanoparticle suspensions (nanofluids). *Journal of Applied Physics*, 99:084314, 2006.
- [95] C.H. Li, W. Williams, J. Buongiorno, L.W. Hu, and GP Peterson. Transient and steady-state experimental comparison study of effective thermal conductivity of al₂O₃/water nanofluids. *Journal of Heat Transfer*, 130:042407, 2008.
- [96] N. Jha and S. Ramaprabhu. Thermal conductivity studies of metal dispersed multi-walled carbon nanotubes in water and ethylene glycol based nanofluids. *Journal of Applied Physics*, 106(8):084317–084317, 2009.
- [97] Yimin Xuan, Qiang Li, and Weifeng Hu. Aggregation structure and thermal conductivity of nanofluids. *AIChE Journal*, 49(4):1038–1043, 2003.
- [98] Xinwei Wang, Xianfan Xu, and Stephen U S. Choi. Thermal conductivity of nanoparticle-fluid mixture. *Journal of thermophysics and heat transfer*, 13(4):474–480, 1999.
- [99] J. Koo and C. Kleinstreuer. A new thermal conductivity model for nanofluids. *Journal of Nanoparticle Research*, 6(6):577–588, 2004.
- [100] R. Prasher, P. Bhattacharya, and P.E. Phelan. Brownian-motion-based convective-conductive model for the effective thermal conductivity of nanofluids. *Journal of heat transfer*, 128:588, 2006.
- [101] Hrishikesh E Patel, KB Anoop, T Sundararajan, and Sarit Kumar Das. A micro-convection model for thermal conductivity of nanofluids. In *International Heat Transfer Conference 13*. Begel House Inc., 2006.
- [102] C-J Yu, AG Richter, A Datta, MK Durbin, and P Dutta. Molecular layering in a liquid on a solid substrate: an x-ray reflectivity study. *Physica B: Condensed Matter*, 283(1):27–31, 2000.
- [103] Q.Z. Xue. Model for effective thermal conductivity of nanofluids. *Physics letters A*, 307(5-6):313–317, 2003.
- [104] Y. Feng, B. Yu, P. Xu, and M. Zou. The effective thermal conductivity of nanofluids based on the nanolayer and the aggregation of nanoparticles. *Journal of Physics D: Applied Physics*, 40:3164, 2007.
- [105] MF Reedijk, J Arsic, FFA Hollander, SA De Vries, and E Vlieg. Liquid order at the interface of kdp crystals with water: Evidence for icelike layers. *Physical review letters*, 90(6):066103, 2003.
- [106] Haiding Mo, Guennadi Evmenenko, and Pulak Dutta. Ordering of liquid squalane near a solid surface. *Chemical physics letters*, 415(1):106–109, 2005.

- [107] C.J. Yu, AG Richter, J. Kmetko, SW Dugan, A. Datta, and P. Dutta. Structure of interfacial liquids: X-ray scattering studies. *Physical Review E*, 63(2):021205, 2001.
- [108] H. Mo, G. Evmenenko, S. Kewalramani, K. Kim, S.N. Ehrlich, and P. Dutta. Observation of surface layering in a nonmetallic liquid. *Physical review letters*, 96(9): 96107, 2006.
- [109] S.A. Putnam, D.G. Cahill, P.V. Braun, Z. Ge, and R.G. Shimmin. Thermal conductivity of nanoparticle suspensions. *Journal of Applied Physics*, 99:084308, 2006.
- [110] D. Lee, J.W. Kim, and B.G. Kim. A new parameter to control heat transport in nanofluids: surface charge state of the particle in suspension. *The Journal of Physical Chemistry B*, 110(9):4323–4328, 2006.
- [111] Antonio L DeVera Jr and William Strieder. Upper and lower bounds on the thermal conductivity of a random, two-phase material. *The Journal of Physical Chemistry*, 81(18):1783–1790, 1977.
- [112] Zvi Hashin and Shmuel Shtrikman. A variational approach to the theory of the effective magnetic permeability of multiphase materials. *Journal of applied Physics*, 33(10):3125–3131, 1962.
- [113] S. Lee and S.U.S. Choi. Application of metallic nanoparticle suspensions in advanced cooling systems. Technical report, Argonne National Lab., IL (United States), 1996.
- [114] R. Chein and G. Huang. Analysis of microchannel heat sink performance using nanofluids. *Applied thermal engineering*, 25(17):3104–3114, 2005.
- [115] S.P. Jang and S.U.S. Choi. Cooling performance of a microchannel heat sink with nanofluids. *Applied Thermal Engineering*, 26(17):2457–2463, 2006.
- [116] D.J. Faulkner, D.R. Rector, J.J. Davidson, and R. Shekarriz. Enhanced heat transfer through the use of nanofluids in forced convection. ASME, 2004.
- [117] J.Y. Jung, H.S. Oh, and H.Y. Kwak. Forced convective heat transfer of nanofluids in microchannels. *International Journal of Heat and Mass Transfer*, 52(1-2):466–472, 2009.
- [118] Y. Xuan and Q. Li. Investigation on convective heat transfer and flow features of nanofluids. *Journal of Heat Transfer*, 125:151, 2003.
- [119] R. Chein and J. Chuang. Experimental microchannel heat sink performance studies using nanofluids. *International journal of thermal sciences*, 46(1):57–66, 2007.
- [120] N. Putra, W. Roetzel, and S.K. Das. Natural convection of nano-fluids. *Heat and Mass Transfer*, 39(8):775–784, 2003.

- [121] H.T. Chien, C.I. Tsai, P.H. Chen, and P.Y. Chen. Improvement on thermal performance of a disk-shaped miniature heat pipe with nanofluid. In *Electronic Packaging Technology Proceedings, 2003. ICEPT 2003. Fifth International Conference on*, pages 389–391. IEEE, 2003.
- [122] CY Tsai, HT Chien, PP Ding, B. Chan, TY Luh, and PH Chen. Effect of structural character of gold nanoparticles in nanofluid on heat pipe thermal performance. *Materials Letters*, 58(9):1461–1465, 2004.
- [123] S.W. Kang, W.C. Wei, S.H. Tsai, and S.Y. Yang. Experimental investigation of silver nano-fluid on heat pipe thermal performance. *Applied Thermal Engineering*, 26(17):2377–2382, 2006.
- [124] Mike P Allen and Dominic J Tildesley. *Computer simulation of liquids*. Oxford university press, 1989.
- [125] CS Murthy, SF O’Shea, and IR McDonald. Electrostatic interactions in molecular crystals: lattice dynamics of solid nitrogen and carbon dioxide. *Molecular Physics*, 50(3):531–541, 1983.
- [126] Bruce J Berne and Philip Pechukas. Gaussian model potentials for molecular interactions. *The Journal of Chemical Physics*, 56(8):4213–4216, 1972.
- [127] William L Jorgensen, Jayaraman Chandrasekhar, Jeffrey D Madura, Roger W Impey, and Michael L Klein. Comparison of simple potential functions for simulating liquid water. *The Journal of chemical physics*, 79(2):926–935, 1983.
- [128] William L Jorgensen. Quantum and statistical mechanical studies of liquids. 10. transferable intermolecular potential functions for water, alcohols, and ethers. application to liquid water. *Journal of the American Chemical Society*, 103(2):335–340, 1981.
- [129] Herman JC Berendsen, James PM Postma, Wilfred F van Gunsteren, and Jan Hermans. Interaction models for water in relation to protein hydration. In *Intermolecular forces*, pages 331–342. Springer, 1981.
- [130] HJC Berendsen, JR Grigera, and TP Straatsma. The missing term in effective pair potentials. *Journal of Physical Chemistry*, 91(24):6269–6271, 1987.
- [131] Liem X Dang and B Montgomery Pettitt. Simple intramolecular model potentials for water. *Journal of Physical Chemistry*, 91(12):3349–3354, 1987.
- [132] Udo W Schmitt and Gregory A Voth. The computer simulation of proton transport in water. *The Journal of chemical physics*, 111(20):9361–9381, 1999.
- [133] Daan Frenkel and Berend Smit. *Understanding molecular simulation: from algorithms to applications*, volume 1. Academic press, 2001.

- [134] Florian Müller-Plathe. A simple nonequilibrium molecular dynamics method for calculating the thermal conductivity. *The Journal of chemical physics*, 106:6082, 1997.
- [135] AJH McGaughey and M Kaviany. Thermal conductivity decomposition and analysis using molecular dynamics simulations. part i. lennard-jones argon. *International Journal of Heat and Mass Transfer*, 47(8):1783–1798, 2004.
- [136] Melville S Green. Markoff random processes and the statistical mechanics of time-dependent phenomena. *The Journal of Chemical Physics*, 20(8):1281–1295, 1952.
- [137] Ryogo Kubo. Statistical-mechanical theory of irreversible processes. i. general theory and simple applications to magnetic and conduction problems. *Journal of the Physical Society of Japan*, 12(6):570–586, 1957.
- [138] Masoud H Khadem and Aaron P Wemhoff. Comparison of green–kubo and nemd heat flux formulations for thermal conductivity prediction using the tersoff potential. *Computational Materials Science*, 69:428–434, 2013.
- [139] Alejandro Guajardo-Cuéllar, David B Go, and Mihir Sen. Evaluation of heat current formulations for equilibrium molecular dynamics calculations of thermal conductivity. *The Journal of chemical physics*, 132(10):104111, 2010.
- [140] Suranjan Sarkar and R Panneer Selvam. Molecular dynamics simulation of effective thermal conductivity and study of enhanced thermal transport mechanism in nanofluids. *Journal of applied physics*, 102(7):074302–074302, 2007.
- [141] DP Sellan, ES Landry, JE Turney, AJH McGaughey, and CH Amon. Size effects in molecular dynamics thermal conductivity predictions. *Physical Review B*, 81(21):214305, 2010.
- [142] Jie Chen, Gang Zhang, and Baowen Li. How to improve the accuracy of equilibrium molecular dynamics for computation of thermal conductivity? *Physics Letters A*, 374(23):2392–2396, 2010.
- [143] Loup Verlet. Computer" experiments" on classical fluids. i. thermodynamical properties of lennard-jones molecules. *Physical review*, 159(1):98, 1967.
- [144] Hans C Andersen. Molecular dynamics simulations at constant pressure and/or temperature. *The Journal of chemical physics*, 72(4):2384–2393, 1980.
- [145] Shuichi Nosé. A unified formulation of the constant temperature molecular dynamics methods. *The Journal of chemical physics*, 81(1):511–519, 1984.
- [146] Shūichi Nosé. A molecular dynamics method for simulations in the canonical ensemble. *Molecular physics*, 52(2):255–268, 1984.
- [147] Steve Plimpton, Paul Crozier, and Aidan Thompson. Lammmps-large-scale atomic/molecular massively parallel simulator. *Sandia National Laboratories*, 18, 2007.

- [148] Nikolaos Asproulis and Dimitris Drikakis. Boundary slip dependency on surface stiffness. *Physical Review E*, 81(6):061503, 2010.
- [149] Nikolaos Asproulis and Dimitris Drikakis. Wall-mass effects on hydrodynamic boundary slip. *Physical Review E*, 84(3):031504, 2011.
- [150] Filippos D Sofos, Theodoros E Karakasidis, and Antonios Liakopoulos. Effects of wall roughness on flow in nanochannels. *Physical Review E*, 79(2):026305, 2009.
- [151] Gabriele Tocci, Laurent Joly, and Angelos Michaelides. Friction of water on graphene and hexagonal boron nitride from ab initio methods: very different slip-page despite very similar interface structures. *Nano letters*, 2014.
- [152] Chang-Hwan Choi, K Johan A Westin, and Kenneth S Breuer. Apparent slip flows in hydrophilic and hydrophobic microchannels. *Physics of Fluids (1994-present)*, 15(10):2897–2902, 2003.
- [153] Derek C Tretheway and Carl D Meinhart. Apparent fluid slip at hydrophobic microchannel walls. *Physics of Fluids (1994-present)*, 14(3):L9–L12, 2002.
- [154] Filippos Sofos, Theodoros Karakasidis, and Antonios Liakopoulos. Transport properties of liquid argon in krypton nanochannels: Anisotropy and non-homogeneity introduced by the solid walls. *International Journal of Heat and Mass Transfer*, 52(3):735–743, 2009.
- [155] Yingchun Liu, Qi Wang, Li Zhang, and Tao Wu. Dynamics and density profile of water in nanotubes as one-dimensional fluid. *Langmuir*, 21(25):12025–12030, 2005.
- [156] Bo Hung Kim, Ali Beskok, and Tahir Cagin. Thermal interactions in nanoscale fluid flow: molecular dynamics simulations with solid–liquid interfaces. *Microfluidics and Nanofluidics*, 5(4):551–559, 2008.
- [157] Jean-Louis Barrat and François Chiaruttini. Kapitza resistance at the liquid-solid interface. *Molecular Physics*, 101(11):1605–1610, 2003.
- [158] Stefano Bernardi, BD Todd, and Debra J Searles. Thermostating highly confined fluids. *The Journal of chemical physics*, 132(24):244706, 2010.
- [159] Jie Chen, Gang Zhang, and Baowen Li. Remarkable reduction of thermal conductivity in silicon nanotubes. *Nano letters*, 10(10):3978–3983, 2010.
- [160] Lina Yang, Nuo Yang, and Baowen Li. Extreme low thermal conductivity in nanoscale 3d si phononic crystal with spherical pores. *Nano letters*, 14(4):1734–1738, 2014.
- [161] J. Li, L. Porter, and S. Yip. Atomistic modeling of finite-temperature properties of crystalline β -sic: Ii. thermal conductivity and effects of point defects. *Journal of Nuclear Materials*, 255(2):139–152, 1998.

- [162] D. Bolmatov, VV. Brazhkin, and K. Trachenko. The phonon theory of liquid thermodynamics. *Scientific reports*, 2, 2012.
- [163] GA Fernandez, J Vrabec, and H Hasse. A molecular simulation study of shear and bulk viscosity and thermal conductivity of simple real fluids. *Fluid phase equilibria*, 221(1):157–163, 2004.
- [164] Jean Frenkel. Kinetic theory of liquids. Technical report, Dover, 1955.
- [165] DL Nika, S Ghosh, EP Pokatilov, and AA Balandin. Lattice thermal conductivity of graphene flakes: Comparison with bulk graphite. *Applied Physics Letters*, 94(20):203103, 2009.
- [166] Alexander A Balandin, Suchismita Ghosh, Wenzhong Bao, Irene Calizo, Desalegne Teweldebrhan, Feng Miao, and Chun Ning Lau. Superior thermal conductivity of single-layer graphene. *Nano letters*, 8(3):902–907, 2008.
- [167] N Sankar, Nithin Mathew, and CB Sobhan. Molecular dynamics modeling of thermal conductivity enhancement in metal nanoparticle suspensions. *International Communications in Heat and Mass Transfer*, 35(7):867–872, 2008.
- [168] Pawel Keblinski, Jeffrey A Eastman, and David G Cahill. Nanofluids for thermal transport. *Materials Today*, 8(6):36–44, 2005.
- [169] S Murad, P Ravi, and JG Powles. Anisotropic thermal conductivity of a fluid in a system of microscopic slit pores. *Physical Review E*, 48(5):4110, 1993.
- [170] R Saito, R Matsuo, T Kimura, G Dresselhaus, and MS Dresselhaus. Anomalous potential barrier of double-wall carbon nanotube. *Chemical Physics Letters*, 348(3):187–193, 2001.
- [171] B. Kim. Thermal resistance at a liquid-solid interface dependent on the ratio of thermal oscillation frequencies. *Chemical Physics Letters*, 554:77–81, 2012.
- [172] CK Bora, EE Flater, MD Street, JM Redmond, MJ Starr, RW Carpick, and ME Plesha. Multiscale roughness and modeling of mems interfaces. *Tribology Letters*, 19(1):37–48, 2005.
- [173] Bing-Yang Cao, Min Chen, and Zeng-Yuan Guo. Effect of surface roughness on gas flow in microchannels by molecular dynamics simulation. *International Journal of Engineering Science*, 44(13):927–937, 2006.